

REPORT DOCUMENTATION PAGE

Form Approved
OMB No. 0704-016

AD-A280 005



This estimate is based on average 1 hour per response, including the time for reviewing instructions, searching existing data sources, and reviewing the collection of information. Send comments regarding this burden estimate or any other aspect of this burden to Washington Headquarters Services, Directorate for Information Operations and Reports, 1215 Jefferson Davis Highway, Suite 1204, Arlington, VA 22202-4302, Attention: Office of Management and Budget, Paperwork Reduction Project (0704-0168), Washington, DC 20503.

1. REPORT DATE
3/22/94

3. REPORT TYPE AND DATES COVERED
Final Dec '91- Dec '93

5. FUNDING NUMBERS
G AFOSR-91-0248

2307/BS

4. TITLE AND SUBTITLE

A Numerical Investigation of Energy Transfer and Subgrid-Scale Eddy Viscosity in Homogeneous, Isotropic and Shear Turbulence.

6. AUTHOR(S)

Richard B. Pelz

7. PERFORMING ORGANIZATION NAME(S) AND ADDRESS(ES)

Mechanical & Aerospace Engineering
Rutgers University
Piscataway, NJ 08855-0909

8. PERFORMING ORGANIZATION REPORT NUMBER

AFOSR-94 0339

9. SPONSORING/MONITORING AGENCY NAME(S) AND ADDRESS(ES)

AFOSR/NA
110 Duncan Ave. Suite B115
Bolling AFB, DC 20332-0001

10. SPONSORING/MONITORING AGENCY REPORT NUMBER

AFOSR-91-0248

11. SUPPLEMENTARY NOTES

DTIC^{NH}
ELECTE
JUN 07 1994
S D
G

94-16998

12a. DISTRIBUTION/AVAILABILITY STATEMENT

Approved for Public Release, distribution is limited.

12b. DISTRIBUTION CODE

DTIC QUALITY INSPECTED 2

13. ABSTRACT (Maximum 200 words)

Numerical solutions to the Navier-Stokes equations for a 3-D, time-dependent, highly-symmetric flow (Kida, 1985 J. Phys. Soc. Jpn 54) have been completed. An effective resolution of up to 1024³ collocation points (341 modes after dealiasing) is attained within the memory on the 256 MW CRAY-2 at Kirtland AFB and the C90 at the Pittsburgh Supercomputer Center. These simulations constitutes the highest resolution runs made to date. One of the primary purposes of the work was to create a data base from which a detailed energy transfer and triad analysis could be made by Andrzej Domaradzki at USC. The data base has been made, and runs for Reynolds numbers of 500, 1000, 2000 and 5000 have been stored on tape. We shall give some information concerning the turbulent flows later in this report. The other purpose of this work is to try to understand the transition process through which the flow becomes turbulent. Our early-time analysis of the data base of runs was concerned with this problem, and hence most of this report will deal with our findings. We also attach a manuscript on this subject that will be published shortly in *The Physics of Fluids*. The transition process is dominated by a thoroughly unexpected and singular phenomenon which most certainly has ramifications in the theory of singularities of Euler and Navier-Stokes equations, but also may have applications in turbulence and mixing away from solid boundaries.

14. SUBJECT TERMS

Turbulent Flows, Transition, Numerical Simulation

15. NUMBER OF PAGES

5 (90 manuscript)

16. PRICE CODE

17. SECURITY CLASSIFICATION OF REPORT

Unclassified

18. SECURITY CLASSIFICATION OF THIS PAGE

Unclassified

19. SECURITY CLASSIFICATION OF ABSTRACT

Unclassified

20. LIMITATION OF ABSTRACT

UL

94 6 6 0 5 2

Final Technical Report
PI: Richard B. Pelz
Grant: AFOSR-91-0248

AFOSR-TR- 94 0339

Mechanical and Aerospace Engineering
Rutgers University
Piscataway, NJ 08855-0909

Approved for public release;
distribution unlimited.

Summary

Numerical solutions to the Navier-Stokes equations for a 3-D, time-dependent, highly-symmetric flow (Kida, 1985 J. Phys. Soc. Jpn 54) have been completed. An effective resolution of up to 1024^3 collocation points (341 modes after dealiasing) is attained within the memory on the 256 MW CRAY-2 at Kirtland AFB and the C90 at the Pittsburgh Supercomputer Center. These simulations constitutes the highest resolution runs made to date.

Goal 1

One of the primary purposes of the work was to create a data base from which a detailed energy transfer and triad analysis could be made by Andrzej Domaradzki at USC. The data base has been made, and runs for Reynolds numbers of 500, 1000, 2000 and 5000 have been stored on tape. We shall give some information concerning the turbulent flows later in this report.

Goal 2

The other purpose of this work is to try to understand the transition process through which the flow becomes turbulent. Our early-time analysis of the data base of runs was concerned with this problem, and hence most of this report will deal with our findings. We also attach a manuscript on this subject that is currently in review in *The Physics of Fluids*. The transition process is dominated by a thoroughly unexpected and singular phenomenon which most certainly has ramifications in the theory of singularities of Euler and Navier-Stokes equations, but also may have applications in turbulence and mixing away from solid boundaries.

Background Information

In order to simulate directly turbulent flows with high Reynolds numbers, we make use of symmetries of the Navier-Stokes equations. These symmetries are 2π periodicity, mirror symmetries at planes $x_i = n\pi$, where $i = 1, 2, 3$ and $n = 0, \pm 1, \pm 2, \dots$, rotation (by $\pi/2$) symmetry

Dist	Avail and / or Special
A-1	

around axes, $(x_i, x_j) = (\pi/2, \pi/2)$ for $(i, j) = (1, 2), (2, 3), (3, 1)$, and a velocity permutation symmetry such that $u_1(x_1, x_2, x_3) = u_2(x_2, x_3, x_1) = u_3(x_3, x_1, x_2)$.

These symmetries may not be stable, and may be observed in nature for a short time only. We have found, however, that the turbulent flows that result from these symmetries is qualitatively similar to flows which do not enforce the symmetries. Enforcing the symmetries, allows us to reduce the memory requirements by almost 200 times and the number of operations per timestep by almost 100. Simulating these prototypical flows are the only practical way to study flows with a long range of scales (or high Reynolds numbers). Otherwise, we must wait for over a hundred-fold increase in computing power in order to simulate flows with such a range without the symmetries.

Early Time Behavior and Transition

The transition to turbulence in this flow is important for a number of reasons. As in the Taylor-Green vortex, there is no wall or forcing that allows a known transition process to occur. Mechanisms for transition in these flows have been conjectured to be by vortex reconnection or by vortex-sheet rollup, but have not been proved. There are practical applications in which a turbulent field is desired in an isolated region away from walls, say to enhance mixing, where a laminar one exists. We have therefore tried to understand the transition process in this flow.

The first result is that the transition is a nearly singular event in space and time, requiring a very high resolution. In the above mentioned reference (Kida), simulations with Reynolds numbers $1/\nu$ of up to 5000 were presented. In our work, it is shown that with much higher resolution, the transition is not well resolved and that numerical errors are involved in the transition event and subsequent evolution. It is interesting to note that the transition event requires much more resolution than the turbulence that follows. In order to resolve properly and understand this transition process, we ran a succession of Reynolds numbers from 5000 down to 500. A short discussion of the results are to follow; see the manuscript for more details.

From simple low-mode initial conditions and no forcing, the flow develops a structure we call a "vortex dodecapole" around the origin. Twelve vortex tubes, grouped as six dipoles each straddling an axis collapse symmetrically towards the origin. This structure is caused by the mirror symmetries and velocity permutations imposed on the flow, but may exist, for some time, without symmetries. A 6-vortex structure appears around the point $(\pi/2, \pi/2, \pi/2)$. For some time period in

the evolution, the dodecapole exhibits what we believe is a self-similar behavior, collapsing toward the origin at the same rate that the tube radius is decreasing due to stretching.

The collapse is eventually altered and then halted. Even in the low Reynolds number case, the highest resolution (1024^3) was required for adequate resolution (at least 10 decades in range of energy spectra). The energy spectrum is full but seems to lack any particular power law scaling. In the higher Reynolds number cases, the flow undergoes transition in which small-scale vorticity is produced from around the collapse points and eventually fills the domain in an apparently random fashion. While we believe that in the high Reynolds number cases, lack of resolution which brings about errors and aliased modes, causes the dodecapole to break down, in careful observation of the lower Re cases, we see what we believe to be the start of vortex reconnection between the tubes of the dodecapole. When partial reconnection begins, the self similarity is then lost and the structure becomes unstable and breaks up into small scale vorticity.

While some integral quantities such as energy and enstrophy only very weakly reflect this event, skewness and flatness show large fluctuations. Local quantities like the maximum of vorticity show even wilder behavior. The peak in enstrophy occurs just before the transition. Skewness peaks sharply at the time of the transition with values of 0.55 for $Re=500$, 0.70 for $Re=1000$, 0.95 for $Re=2000$, and 1.1 for $Re=5000$. Skewness then drops to between .4 and .5 in the turbulence flow regime. Flatness peaks at 19, 37, 82 and 170, but shows signs of nonconvergence. The case $Re=1000$ shows a difference in peak flatness with resolution: 27 for 256^2 , 34 for 512^3 , and 37 for 1024^3 . If the peak values of quantities differ, the subsequent evolution differs also but to a lesser extent. The maximum of vorticity peaks spatially in the middle of a vortex tube of the dodecapole and temporally at transition. Even in the $Re=500$ case, the peak values are 100 for 256^3 , 115 for 512^3 and 120 for 1024^3 . After the breakup of the coherent vortices, there is a sharp drop in all quantities.

In the higher Reynolds number cases, it is not clear whether viscosity or lack of numerical resolution is causing the transition since similar but less dramatic behavior is seen at lower Re . We speculate that the dodecapole may be a finite-time singularity of the Euler equations. The structure of the singularity is characterized by an analyticity strip analysis and by curve fitting of the maximum value of vorticity. The latter analysis shows that the maximum vorticity scales as $(T - T_{cr})^{-1}$ shortly before the transition. The width of the analyticity strip (distance of the nearest singularity in complex space-time to real space-time) approaches zero faster than exponential. Exponential behavior suggests no finite time singularity.

It is interesting to speculate about experimentally creating similar structures. When two vortex rings are shot symmetrically towards each other, rapid stretching occurs and after the symmetry is broken, there is a rapid evolution of small scale vorticity and turbulence. The dodecapole is perhaps an extreme example of such a phenomenon.

This work has spawned other research including my current project on direct simulations of turbulence in complex time in which we attempt to establish the location and form complex time singularities in order to find the leading behavior of turbulence in real space-time.

The Turbulence Stage

After the peak in dissipation rate has been reached, the energy spectra begin to show Kolmogorov scaling. We refer to figure 4c in the manuscript and note that the $k^{-5/3}$ scaling exists from a wavenumber of 10 to 150 (1.2 decades). We also refer to figure 11, an isovorticity surface plot which shows an apparently random distribution of vorticity which gives rise to such a scaling.

2. Knowledge Transferred through talks at NCAR, APS, Observatoire Cote Azure, AGARD Meeting in 5/94.

3. Publications

Pelz, R.B. and Boratav, O.N., "Direct Numerical Simulation of Transition to Turbulence from a High-Symmetry Initial Condition", *The Physics of Fluids*, in review.

4. No Patents, Honors or Awards

5. Postdoc supported on this grant: Olus Boratav currently

Henri Poincare Fellow
Observatoire de Cote Azure
Nice France
and
Assistant Professor of Mechanical Engineering
Middle East Technical University, Ankara

abstract

The three-dimensional time evolution of a high-symmetry initial condition¹ is simulated using a Fourier pseudospectral method for $Re = 1/\nu = 500, 1000, 2000, 5000$ with an effective resolution of 1024^3 collocation points (171^3 independent modes, maximum wavenumber $k_{max} = 340$). It is found that much before the peak enstrophy is reached, there is a short interval when the local quantities increase sharply. It is also found that during this interval, 6 vortex dipoles (at the origin) and 3 dipoles (at the $\pi/2$ corner) collapse towards two separate vorticity null points at the opposite corners of the domain in a nearly self-similar fashion. The coherent vortices break up afterwards followed by sharp decrease in local quantities. The singularity analysis shows that, within the limits of the resolution, the maximum vorticity scales approximately as $(T - T_c)^{-1}$ shortly before the break up. However, the increase in peak vorticity stops at a certain time possibly due to viscous dissipation effects. The temporal evolution of the width of the analyticity strip shows that δ approaches zero at a rate faster than exponential, but reaches a minimum value and starts to increase. This suggests that the solution remains uniformly analytic as is the case in the viscous Burgers equation.

1 Introduction

It is well-known that ² the degrees of freedom required to simulate a three-dimensional turbulent flow scale with $Re^{9/4}$, and hence it is extremely difficult to simulate turbulent flows of high Reynolds number. The difficulty can be partially compensated by using initial conditions having symmetries. For such flows, it is possible to calculate the evolution in a fraction of the whole flow field and thus to increase the *effective resolution*. Navier-Stokes equations, in the absence of solid boundaries, will preserve the symmetries of the initial conditions with time since they are invariant under several transformation groups, namely, space translations, rotations and plane reflections.

A popular example of an initial condition with high-symmetries is the Taylor-Green vortex ³. By making use of symmetries, it is possible to gain a factor of 4 in the separation of scales, 64 in memory, 32 in number of operations ⁴. An initial condition with an even larger number of symmetries is the high-symmetry flow suggested by Kida ¹. The symmetries of this flow reduce the memory requirement by a factor of 192 and the number of operations by a factor of 96 (3 times more than the Taylor-Green vortex).

Both flows have been analyzed extensively by direct numerical simulations. The former by Orszag ⁵, Brachet et al. ^{4,6,7}, and the latter by Kida and Murakami ^{8,9}. Table 1 presents an outline of the parameters of study in these works. In Table 1, the last three columns give the resolution of the whole flow field (periodicity box), the first one the number of collocation points before dealiasing and the second one the number of independent Fourier modes after dealiasing and the last one the maximum resolved

wavenumber k_{max} in the flow field. To the authors' knowledge, the present work has the highest resolution obtained in literature using Fourier spectral methods. Also given in Table 1 is the Reynolds number based on the Taylor microscale, R_λ , which evaluated at the time when the peak dissipation is attained (See Section 2 for the definition of R_λ).

The previous simulations in literature^{6,9} show that several features of fully developed turbulence are observed at late times (after the peak in dissipation is reached). Taylor-Green simulations show that the energy spectra follow a power law in wave-number, the exponent being between 1.47 to 2.02. The Kolmogorov constant, on the other hand, is approximately equal to 4, a value considerably larger than the experimentally observed values of 1.4-1.5. Simulations by Kida and Murakami give the Kolmogorov's constant to be between 1.2 to 2.0, a closer value to the experiments. Their energy spectra power law exponent is calculated to be between 1.5 to 1.7.

Perhaps the more interesting stage in the flow is the early time evolution; an interval before the peak in enstrophy and dissipation is attained. Viscous Taylor-Green flow simulations show that it is during this interval the coherent, highly-symmetric vortices start to break up. The transition mechanism is not well-understood, but there are several scenarios proposed⁶ such as Kelvin-Helmholtz type inviscid instability mechanisms or viscosity induced instabilities and possible vortex reconnections. For the inviscid flow simulations, on the other hand, the question as to whether the smooth initial conditions will remain regular or not when the three-dimensional Euler equations are solved is yet to be answered. Predictions using time series analysis and Padé approximants¹⁰ gave hints that a singularity might develop spontaneously in the Taylor-Green flow and the

structure of the flow near the singular time T_c will have important consequences for the generation of small scale turbulent structures and intermittency. However, more recent work by Brachet et al.⁶ using a more extended series could not confirm the existence of a finite time singularity. An alternate approach¹¹ is to examine the time evolution of the width of the analyticity strip δ (the distance to the real domain of the nearest singularity). If δ goes to zero in finite time, the solution becomes singular. Simulations by Brachet et al.⁶ showed that δ decreases exponentially within the limits of resolution which suggests that the singularity will never occur in finite time. However, the resolution problems arise at an early time leaving the results inconclusive.

The present work focuses on the high-symmetry flow by Kida and Murakami^{8,9} particularly at the early stage of the flow when the coherent vortices start to break up. Since the evolution of the flow field in physical space has not been presented by Kida and Murakami^{8,9}, we emphasize the physical pictures (vorticity contour sections and isosurfaces) in detail. Section 2 presents the initial conditions, governing equations and the parameters of study. Section 3 gives the description of the flow field with time emphasizing the role of symmetries on the flow dynamics. Section 4 focuses on the evolution of local and total quantities, with a discussion on the possible singularity formation and the role of resolution on our results. Section 5 presents the conclusions.

2 Equations Solved, Initial Conditions, Parameters of Study

The equations solved are the three-dimensional Navier-Stokes equations in rotational form given by

$$\frac{\partial \mathbf{u}}{\partial t} - \mathbf{u} \times \boldsymbol{\omega} = -\nabla \Pi + \nu \nabla^2 \mathbf{u} \quad (1)$$

with the incompressibility condition given by

$$\nabla \cdot \mathbf{u} = 0 \quad , \quad (2)$$

where \mathbf{u} and $\boldsymbol{\omega}$ are the velocity and vorticity vectors respectively and $\Pi = \frac{\rho}{\rho} + (1/2)\mathbf{u}^2$ and the density, $\rho = 1$.

The initial conditions are given by

$$u(x, y, z, t = 0) = \sin x (\cos 3y \cos z - \cos y \cos 3z) \quad (3)$$

$$v(x, y, z, t = 0) = \sin y (\cos 3z \cos x - \cos z \cos 3x) \quad (4)$$

$$w(x, y, z, t = 0) = \sin z (\cos 3x \cos y - \cos x \cos 3y) \quad (5)$$

where u , v , w denote the velocity vector components in x , y , z directions. This flow has been suggested by Kida and Murakami and a detailed summary of the flow symmetries are discussed by these authors ^{1,8}. In this work, we will refer to the initial condition as the '*high-symmetry initial condition*'.

The symmetries, which we shall only list here, occur in all three directions, and are a 2π periodicity, a bilateral symmetry through planes $n\pi$, $n = 0, \pm 1, \pm 2, \dots$, a $\pi/2$

rotational symmetry around the axis $(\pi/2, \pi/2)$, and a permutation symmetry of the velocity components, $u(x, y, z) = v(y, z, x) = w(z, x, y)$.

If the above flow is compared to the Taylor-Green initial conditions in Fourier space, certain differences are found. The number of non-zero Fourier coefficients of the velocities for the Taylor-Green flow is 2, compared to 6 for the high-symmetry initial condition. The magnitude of the initial wave-number vector \mathbf{k} corresponding to non-zero Fourier modes of the velocities is $\sqrt{1+1+1} = \sqrt{3}$ for the Taylor-Green flow compared to $\sqrt{11}$ for the high-symmetry initial condition.

Figures 1 (top left) and 2 (top left) give an isosurface of the magnitude of the vorticity $\hat{\omega} = 0.3\omega_0$ of the initial condition from two views.

We solved the governing equations using a Fourier pseudo-spectral method with the “2/3 rule” dealiasing ¹². We used the second-order accurate method of time-split fractional steps for time integration. The details of the numerical method can be found in our previous work ¹³, Appendix B.

The even-mode, odd-mode cosine and sine transforms are evaluated using an FFT for real sequences and suitable pre- and post-processing as given by Cooley et al. ^{14,15} and Brachet et al. ⁶. Only four arrays and four three-dimensional transforms are required per time step. An in-place indicial permutation to obtain the three velocity components, when needed, is used.

The parameters of the study are presented in Table 2. It is worth emphasizing what is meant by resolution in this table. As an example, for Run B2, the total resolution is given by 1024^3 which is the total number of collocation points in the periodicity box.

This is also equivalent to 256 independent Fourier modes. We use dealiasing in our code which reduces the independent Fourier modes to $2/3 \times 256 = 171$ (and a maximum wavenumber $k_{max} = 341$). Note that the symmetries allow us to solve the problem in the fundamental box which has a resolution of $(1024/4)^3 = 256^3$.

As seen from Table 2, we have four runs with Reynolds numbers, ($Re = 1/\nu$) 500 for Run C, 1000 for Run D, 2000 for Run A and 5000 for Run B. For Run A, remeshing is done at $t=0.785$ by appending zero Fourier modes, thus increasing the total resolution from 256^3 to 512^3 , and Run A2 is started at this time. Further remeshing is done on Run A2 at $t=1.625$ increasing the resolution from 512^3 to 1024^3 and Run A3 is started at this instant. We also continued both Runs A1 and A2 until $t=2.25$ with the lower resolution.

For Runs C and D, remeshing is done at $t=0.8$ increasing the total resolution from 256^3 to 512^3 , and Run C2 (and D2) is started at this time. Further remeshing is done on Run C2 (and D2) at $t=1.55$ increasing the resolution from 512^3 to 1024^3 and Run C2 (and D2) is started at this time.

For Run B, we started with a higher resolution, 512^3 and increased the resolution to 1024^3 at $t=1.625$ and started the Run B2.

Later, it will be clear to the reader after reading Section III and IV why we stop the runs at the particular times. We postpone this discussion to these sections.

For each resolution, the time step is determined from the CFL condition and checked continuously throughout each run. It was possible to use an even larger Δt for Runs A1, C1, D1 but we kept it the same as in Runs A2, C2, D2 since the computational cost of

Runs A1, C1, D1 was very low.

The computational time and memory requirements of the runs are presented in Table III. We used the (single processor) Cray 2 at the Kirtland Supercomputer Center and the Cray Y-MP at the Pittsburgh Supercomputing Center for one low resolution run. Cray Y-MP is more than twice faster than the Cray 2 but does not have sufficient memory for the high resolution runs. Also, the turnaround time at the Kirtland Center was much faster than in Pittsburgh. For some of the post-processing calculations, and short runs, we used the newly installed Cray 90 (C-90) at the Pittsburgh Supercomputing Center ¹⁶.

We calculated certain total and local quantities in each run during the evolution. These were stored at every $t=0.0125$. We stored the velocity, vorticity and dissipation vector fields at every $t=0.125$ and sometimes every $t=0.0625$.

We calculated the total energy E ; and total enstrophy Ω ; given by

$$E = \frac{1}{V} \int \frac{1}{2} (u^2 + v^2 + w^2) dV \quad (6)$$

$$\Omega = \frac{1}{V} \int \frac{1}{2} (\omega_x^2 + \omega_y^2 + \omega_z^2) dV \quad (7)$$

where ω_x , ω_y , ω_z are the vorticity vector components in x, y, z directions respectively. For the discrete problem, the integrals are summations over all grid points in the solution domain and V is the total number of grid points.

Also calculated are the total dissipation ϵ , the velocity derivative skewness S and flatness F given by

$$\epsilon(t) = \frac{1}{2} \nu S_{ij} S_{ij} \quad (8)$$

$$S = - \frac{< (\partial u / \partial x)^3 >}{< (\partial u / \partial x)^2 >^{3/2}} \quad (9)$$

$$F = \frac{\langle (\partial u / \partial x)^4 \rangle}{\langle (\partial u / \partial x)^2 \rangle^2} \quad (10)$$

where $\langle \rangle$ denotes averaging over all grid points at a given time, and S_{ij} is the strain rate tensor. We emphasize that our skewness and flatness calculations are performed directly using the above relations without making any additional assumption as isotropy.

We also calculated the Reynolds number based on Taylor microscale R_λ , Kolmogorov microscale η and Kolmogorov wavenumber k_η defined as

$$R_\lambda = \sqrt{(10/3)} \frac{E(t)}{\nu \sqrt{\Omega}} \quad (11)$$

$$\eta = (\nu^3 / \epsilon(t))^{1/4} \quad (12)$$

$$k_\eta = 1/\eta \quad (13)$$

Several other local quantities are calculated. These are the local maximum velocity, vorticity, dissipation u_{max} , ω_{max} , ϵ_{max} .

And finally, we calculated the band-averaged three dimensional energy spectrum $E(k, t)$ given by

$$E(k, t) = \frac{1}{2} \sum_{k \in A} |\hat{u}(k, t)|^2 \quad (14)$$

where A is the domain for $p - \Delta \leq k \leq p + \Delta$, $p = 0, 1, \dots$. Values for Δ are $1/2$ and 1 .

We denote the magnitude of the wavenumber vector by k , that is; $k = |\mathbf{k}|$.

3 Flow Evolution

We start this section giving the statistics of Run B1. This run has the same initial conditions as one of the runs Kida and Murakami ⁹ simulated so we will compare our

results with that run in detail.

3.1 Late Stages

The evolution of energy E , enstrophy Ω , dissipation ϵ and the Taylor Reynolds number R_λ are given in Figure 3. We compare these results with Figures 1, 2, 3 and 4 of the work by Kida and Murakami ⁹. We find that there is perfect agreement between the two simulations.

As seen from Figure 3, the energy stays constant until $t=2$ showing that the flow is close to inviscid at this stage. The enstrophy and dissipation increase smoothly (without any sudden jump), the log-linear plot shows an almost straight line with time implying that the initial enstrophy increase is at least exponential. In fact, there are indications that the almost straight line in Figure 3 for enstrophy is slightly parabolic which would give a faster than exponential growth rate. A final observation in Figure 3 is that there is a small dimple observed in E , Ω and R_λ between $t=2$ and 3. This clearly shows a change in the rate of increase (decrease) but at this stage it is not clear why it is so.

The flow field after the peak ϵ is attained at $t=3.5$ starts showing statistics in agreement with Kolmogorov's scalings. Figure 4a and 4b shows the spectra and the spectra multiplied by $k^{5/3}$ at $t=6$. We observe Kolmogorov scaling between $k=10$ to 70. There is a very slight bump at $k=170$ which is noticeable but not severe enough to suggest the resolution problems. Figure 4c shows the spectra multiplied by $k^{5/3}$ for Run B2 (our highest resolution run) for different late times (6 different times between $t=5.75$ and 6.00) which exhibits Kolmogorov scaling between the wavenumbers $k=10$ to 150.

Questions arise as to how the coherent initial vortices evolve into isotropic structures giving Kolmogorov scaling, what the transition mechanisms are, when the transition takes place and whether there is enough resolution in this high Reynolds number run or not. One resolution adequacy check is to calculate the time evolution of the Kolmogorov wavenumber k_η and compare it to the highest resolved mode in Run B1 (which is 170). Figure 5 gives this evolution. We see that k_η increases to 323, which is above the highest resolved mode in our run. We conclude that resolution has to be increased somewhere between $t=1$ and 2 and both our Run B1 and Kida-Murakami runs are probably underresolved. This is the main reason of our doubling the resolution at $t=1.625$ and starting Run B2 which has a maximum wavenumber of 341.

To investigate the transition mechanisms to turbulence, we return to the flow pictures in physical space in the next section.

3.2 Early Stages

3.2.1 Symmetries and Dynamics

In order to understand the early time evolution of the flow, we focus on two separate regions in the fundamental box where symmetries result in the formation of interesting vortex structures. These regions are; i) $x, y, z = \pi/2$ faces. ii) $x, y, z = 0$ faces. We will focus on the XY planes at $z=\pi/2$ and $z=0$ to describe these symmetries. Similar conclusions can be drawn for the other two planes.

For the XY plane $z=\pi/2$ the following symmetries exist:

$$u(x, y, \pi/2) = v(y, x, \pi/2) \quad (15)$$

$$w(x, y, \pi/2) = -w(y, x, \pi/2) \quad (16)$$

A similar symmetry is also present in the vorticity field. This is not written explicitly by Kida and Murakami but can be easily seen by taking the curl of the initial velocity field. Then, it can be shown that:

$$\omega_x(x, y, \pi/2) = \omega_y(y, x, \pi/2) \quad (17)$$

$$\omega_z(x, y, \pi/2) = -\omega_z(y, x, \pi/2) \quad (18)$$

It is seen from the above equation that the normal vorticity (ω_z in plane XY) is an odd function with respect to $x=y$. This is nothing but a necessary condition to obtain a dipole along the line $x=y$. The dipole is not necessarily aligned with the z axis, in addition to its out-of-plane vorticity ω_z it also has non-zero vorticity components in x and y directions.

Before giving the picture of the dipole, we emphasize its one final feature: At $t=0$, $\omega_z(x, y, \pi/2) = -\omega_z(y, x, \pi/2) = 0$, thus there is no out-of-plane vorticity in the initial field. However, there is no restriction that the vorticity will stay zero at later times at $z = \pi/2$ plane. In fact we see in Figure 6 that this is the case.

Similar symmetries exist for the other planes. There is another dipole in the $y = \pi/2$ plane along $x=z$, and still another in the plane $x = \pi/2$ along $y=z$. These three dipoles are oriented in such a way that they all move towards the point $x, y, z = \pi/2, \pi/2, \pi/2$.

The other regions of interest are the $x, y, z = 0$ planes. We will consider $z=0$ plane

to describe the symmetries. For this plane, we have

$$\omega_z(x, y, 0) = -\omega_z(-x, y, 0) \quad (19)$$

$$\omega_x = 0 \quad (20)$$

$$\omega_y = 0 \quad (21)$$

We see that the out-of-plane vorticity ω_z is an odd function with respect to the y axis and thus its image with respect to the y axis will form a dipole. Similarly, we have another symmetry with respect to the x axis. This is given by

$$\omega_z(x, y, 0) = -\omega_z(x, -y, 0) \quad (22)$$

Then, due to the above odd symmetry with respect to the x axis, the image of the vortex with respect to the x axis will form another dipole.

The symmetries have an additional property at the zero faces: The normal vorticity is zero along the *zero* edges, and is zero at the origin. Then, the origin is a vorticity *null point*.

With all these symmetries in mind, we describe the evolution of the high-symmetry flow in the next section.

3.2.2 Evolution

Figures 1, 2, 7-12 display magnitude of vorticity isosurfaces at different times for Run B from two different angles. The first view angle is used in Figures 1, 7, 9, 11, 12 and shows the $x, y, z = \pi/2$ planes clearly. The second view angle is used in Figures 2, 8, 10 and shows the origin.

The initial stages of the evolution is seen in Figures 1, 2. Figure 1 shows that three dipoles are immediately formed with oppositely-signed vortices approaching towards one another due to the strain field set up in the flow field. At $t=0.75$ (Figure 1, bottom right), the standard head-tail cross sections of the three dipoles in the $x, y, z = \pi/2$ planes are clearly seen. In the meantime, a different motion takes place near the origin. To see the dynamics, we consider the smaller vortex given in Figure 2 (bottom). This vortex will have an image vortex located below with opposite sign (quadrant 4), another image vortex located to its left of opposite sign (quadrant 2) and finally the image vortex in quadrant 2 will have an image in quadrant 3. Therefore, totally, we have 4 vortices or 2 dipoles in the $z=0$ plane. A similar argument can be made for $x=0$ and $y=0$ planes giving 8 more vortices or 4 more dipoles. So, there are 12 vortices or 6 dipoles on the zero faces approaching the origin. We shall call this configuration a *dodecapole* since we can treat it as an entity (six dipoles) straddling each of the axes. We emphasize that in all vorticity isosurfaces given in this work, only the fundamental box is displayed. Therefore, only three vortices (1/4 th of the 12) will be seen in the pictures.

The three vortices of the dodecapole approach to the edges and start to get flattened. The flattening can be better seen in Figure 13 which shows the magnitude of vorticity contours at $t=0.75, 1.0, 1.25$ and 1.5 for Run A. The topology looks similar to the *typical* flattening and subsequent head-tail formation of a dipole. (For example: See Figures 6 and 7 by Kerr ¹⁷). We remind the reader that our configuration has three flattened vortices in each plane (or 12 when the images are considered) converging to a null point (the origin).

Figures 7 and 8 show the vorticity isosurfaces at $t=1.25, 1.5, 1.75, 1.81$. The vorticity has amplified considerably at this stage and the threshold is raised for clarity. Three dipoles directed towards the point $\pi/2, \pi/2, \pi/2$ is clearly seen at $t=1.25$ (Figure 7, top left). At $t=1.5$, more vortex tubes appear on each $\pi/2$ face (Figure 7, top right). When part of each main dipole exits on a face, it enters on two other faces due to the symmetries which are given by

$$\omega_x(\pi/2, y, z) = -\omega_y(x, \pi/2, z) = -\omega_z(z, y, \pi/2) \quad (23)$$

At $t=1.75$ and 1.81 (Figure 7, bottom), the dipole structure is becoming distorted and the flow is becoming increasingly complicated. To see the complexity, we display in Figure 14, a contour section at $z = \pi/2$ for the times $t=1.25, 1.5, 1.625, 1.75$. (Recall the symmetry presented before with respect to $x=y$ line.) In the meantime, the vortices of the dodecapole continue to get flattened as seen from Figure 8. The threshold chosen does not show the connectivity between the dodecapole and the dipoles but the main reason of the choice is to focus on the structure near the origin.

Figures 9 and 10 display the evolution at $t=1.875, 1.937, 2.0$ and 2.0625 . The vorticity threshold is raised even more compared to the previous figures. It seems that the vorticity is becoming smaller in scale. Both the dipoles approaching the $\pi/2, \pi/2, \pi/2$ corner and the three vortices of the dodecapole approaching the origin start breaking up. A vorticity cross section given in Figure 15 shows that the structure still preserves its shapes until $t=2.062$ but afterwards (Figure 16), tremendous amount of small-scale vorticity is observed.

From all these pictures, it is clear that a major break up takes place for Run B

roughly between $t=1.875$ and $t=2.5$. We have not displayed the isosurfaces for runs A, C and D but these runs also have qualitatively similar pictures in the same interval. There are slight quantitative differences which are discussed in Section 4.1.

Now if we return to Figure 3, we observe that none of the quantities displayed show any major change during this interval. Perhaps enstrophy and dissipation rate changes slightly but this is hardly noticeable. It is well-known that most of the integrated quantities in vortex interactions are not sensitive enough to reflect sudden changes in the flow field due to the violent intermittent events. However, there are some exceptions such as velocity derivative skewness and flatness which reflect the sudden changes in the vortex interaction dynamics properly. For example, in vortex reconnection problems, when the interaction is at its most intense stage, sharp increases in skewness values are observed ¹⁸. A similar trend is seen in the work by Brachet et al. ⁶ (their Figure 10) and Domaradzki et al. ¹⁹ (their Figure 1c).

In order to quantify the transition dynamics, we look at the evolution of certain quantities which could capture the important events. That, we present in the next section.

4 Transition Stage: Quantification

4.1 Evolution of Local and Total Quantities

We present in Figures 17-18 the evolution of total and local quantities as energy E , enstrophy Ω , Kolmogorov wavenumber k_η , Taylor Reynolds number R_λ , velocity derivative

skewness S and flatness F and maximum vorticity ω_{max} . Due to the space limitation, we will only present the results of the highest Reynolds number run (Run B). The results obtained in Runs A, C and D, will be mentioned whenever necessary. Figures 17 and 18 give results from Run B with a comparison of the results of two different mesh sizes, Run B1 (dashed) and Run B2 (solid). Figure 19 gives a comparison of two of the runs having higher resolution, Run A3 (solid) and Run B2 (dashed).

We see in Figures 17 and 19 that evolution of energy, enstrophy, Kolmogorov wavenumber (which is also a function of enstrophy) and Taylor Reynolds number (which is a function of enstrophy and energy) are not significantly different for different resolutions. Quantitatively, if Run B2 and B3 are compared, the energy differs by less than 1%, enstrophy less than 5%.

Next, we discuss the evolution of certain local quantities. We see from Figure 18 that approximately between $t=1.5$ and 2.5, there are drastic changes in the local maximum vorticity. In this short interval, local maximum vorticity ω_{max} increases 13 times for Run A3, 16 times for Run B2 (Figure 18, bottom), 6.5 times for Run C3 and 10 times for Run D3. Skewness increases as much as 1.1 for Run B2 (Figures 18 and 20), 0.9 for Run A3, 0.55 for Run C3 and 0.70 for Run D3. Flatness increases to 170 for Run B2 (Figures 18 and 20), 80 for Run A3, 19 for Run C3 and 37 for Run D3. The smallest change is found in the local maximum velocity u_{max} which increases less than twice in Run B2 (not shown).

All these sudden increases are followed by sudden drops which are as sharp as the increase rates. Certain quantities start to show fluctuations after this stage (such as

ω_{\max} and S in Figure 18).

Now it becomes clear that the display of these local quantities illuminates a violent, intermittent event taking place in the flow field. In the absence of this diagnostics (as is the case in Kida and Murakami ⁹), it is not possible to see the intensity of this event by only looking at energy and enstrophy pictures only. The event is so sudden and intense that all the local functions appear to look like the *delta function* at this instant.

Questions arise as to how effectively this large local quantity can be resolved and how much the results vary with resolution. It is evident that for the extreme hypothetical case when one of the local quantities is a delta function, it can be only resolved with infinite resolution. An ideal shock wave (with zero thickness), for example, in the absence of any smoothening, needs infinite number of grid points to be resolved.

In appendix A, we show the dependence of the Fourier transform of a delta function on the numerical resolution (the cut-off). It is seen from this derivation that for such a function, doubling the resolution will double the amplitude of the function.

For Runs A and B, we find that the local peaks are very large and as the resolution is doubled, the value of the peak found in the higher resolution run is approximately twice as much as in the lower resolution run. Unfortunately, it is not currently possible to go above a resolution of 1024^3 due to severe limitations in computer time and memory. On the other hand, for Runs C and D, there is a convergence in local quantities within 10 to 20 % respectively (between C2 and C3, D2 and D3). A detailed resolution analysis is presented in Appendix B.

Such a sudden increase in the local quantities in the flow field naturally brings the

singularity arguments into the picture. We investigate the issue in detail in the next section.

4.2 Singularity Analysis

The regularity and uniqueness theorems for the three dimensional Euler and Navier-Stokes equations are far from being complete in literature. An important result is by Constantin ²⁰ who shows that the breakdown of smooth solutions to 3-D incompressible Navier-Stokes equations cannot occur without the corresponding solution of the incompressible 3-D Euler equations. Therefore, a possible singularity formation in our problem will have important implications on the formation of a singularity in 3D Euler equations.

We start with the evolution of ω_{max}^{-1} during the time interval $t=1.64-2.25$ given in Figure 20. The top figure shows the trend in two runs (B2 and A3) shortly before the peak vorticity is reached. We observe three intervals with different slopes in this figure. The first slope increase is around $t=1.78$ for Run B2 ($t=1.88$ for Run A3), and another increase around $t=1.93$ for Run B2 ($t=1.96$ for Run A3). If the evolution continues with this pace, it is clear that the function will hit the time axis and the local vorticity will diverge. We performed a least square fit in Figure 20 for the regions with the steepest slope and found that the time axis will be intersected at $T_c = 2.0389$ for Run B2 and $T_c = 2.1077$ for Run A3. However, as seen from Figure 20 (bottom), the ω_{max}^{-1} slope gets less steep, reaches a local minimum and starts to increase. We repeated the same analysis for our lower Reynolds number runs C and D and obtained similar results as

seen in Figure 21. Extrapolation of the curves to the x axis gives $T_c = 2.21$ for Run C3, and $T_c = 2.45$ for Run D3. Note that the slope in Figure 21 becomes steeper as approached to T_c similar as in the runs A and B.

It is important to investigate how ω_{max} and $(T_c - T)$ scale particularly during the interval with the steepest slope in Figure 20. This is presented in Figure 22 (recall that the T_c 's used are not the same for two runs). Least squares fitting for Run A3 between $t=1.9640-2.0515$ (using 8 data points) gives $\omega \sim (T_c - T)^{-1.09}$ and for Run B2 between $t=1.9265-1.9890$ (using 6 data points) gives $\omega \sim (T_c - T)^{-1.03}$. The power laws found depend slightly on the number of data points used in the fitting. This is a consequence of the fact that the points are not located exactly on a straight line but slightly curved. Taking various intervals and changing the number of points gave exponents between 0.9983 and 1.181 for all runs but never close to 2. We emphasize the fact that the highest resolution results are used to calculate the scaling and it is not possible to go above a resolution of 1024^3 to further check the resolution dependance of the exponents.

The scaling exponent found is similar to the scaling calculated by Kerr ^{17,21} in his single dipole simulation. Recently, Bhattacharjee and Wang ²² have suggested an analytical model of three-dimensional Euler flows which gives a singularity on a line joining two vorticity nulls. It is found that vorticity diverges as $(T_c - T)^{-1}$. A similar scaling is calculated by Grauer and Sideris ²³ in axisymmetric flows with swirl. However, Pumir and Siggia ²⁴ find a different scaling for a similar problem with higher resolution which is calculated to be $(T_c - T)^{-2}$.

Next, we examine the time evolution of the width of the analyticity strip δ . The width

δ is the distance of a complex-domain singularity to the real axis. It can be determined from the large wavenumber behavior of the energy spectra. For large wavenumbers, it can be shown ¹¹ that the leading term of the spectra is given by:

$$E(k, t) \sim \exp(-2\delta(t)k) \quad (24)$$

if δ remains finite in time. If, however, the width δ decreases to zero in finite time, a complex-domain singularity reaches the real axis and the spectra behaves like a power law in wavenumber given by

$$E(k, t) \sim k^{-n} \quad (25)$$

We calculated the temporal evolution of δ in all our simulations by performing least squares fitting assuming two different shape functions for the spectra. The first (we will refer to it as Type 1 fitting) is in the form as $\exp(-2\delta(t)k)$ and the higher end of wavenumber interval $100 < k < 340$ is used in the fittings for all runs. The second (we will refer to it as Type 2) is in the form $Ak^\alpha \exp(-2\delta(t)k)$ and the fitting is done for wavenumber intervals $3.5 < k < 340$ and $9.5 < k < 340$. The results obtained from these two intervals are almost the same for delta values. This can be seen in Figure 23 which gives the plots of the energy spectra of Run C3 at $t=2.3$ and two fit curves using the second type of fitting using the intervals $3.5 < k < 340$ (solid curve) and $9.5 < k < 340$ (dashed curve). As seen from this figure, the fit curve follows the points obtained from the simulation perfectly.

The energy spectra for two different times ($t=1.75$ and 2.25) for Run B2 are presented in Figure 24a. Figure 24b displays $k^3 E(k)$ and Figure 24c displays $k^4 E(k)$. Note that Figure 24c implies that somewhere between $t=1.75$ and 2.25 , the spectra will be nearly

horizontal line which indicates a scaling approximately as k^{-4} . Recall that at this instant, the whole flow field (fundamental box) has 3 dipoles near the origin and 3 near the $\pi/2$ corner. The dipoles can be considered as flattened vortex sheets with sudden vorticity jumps across them (vorticity changes sign across the flattened dipole sheet). The configuration is similar to Saffman's ²⁵ vorticity field with random two-dimensional vorticity discontinuities which also gives a k^{-4} scaling. As the structure breaks down, the spectra evolves towards k^{-3} but continues to change. Therefore, k^{-3} scaling might be only a transient intermediate stage as the cascade evolves into the Kolmogorov regime at later times (A.Pouquet, private communication).

Returning to the δ argument, we present the temporal behavior of the analyticity width in Figure 25 (Type 2 fitting), and display the results in log-log scale. The δ values found using the Type 1 fitting are found to be qualitatively the same and quantitatively slightly larger than those calculated by Type 2 fitting. The horizontal dashed line in Figure 25 shows twice our effective resolution.

One interesting observation from Figure 25 is the existence of the regions of different slopes for all four runs. For Run A3, after the first sharp drop in δ , there is a region of almost constant slope between $t=1.789-1.9765$ (recall that our predicted $T_c = 2.1077$ for this run) and another region with a steeper slope between $t=1.98-2.1$ after which the curve hits a minimum value at $t=2.1265$. The width starts to increase after this time. A similar trend is seen for Run B2. After the initial wiggly region, the curve shows a constant slope between $t=1.7765-1.8265$ (recall that the predicted $T_c = 2.0389$ for Run B2). After $t=1.83$, it seems like the decrease in δ slows down. This slow decrease in

δ continues until $t=1.964$. After this time, there is a decrease in the slope which stays uniform between $t=1.964-2.064$. At $t=2.064$, the curve reaches to its minimum value. Similarly for the lower Reynolds number runs C and D, the region with the steeper slope is between $t=2.15$ and 2.32 for Run C3 and $t=2.02$ and 2.2 for Run D3.

We emphasize that in all these runs, we obtain regions of different slope as the time evolution of ω^{-1} and δ are examined. Since such similar trends are also observed in Runs C and D which are much better resolved than A and B, we conclude that the results cannot be an artifact of a possible resolution problem.

The rate at which δ decreases is almost the same in three runs (A3, B3, D3) and slightly slower in Run C3 (Figure 25). The critical times (T_C) is at a later time as Reynolds number is increased. Similar results are obtained in vortex reconnection runs ¹³. We make the following observations: i) In two different studies by Brachet et al. ^{6,7}, δ evolution with time seems to exhibit an exponential decrease. However, there are hints that such a trend might change after a certain time. Brachet et al. ^{6,7} always considered the formation of a finite time singularity possible, stating that 'A more singular behaviour due to subsequent instabilities of the above structures is however not excluded' ⁷. Such an interval with a faster than exponential rate is what we observe in our simulations. ii) We find that δ has a non-zero minimum in our simulations. This suggests that the solution is uniformly analytic. This is the case for the viscous Burgers equation which also gives a δ decrease to a minimum and a subsequent linear increase (Figure 3 in Reference 11).

Next, we focus on the spatial location of the local maximum vorticity. We find that

in all our runs the maximum is located at the zero planes of the flattened vortex tubes and more specifically in the “*head region*” of the vortices. We present in Figures 26-31 the magnitude of vorticity contours at different times for runs A3 and B2 (Recall that we have presented the pictures for Run A at earlier times in Figure 13). We start with Run B2, Figures 26-28. We observe that the vortex head deforms in a self-similar way until $t=1.937$. After this time, for example at $t=2.0$, the self-similarity is lost in the sense that the vorticity contour pictures can not be generated by only stretching and compressing the pictures at an earlier time. For Run A3, a similar picture appears with a slight delay in time. As seen from Figures 29 and 31, vorticity contours seem to be self-similar until $t=2.0$. After this time, the self-similarity is lost (for example; the contours at $t=2.062$, Figure 31). To quantify this process, we have calculated the distance between the location of the maximum vorticity and the origin for both runs. The results are given in Figure 32 which displays the natural logarithm of the distance as a function of time. We see in Figure 32 that for both runs, there is an interval when the distance decreases linearly (in logarithmic scale) which implies an exponential shrinkage with time. This interval is until $t=1.939$ for Run A3 and $t=1.9015$ for Run B2. But the curves do not continue with the same trend, and after the exponential period a saturation is observed. This is an interval between $t=1.939-2.0015$ for Run A3 and $t=1.9015-1.939$ for Run B2. To see the process clearly, we present in Figure 33 the trajectory connecting the location of the points with maximum vorticity at different times (equally spaced in time) for both runs. It is seen from this figure that the approach of the maxima towards the origin halts for some time during the evolution. This surprising “*saturation*” is similar

to the “*bouncing-off*” process of two vortex rings which are shot towards one another. In this interaction, there is a minimum intercentroid distance of the vortices after which the vortices change direction and divert their paths. The saturation process might also be related to a competition between the stretching and dissipation processes. There is an interval when these forces approximately balance each other and a local equilibria is attained as in the case of viscous Burgers vortex. However, it looks like the equilibria is not stable, the structure breaks down.

Now, it might be interesting to compare the results of the time scale analysis we have at different sections of this work: For Run A3, we observe a faster than exponential shrinkage (in distance to origin) for $t > 2.0015$. The self-similarity is broken around this time (Figures 30, 31), the analyticity strip δ has its fastest decrease rate (between $t=1.98-2.1$), and a possible singular time is predicted to be at $T_c = 2.1077$. Similarly for Run B2, we find a faster than exponential shrinkage rate for $t > 1.95$, the self-similarity is broken at this time (Figure 31), δ attains its steepest slope between $t=1.964-2.064$, and a possible singularity time is predicted to be at $T_c = 2.0389$. In spite of all these trends towards a singularity, both δ and ω_{max} remain bounded after the violent deformation period. We propose the following scenario: i) The 6 vortex dipoles deform one another, their cores get more and more flattened, the distances shrink exponentially. ii) There is a short local equilibrium interval when the viscous forces and vortex stretching forces balance each other. iii) The intermediate state is likely to be unstable, the vortices start to break up by an instability mechanism which is not well-understood, but a viscosity-induced stability is not discarded. iv) Viscous dissipation takes over, trends towards

a singularity are damped down. v) In the runs with higher Reynolds numbers, we do not observe vortex reconnection. In Run C ($Re = 500$) we do see evidence of multiple reconnections, but further analysis is necessary. If vortex reconnection does occur, it would be a mechanism against the formation of a singularity by changing the extremely flattened sheet-like vortices back to their original tubular topology and hence decreasing the existence of the high gradient regions.

One final check to be made to strengthen the above argument will be to determine at which length scales the viscous time scales will be comparable to the convective (deformation) time scales in the problem. For this, we refocus on Figure 32 and particularly on the region where there is exponential shrinkage in length. For Run A3, this is an interval of $\Delta t \simeq 1.939 - 1.639 = 0.3$ and for Run B2, $1.9015 - 1.7015 = 0.2$. Hence, we will use these time intervals as the convective time scale in the deformation process. The viscous time scale, on the other hand, is given by $1/(\nu k^2)$. Equating the convective time scale T_{conv} ($=0.2$ for Run B2 and $=0.3$ for Run A3), to the viscous time scale, we obtain the wavenumber at which the dissipative forces have comparable time scales as the convective forces. This is found to be $k = 82$ for Run A3 and $k = 158$ for Run B2. The corresponding length scales can be evaluated using $L = 2\pi/k$ and one obtains $L = 0.0766$ for Run A3 $L = 0.0398$ Run B2. The grid size is given by $\Delta x = (\pi/2)/256 = 0.0061$. Hence, the dissipative time scale becomes comparable to convective time scale at 13 gridpoints for Run A3 and 7 gridpoints for Run A2. To show the resolution clearly, we display in Figure 28 (Run B2) and Figure 31 (Run A3) the vorticity contour sections at $z = 0$ plane. For Run B2, we see that 7 gridpoint limit

is reached somewhere between $t = 1.937$ and 2.0 . For Run A3, the 13 point limit is reached somewhere between $t = 2.0$ and 2.062 . Once these limits are reached, viscous dissipation forces will play a role against the singularity formation as rapidly as the convective forces play towards a singularity.

Finally in this section, we will examine the evolution of enstrophy and skewness in more detail. It has been shown by Kida and Murakami⁹ (Figure 2) and confirmed by the present work that the time at which the enstrophy attains its maximum value depends weakly on Reynolds number. For higher Reynolds number, the time of the enstrophy peak is later than that of the lower Reynolds number, but the difference is slight. The Reynolds number based on Taylor microscale, R_λ is initially 674 for Run A and 1685 for Run B. Our results are in agreement with the recent work by Herring and Kerr²⁶ who observed a similar trend in the time of the peak enstrophy.

The initial growth of the enstrophy for all runs seems to be at least exponential. This can be seen from Figure 3, 17 and 19 which approximately give a linear result when the enstrophy evolution is plotted on a log-lin scale. The graphs have a slight concavity which suggests that the rate might be slightly faster than exponential. Another interesting feature is the slight dimple observed during the evolution. This is around $t=2.06$ for Run B2 and $t=2.11$ for Run A3. It is clearly seen in Figure 19. Thus, we conclude that the enstrophy increase rate changes after the break up of the structure. If the viscous terms are ignored, and isotropy is assumed, enstrophy rate can be related to the velocity derivative skewness, so we might also expect a change in the skewness as the cause of the enstrophy rate change. This is indeed the case, and we find sharp

skewness fluctuations around $t=2.0640$ for Run B2 and $t=2.1265$ for Run A3. The time at which the peak is attained is at an earlier time for the higher Reynolds number run. Such a trend is also observed in the Taylor-Green simulations by Brachet et al.⁶ (See their Figure 10).

It is a common practice to assume isotropy in calculating the skewness, since the quantity can directly be related to enstrophy for the inviscid case given by

$$S = \left(\frac{135}{98}\right)^{1/2} \frac{d\Omega/dt}{\Omega^{3/2}} \quad (26)$$

We have compared the skewness results obtained from the above equation and Equation 9. We observed major differences between them particularly during the intermittent interval. For example, for Run B2, the skewness value calculated directly is 0.52 at $t=4$ compared to 0.00193 obtained using the isotropic relation. Such a low value is due to the fact that the enstrophy increase rate is very slow around that time, giving extremely low skewness values. Such a discrepancy is not surprising since one observes that close to the break up, there are two local regions where all the action is concentrated (0 and $\pi/2$ planes) and therefore the flow is strongly anisotropic and the skewness values obtained using Equation 26 assuming isotropy do not give realistic values. Similarly, Taylor-Green flow simulations suggested a strong anisotropy before the break up (See Figure 8a in Reference 6).

Finally, we make an observation on the influence of the resolution on the skewness and flatness. We have concluded before that Run B1 is underresolved around $t=2$. A comparison of the skewness values for Run B1 and B2 shows that the two runs approach asymptotically to different values after the break up, Run B1 approaches to 0.44 and

Run B2 to 0.5. There is also divergence in flatness values. Run B1 approaches to 5.2 whereas Run B2 tends to 7.5 after $t=2$. Such a divergence brings questions about the calculated turbulence statistics by Kida and Murakami after the break down, since their maximum resolution is as much as our Run B1 resolution. One other possibility is that these values will converge to the same value at the later times. We remind the reader that Kida and Murakami's runs are longer in time than the present work. To check this, we continued Run B2 up to $t=6$ and found that the skewness is 0.5295 and the flatness is 5.65 at this instant. The values have not converged yet at this time.

5 Conclusions

The present work is an attempt to show the similarities and differences between the high-symmetry initial condition and several other flows in literature such as the Taylor-Green vortex and the vortex reconnection problems. We find the following similarities in all these flows:

1. All of these flows examine the vortex tubes which are moving towards one another.

The topology is simpler in the vortex reconnection problems since there are only two vortex tubes in the field. In both Taylor-Green and high-symmetry flows, more than one dipole exists in the domain. All of these problems result in the extreme deformation (flattening) of (at least one) a dipole, which is moving towards the origin during the deformation process. The origin is a vorticity null point in Taylor-Green and high-symmetry flows but such a constraint is not imposed in the vortex

reconnection problem.

2. During the interaction, there is an interval during which local quantities such as maximum vorticity and strain rate and integrated quantities such as velocity derivative skewness and flatness increase sharply. The increase is so sudden and sharp that questions arise as to whether some of these quantities would diverge in finite time or not. This interval of extreme intermittency takes place before the peak in enstrophy and total dissipation is reached.
3. For viscous simulations, both for the vortex reconnection problem^{13,17}, Taylor-Green vortex and the high-symmetry flow, as the Reynolds number is increased, the amplitude of maximum vorticity, skewness and flatness increase and the peaks are attained at an earlier time. This is a tendency which shows hints that for the inviscid case, all these quantities will blow up.
4. During this intense period, all the flow statistics are far away from any Kolmogorov-type scaling laws. The energy spectra behave as k^{-4} and evolves towards k^{-3} . Flow is extremely anisotropic. Skewness and flatness values are much higher than those obtained in fully developed turbulent flow simulations.

There are also differences encountered among the above-mentioned studies. We summarize these as:

1. In the presence of viscosity, no singularity formation is observed in any of the studies. However, both viscous vortex reconnection^{13,18} and the present work shows trends towards a singularity for the inviscid case. Such a trend is not supported by

the Taylor-Green simulations^{3,7} and the reasons for the disagreement are not clear.

The differences between the present work and the viscous Taylor-Green simulations are; slightly higher resolution in the present work and a more complicated flow topology in the high-symmetry flow compared to the Taylor-Green flow. In fact, the violent flow evolution configuration in high-symmetry flow which is as a result of twelve converging vortices towards the origin is not present in the Taylor-Green initial conditions.

2. Even though we observe tendencies towards a singularity, the presence of viscosity damps the process down. In vortex reconnection problems, vortex line topology changes during reconnection, resulting in the formation of new tubular vortices. The flattened remnants are rapidly dissipated by enhanced dissipation^{13,18}. In the present work, the structure breaks down followed by a similar dissipation process acting against the singularity formation.

It is interesting to see whether the violent peaks observed in the simulation of the high-symmetry flow can be avoided by slightly perturbing the flow field. To check this, we have added some random noise (5 %) to the Run C2 at $t=2.0$ and also at $t=2.25$ (separately) and continued the flow. We compared the local maximum vorticity, skewness and also the vorticity isosurfaces and contours (at 0 and $\pi/2$ planes) between the two runs with and without the noise. We did not observe any significant change in our results.

A natural question is to discuss what influence the symmetries have on our results. We tend to believe that flows like Taylor-Green flow and high-symmetry flow with all the symmetry constraints are unstable and in the absence of the symmetries, the flow

will escape from the singularity formation direction. We remind the reader that such a trend due to axisymmetry is also suggested by Pumir and Siggia²⁷. It is not easy to check this since performing a well-resolved simulation without imposing the symmetries requires many more modes than the current computers can provide. But it has been observed that marching towards or away from a singularity strongly depends on how the initial conditions are set up²¹. Even the numerical method chosen might have influence on the results. Finite difference solutions which do not make use of any symmetry do not give any singularity formation²⁷ whereas Fourier-Chebyshev method simulations which impose symmetry constraints intrinsically in the code obtain a singular trend²¹ for the same problem.

Acknowledgements

This work is fully supported by the Air Force Grant (AFOSR-91-0248). The authors would like to thank to R. Kerr, S. Kida, A. Bhattacherjee, A. Pouquet, N. Zabusky, P. Sulem, U. Frisch, and A. Pumir for the exciting discussions. M. Brachet kindly provided his code which we used as a guide in implementing the flow symmetries in the present work's initial condition. One of the authors (O. B) thanks Dr. E. Eşkinat for his helps in curve-fitting calculations. The authors would also like to thank the director of the Institute of Theoretical Physics at University of California at Santa Barbara, James Langer and the directors of the NATO workshop on topological fluid dynamics, Keith Moffat and Michael Tabor for inviting them to the workshop and to the Institute. Computations were done on the Cray 2 at the Kirtland Supercomputer

Center, supported by the US Air Force and on the Cray Y-MP and C-90 of the Pittsburgh Supercomputing Center supported by the National Science Foundation. The final part of this work was completed when one of the authors (O. B.) was a Henri-Poincare fellow at the Observatoire de Nice supported by C. N. R. S.

References

¹S. Kida, "Three-Dimensional Periodic Flows with High-Symmetry", *J. Phys. Soc. Jpn.*, **54(6)**, 2132 (1985)

²L. D. Landau and E. M. Lifshitz, *Fluid Mechanics*, Pergamon Press, 4th Edition, 123 (1975)

³G. I. Taylor and A. E. Green, "Mechanism of the Production of Small Eddies from Large Ones", *Proc. Roy. Soc. A* **158**, 499 (1937)

⁴M. E. Brachet, "Direct Simulation of Three-Dimensional Turbulence in the Taylor-Green Vortex", *Fluid Dy. Res.*, **8**, 1 (1991)

⁵S. A. Orszag, "Numerical Simulation of the Taylor-Green Vortex", in *Proc. Symp. on Computing Methods in Applied Sciences and Engineering* (ed. R. Glowinski & J. L. Lions), part II, p.50, Springer-Verlag, 50 (1974)

⁶M. E. Brachet, D. I. Meiron, S. A. Orszag, B. G. Nickel, R. H. Morf, U. Frisch, "Small-scale Structure of the Taylor-Green Vortex", *J. Fluid. Mech.*, **130**, 411 (1983)

⁷M. E. Brachet, M. Meneguzzi, A. Vincent, H. Politano, P. L. Sulem, "Numerical Evidence of Smooth Self-Similar Dynamics for Three-Dimensional Ideal flows", *Phys. Fluids*, **4(12)**, 2845, (1992)

⁸S. Kida and Y. Murakami, "Kolmogorov's Spectrum in a Freely Decaying Turbulence", *J. Phys. Soc. Jpn.*, **55(1)**, 9 (1986)

⁹S. Kida and Y. Murakami, "Kolmogorov Similarity in Freely Decaying Turbulence", *Phys. Fluids*, **30(7)**, 2030 (1987)

¹⁰R. H. Morf, S. A. Orszag and U. Frisch, "Spontaneous Singularity in Three-Dimensional

Inviscid, Incompressible Flow", Phys. Rev. Letts., **44(9)**, 572 (1980)

¹¹C. Sulem, P. Sulem and H. Frisch, "Tracing Complex Singularities with Spectral Methods", J. Comp. Phys., **50**, 138 (1983)

¹²S. A. Orszag, "Numerical Simulation of Incompressible Flows Within Simple Boundaries, I. Galerkin Representations", Stud. Appl. Math., **50**, 293 (1971)

¹³O. N. Boratav, R. B. Pelz and N. J. Zabusky, "Reconnection in Orthogonally Interacting Vortex Tubes: Direct Numerical Simulations and quantifications", Phys. Fluids A, **4(3)**, 581 (1992)

¹⁴J. W. Cooley and J. W. Tukey, "An Algorithm for the Machine Calculation for Complex Fourier Series", Math. Comput., **19**, 297 (1965)

¹⁵J. W. Cooley, P. A. Lewis, P. Welch, "The Fast Fourier Transform algorithm: Programming Considerations in the Calculation of Sine, Cosine and Laplace transforms", J. Sound. Vibr., **12**, 315 (1970)

¹⁶ While the manuscript was in the reviewing process, we checked the cpu time/timestep for the new C-90 machine at Pittsburgh. For Runs C1, C2 and C3, the cpu /timestep are found to be 0.19, 2.8, 25.0 seconds respectively. This is more than twice faster compared to the Y-MP.

¹⁷R. M. Kerr, "Evidence for a Singularity of the Three Dimensional, Incompressible Euler Equations", Topological Aspects of Dynamics of the Fluids and Plasmas, Moffat, Zaslavsky, Tabor, Comte (eds.), Kluwer Academic Pub., (1992).

¹⁸O. N. Boratav, R. B. Pelz and N. J. Zabusky, "On Vortex Reconnection and Turbulence", Topological Aspects of the Dynamics of Fluids and Plasmas, Moffat, Zaslavsky,

Tabor, Comte (eds.), Kluwer Academic Pub., (1992).

¹⁹A. Domaradzki, W. Liu and M. Brachet, "An Analysis of Sub-grid Interactions in Numerically Simulated Isotropic Turbulence", *Phys. Fluids A*, **5**(7), 1747 (1993).

²⁰P. Constantin, "Note on Loss of Regularity for Solutions of the 3-D Incompressible Euler and Related Equations", *Commun. Math. Phys.*, **104**, 311 (1986).

²¹R. M. Kerr, "Evidence for a Singularity of the Three Dimensional, Incompressible Euler Equations", *Phys. Fluids A*, **5**(7), 1725 (1993).

²²Bhattacharjee, A. and Wang, X., "Finite-time Vortex Singularity in a Model of Three-Dimensional Euler Flows", *Phys. Rev. Lett.*, **69**(15), 2196 (1992).

²³Grauer, R. and Sideris, T., "Numerical Computation of three-dimensional Incompressible Ideal Fluids with Swirl", *Phys. Rev. Lett.*, **67**, 3511 (1991).

²⁴Pumir, A. and Siggia, E., "Development of Singular Solutions to the Axisymmetric Euler equations", *Phys. Fluids A*, **4**(7), 1472 (1992).

²⁵Saffman, P. G., "On the Spectrum and Decay of Random Two-Dimensional Vorticity Distributions at Large Reynolds Numbers", *Studies App. Math.*, **50**(4), 377 (1971).

²⁶Herring, J. and Kerr, R., "Development of Enstrophy and Spectra in Numerical Turbulence", *Phys. Fluids A*, **5**(11), 2792 (1993).

²⁷Pumir, A. and Siggia, E., "Collapsing Solutions to the 3-D Euler Equations", *Phys. Fluids A*, **2**, 220 (1990).

Table No.I
High-symmetry Runs in Literature

Author(s)	$Re = 1/\nu$	R_λ	Total Resolution	Independent Modes	k_{max}
Orszag ⁵	300	37	32^3	8^3	16
Brachet et al. ⁶	$3000, \infty$	110	256^3	42^3	84
Brachet ³	5000	140	864^3	144^3	288
Kida and Murakami ⁸	2000	90	512^3	85^3	171
Kida and Murakami ⁹	5000	143	512^3	85^3	171
Present Work	5000	143	1024^3	171^3	341

Table No.II
Parameters of Study

Run	$Re = 1/\nu$	Δt	Resolution	(t_i, t_f)
A1	2000	0.001	256^3	(0,2.25)
A2	2000	0.001	512^3	(0.785,2.25)
A3	2000	0.0005	1024^3	(1.625,2.25)
B1	5000	0.001	512^3	(0,6.0)
B2	5000	0.0005	1024^3	(1.625,6.00)
C1	500	0.001	256^3	(0,2.5)
C2	500	0.001	512^3	(0.8,2.5)
C3	500	0.001	1024^3	(1.55,2.5)
D1	1000	0.001	256^3	(0,2.25)
D2	1000	0.001	512^3	(0.8,2.25)
D3	1000	0.001	1024^3	(1.55,2.25)

Table No.III
Memory and Time Requirements

Resolution	Machine	Memory-Mwords	Cpu secs./timestep
256^3	Cray 2	2.9	2.0
256^3	Cray Y-MP	2.9	0.8
512^3	Cray 2	18.5	10.0
1024^3	Cray 2	139.5	80.0

Figure Captions

Figure 1: Vorticity magnitude isosurfaces for Run B at $t=0, 0.2$ (top row, $\hat{\omega} = 0.3\omega_0$), $0.5, 0.75$ (bottom row, $\hat{\omega} = 0.49\omega_0$).

Figure 2: Same as previous figure, different view.

Figure 3: Run B1, Top: Energy and enstrophy. Bottom: Dissipation and Taylor Reynolds number.

Figure 4: 4a and b: Run B1, energy spectra at $t=6$. Fig.4a: $E(k)$. Fig.4b: $k^{5/3}E(k)$, Fig.4c: Run B2, $k^{5/3}E(k)$ at six different times between $t=5.75$ and 6.0 .

Figure 5: Run B1, Kolmogorov wavenumber.

Figure 6: Symmetries at a XY plane, $z=\pi/2$. Top: ω_x and ω_y . Bottom: ω_z and magnitude of vorticity. Run A2, $t=1.25$.

Figure 7: Vorticity magnitude isosurfaces for Run B at $t=1.25, 1.5, 1.75, 1.8125$, $\hat{\omega} = 1.25\omega_0$).

Figure 8: Same as previous figure, different view.

Figure 9: Vorticity magnitude isosurfaces for Run B at $t=1.875, 1.9375$ (top row, $\hat{\omega} = 2.5\omega_0$), $2.0, 2.0625$ (bottom row, $\hat{\omega} = 6.25\omega_0$).

Figure 10: Same as previous figure, different view.

Figure 11: Vorticity magnitude isosurfaces for Run B at $t=2.125, 2.5, 3.0, 3.5$ ($\hat{\omega} = 6.25\omega_0$).

Figure 12: Same as previous figure, $t=4.0, 6.0$.

Figure 13: Magnitude of vorticity contours at $z=0$ section for Run A, $t=0.75, 1.0, 1.25, 1.5$. A similar picture exist for $x=0$ and $y=0$ planes.

Figure 14: Magnitude of vorticity contours at $z=\pi/2$ section for Run A, $t=1.25, 1.5, 1.625, 1.75$. A similar picture exist for $x=\pi/2$ and $y=\pi/2$ planes.

Figure 15: Same as previous figure, at $t=1.8125, 1.9375, 2.0, 2.0625$.

Figure 16: Same as previous figure, at $t= 2.125, 2.5$.

Figure 17: Evolution of energy E , enstrophy, Ω , Kolmogorov wavenumber k_ν , and Taylor Reynolds number R_λ for Run B1 (dashed) and Run B2 (solid).

Figure 18: Evolution of velocity derivative skewness S , flatness F and maximum vorticity ω_{max} , for Run B1 (dashed) and Run B2 (solid).

Figure 19: Comparison of two high-resolution runs. Solid: Run B2. Dashed: Run A3. Velocity derivative skewness S , flatness B , maximum vorticity ω_{max} , energy E , enstrophy Ω (Lin-Lin), enstrophy Ω (Log-Lin)

Figure 20: ω^{-1} evolution to determine the trend towards a singularity, Run B2 (solid), Run A3 (dashed). Top: Before dissipation takes over. Bottom: After the peak vorticity is reached. Fitting for the top figure gives $T_c = 2.039$ for Run B2 and $T_c = 2.108$ for Run A3.

Figure 21: ω^{-1} evolution to determine the trend towards a singularity, Run D3 (solid), Run C3 (dashed).

Figure 22: Scaling of ω_{max} and $(T_c - T)^{-1}$ for Run B2 (solid, $T_c = 2.039$) and for Run A3 (dashed, $T_c = 2.108$).

Figure 23: Calculated and fit energy spectra at $t=2.30$ for Run C3. Solid: $3.5 < k < 340$, Dashed: $9.5 < k < 340$, Short Dashed: Simulations.

Figure 24: Energy spectra at $t=1.75$ (pluses) and $t=2.25$ (triangles) for Run B2. Figure

24b: $k^3 E$. Figure 24c: $k^3 E$. The spectra evolves from k^{-4} to k^{-3} during the break up.

Figure 25: Evolution of the width of the analyticity strip δ for Run A3 (long-dashed), B2 (solid), C3 (dot-dashed), D3 (short-dashed), (Type 2 fitting). The dashed horizontal line indicates twice the effective grid size. Log-Log scale.

Figure 26: Vorticity contours at $z=0$ (location of peak vorticity) at $t=1.75, 1.8125, 1.875, 1.9375$, Run B2. The ratio of the axes in each figure is drawn to scale. But note that the last two figures have coordinates half of the first two for clarity. The numbers in the axes show the grid points.

Figure 27: Same as previous figure at $t=2.0, 2.0625$.

Figure 28: Same as Figures 28 and 29 the x axis stretched to show the structures in more detail.

Figure 29: Vorticity contours at $z=0$ (location of peak vorticity) for Run A3 at $t=1.875, 1.9375, 2.0$.

Figure 30: Same as previous figure, at $t=2.0625, 2.125$.

Figure 31: Same as Figures 31 and 32, the x axis stretched to show the structures in more detail.

Figure 32: Evolution of the distance from the origin of the location of the maximum out-of-plane vorticity (ω_z). Solid: Run B2. Dashed: Run A3.

Figure 33: The location of the maximum out-of-plane vorticity (ω_z) between $t=1.7015-2.0640$ Run B2 (left figure) and between $t=1.6390-2.2140$ Run A3 (right figure). Each marker is equally spaced in time.

Figure 34: Energy spectra for Run C1 (solid), C2 (dot-dashed) and C3 (dot) at $t=2.35$.

Figure 35: Evolution of Kolmogorov wavenumber k_n for Run C1 (squares), C2 (triangles) and C3 (circles).

Figure 36: Evolution of enstrophy for Run C1 (squares), C2 (triangles) and C3 (circles).

Figure 37: ω^{-1} evolution to determine T_c for Run B1 (dashed) and Run B2 (solid).

Figure 38: Evolution of ω_{max} for Run C1 (squares), C2 (triangles) and C3 (circles).

Appendix A

Examining a singularity by computation is analogous to a classical tragic drama; one knows from the start that eventually the loss of resolution will knock the solution off the singular evolution trajectory and doom the calculation.

When one attempts to integrate through a singularity, convergence tests will obviously fail, but how they fail may give an indication of the type of singularity. As an example, consider the approximation of a delta function with a finite Fourier series. The Fourier coefficients are all equal to a constant which is denoted by C. The delta function can be written as follows:

$$\delta(x) = \lim_{j \rightarrow \infty} C f_j(x) \quad (27)$$

where

$$f_j(x) = \sum_{n=0}^{jN} \exp(-inx). \quad (28)$$

and $i = \sqrt{-1}$. Since $f_j(x)$ is a geometric series, its sum can be found as

$$f_j(x) = [1 - \exp(-ijN x)]/[1 - \exp(-ix)]. \quad (29)$$

The maximum absolute value of f_j , $j = 0, 1, \dots$ occurs at $x = 0$. In the limit as $x \rightarrow 0$ and through the use of l'Hopital's rule, one finds

$$\|f_j(x)\|_\infty = \lim_{x \rightarrow 0} f_j(x) = jN. \quad (30)$$

The expression above shows that if one is trying to resolve a delta function with a finite Fourier series, each doubling of the number of modes or resolution will cause doubling of the maximum value. Similarly, the maximum value upon doubling of resolution for the representation of the nth derivative of a delta function will scale as $(jN)^{n+1}$.

While the doubling behavior at the critical time that we have observed in our simulations is a necessary condition for the true function to be a delta function, it is not proved to be a sufficient condition. Other generalized functions may have a similar scaling, and a function that is continuous but appears to be a delta function in the resolution range over which the convergence is investigated may also have this behavior.

Appendix B: Resolution Checks

In this section, we present the resolution checks performed for each run at different instants. We systematically checked the following quantities in our runs:

1. Spectral convergence for different resolutions. (Energy spectra for three different resolutions).
2. High wave-number end of the spectra, to see whether there is a flip-up in the energy in this region.
3. Comparison of the maximum resolved wave-number k_{max} with the Kolmogorov wave-number k_η .
4. Convergence checks for total energy, enstrophy, dissipation and the Reynolds Number based on Taylor microscale (for different resolutions).
5. Convergence checks for local maximum vorticity, skewness and flatness (for different resolutions).
6. Evolution of δ for different runs.
7. Physical picture check. Checking the number of gridpoints across the vortices in vorticity contours.
8. Physical picture check. Checking the vorticity contours and isosurfaces for different resolutions.

The Checks 1 and 2 showed that all runs are spectrally converged. The flip-up in the spectra is observed to be the highest around the time of the singularity and decreases as approached to the time of peak enstrophy. As an example, we present in Figure 34 the energy spectra for Run C (for 3 different resolutions) at $t=2.35$ (close to the peak in maximum vorticity).

Check 3 showed that k_{max} is around 240, 140, 89, 55 for Runs B, A, D and C respectively around the time of peak local vorticity (Recall that the maximum wavenumber for the highest resolution is 341). These values increase further as the flow approaches to peak in enstrophy (for example 323 for Run B2). The check shows that Run B2 is in the limit of resolution (323 vs 341) while Runs A3, C3, D3 are sufficiently resolved. We present in Figure 35 the Kolmogorov wave-number for three different resolutions in Run C. We find that the three runs differ by less than 1 %.

Check 4 for Run B was already mentioned in the text; we recall that the comparison of the different resolutions shows that the energy differs by less than 1%, enstrophy less than 5%. This error is even less for the lower Reynolds number runs. The results for C are shown in Figure 36.

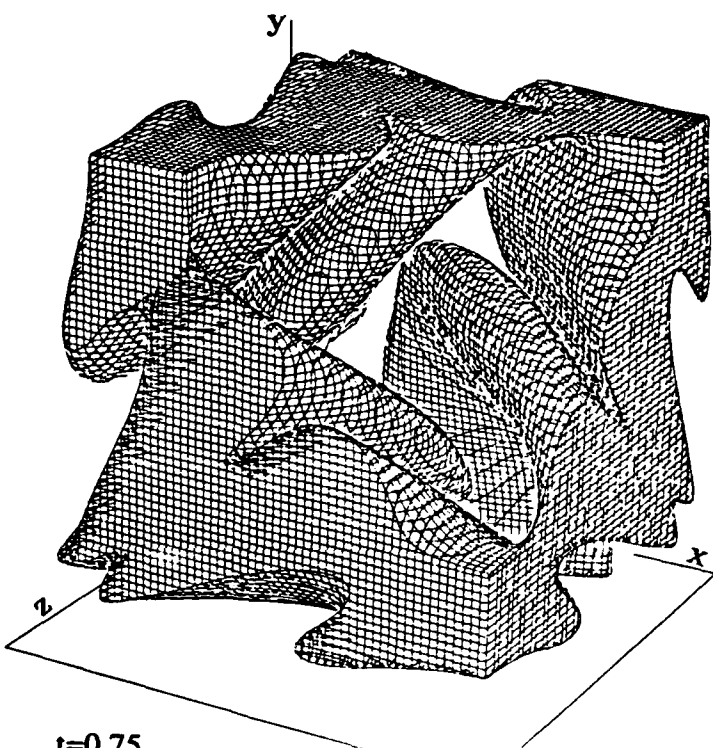
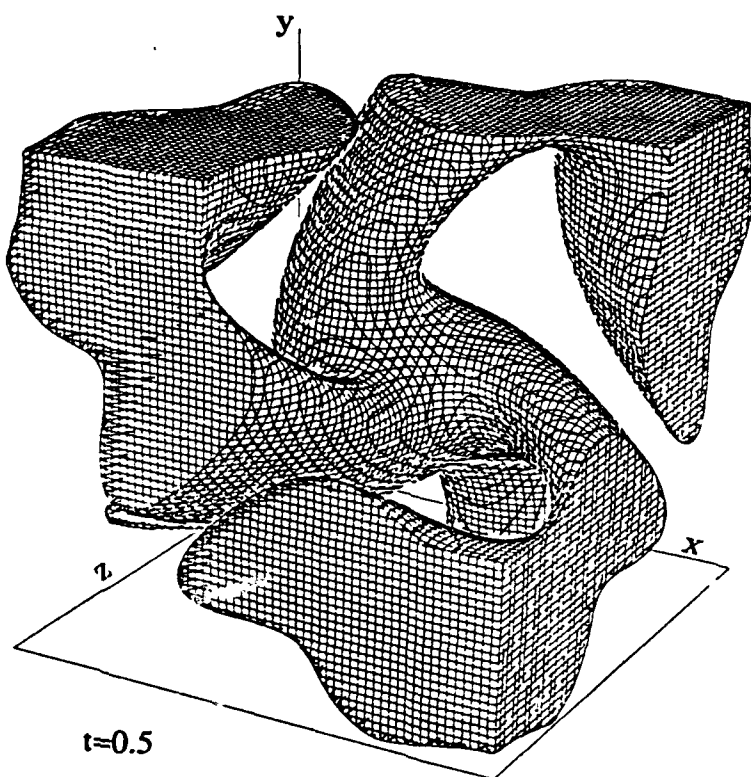
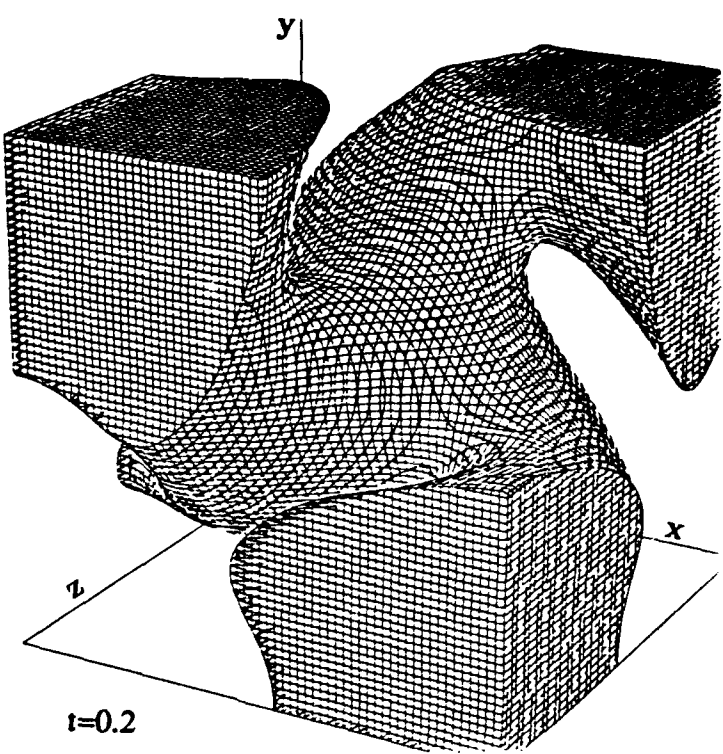
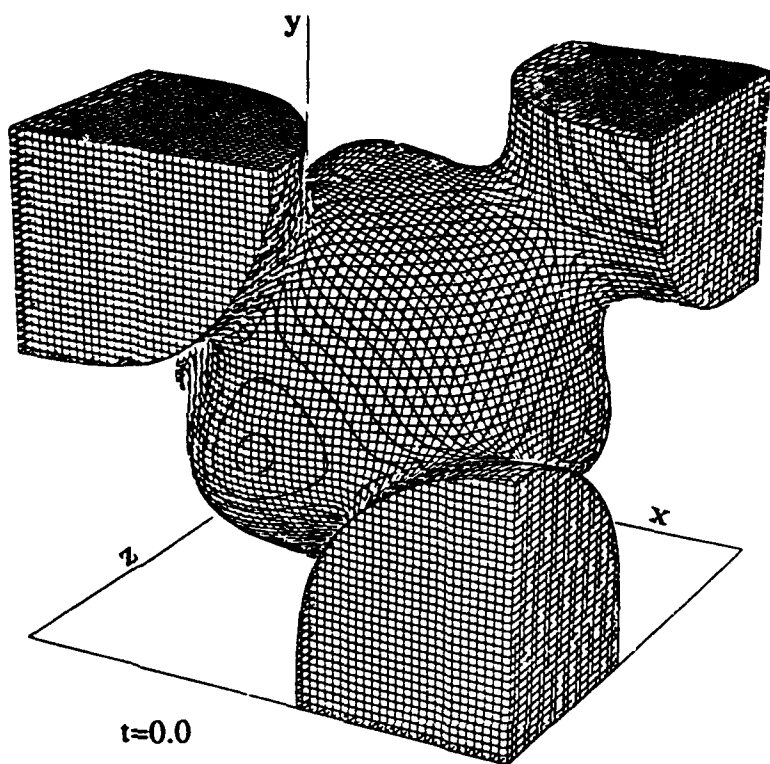
Check 5 for Runs A and B have given discrepancies in runs of different resolutions as mentioned before. We, in fact, find that all the values increase with the same rate up to a certain time after which the increase further continues for the highest resolution run which reaches to a higher peak. While calculating the T_c values for these runs, we plotted the ω^{-1} as a function of time for two resolutions. The tangent is drawn in such a way that the line passes through a region with the maximum number of common points

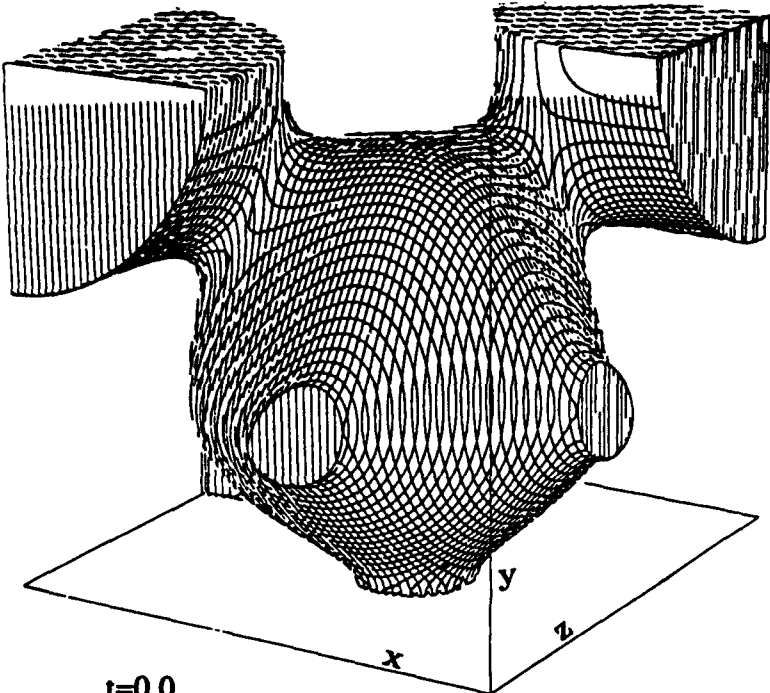
possible. Figure 37 gives the plot for runs B1 and B2. The scaling exponents found as such showed that the powers for the two cases are close to one another. For Runs C and D, a better convergence is attained and the convergence in local quantities is within 10 to 20 % respectively (between C2 and C3, D2 and D3). As an example, we present in Figure 38 the local maximum vorticity evolution for Runs C1, C2 and C3.

Check 6 showed that the time evolution of δ is very similar in different runs, the regions of different slopes are observed in all cases. It is also seen that δ values from run B3 is very close to the double resolution run. The δ values are calculated using only the 1024^3 resolution runs because of having a much wider exponential high k region in these runs.

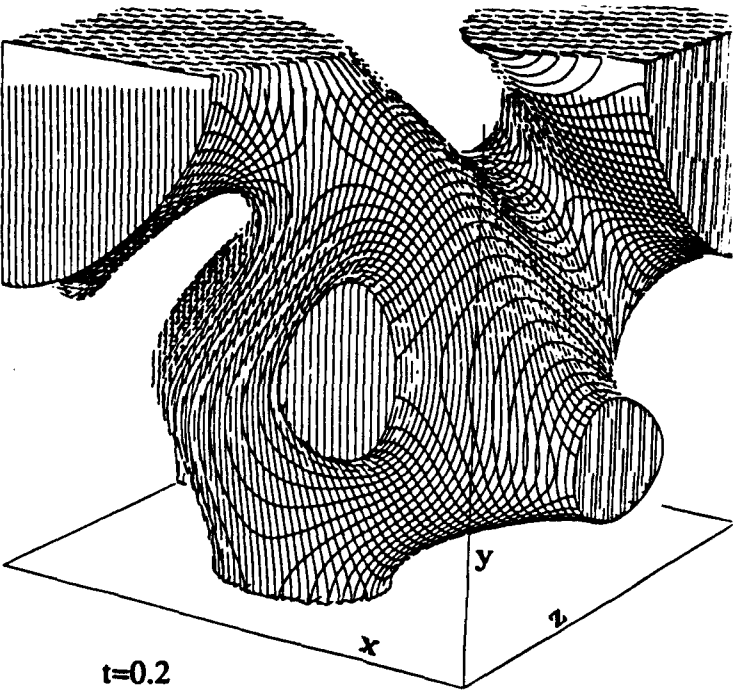
Check 7 has shown that the number of grids used to resolve a flattened vortex is around 7 for Run B2, 12 for Run D3 and 17 for Run C3.

Check 8 showed that both the isosurfaces and the vorticity contours show similar pictures for all runs as the vortices are flattened and approach to 0 and $\pi/2$ corners. The amount of small-scale production however is much less in run C3 compared to the other three runs.

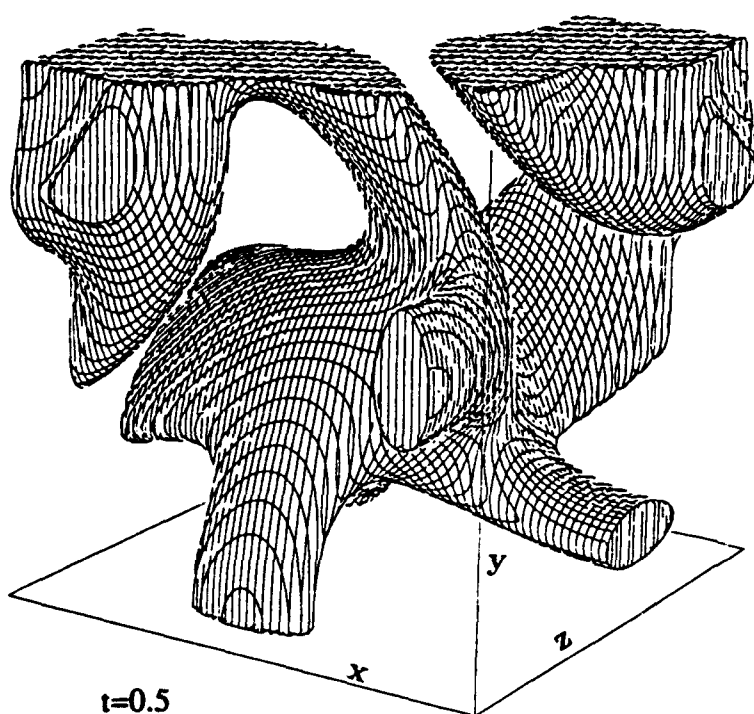




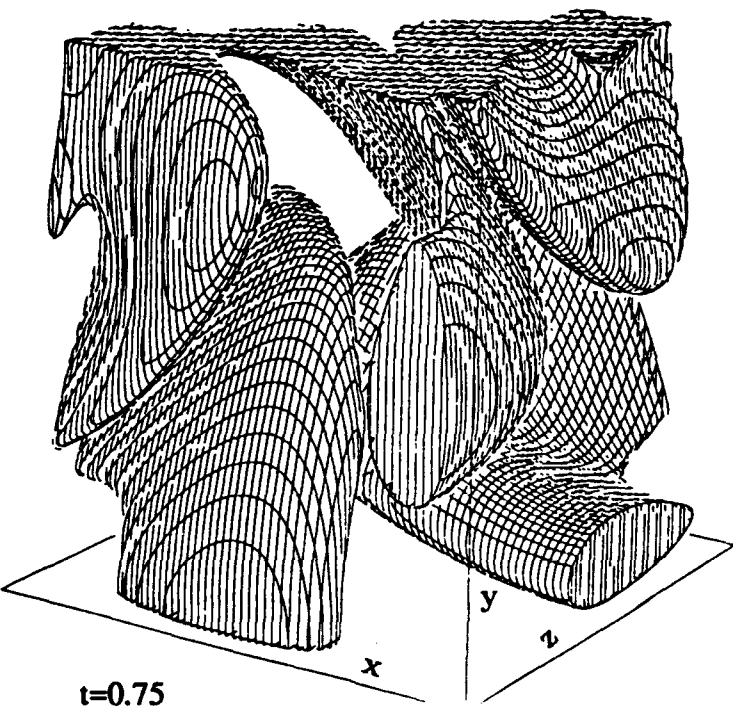
$t=0.0$



$t=0.2$

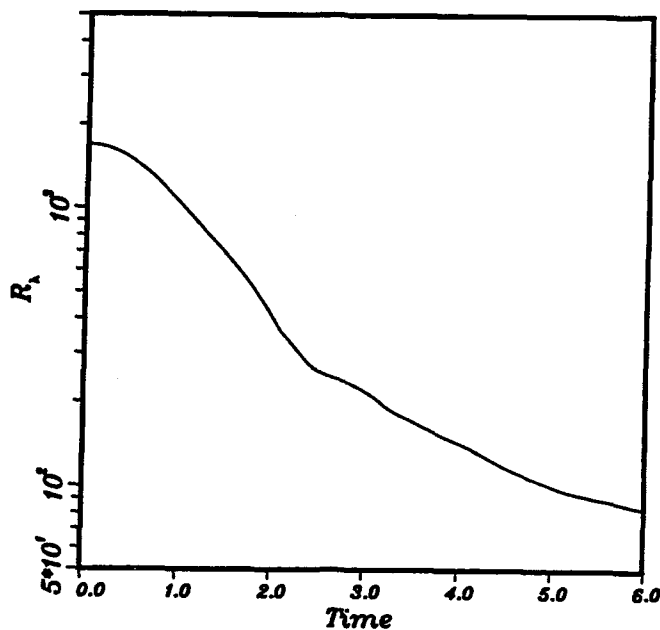
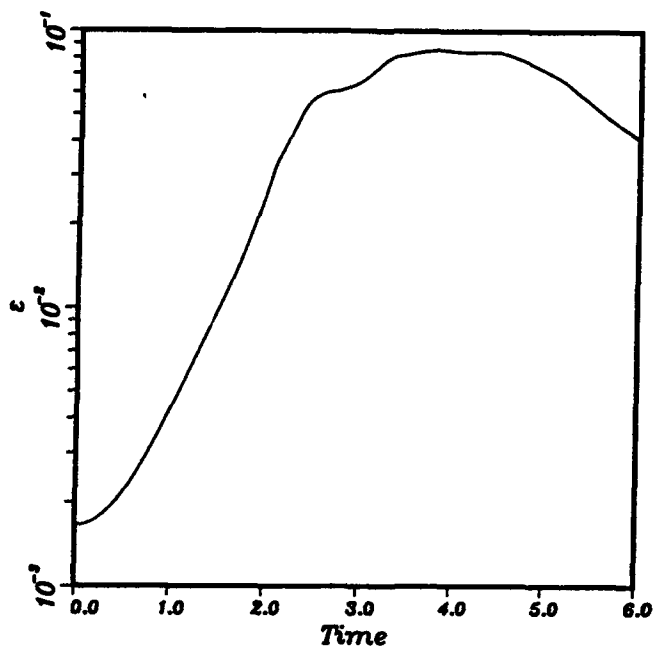
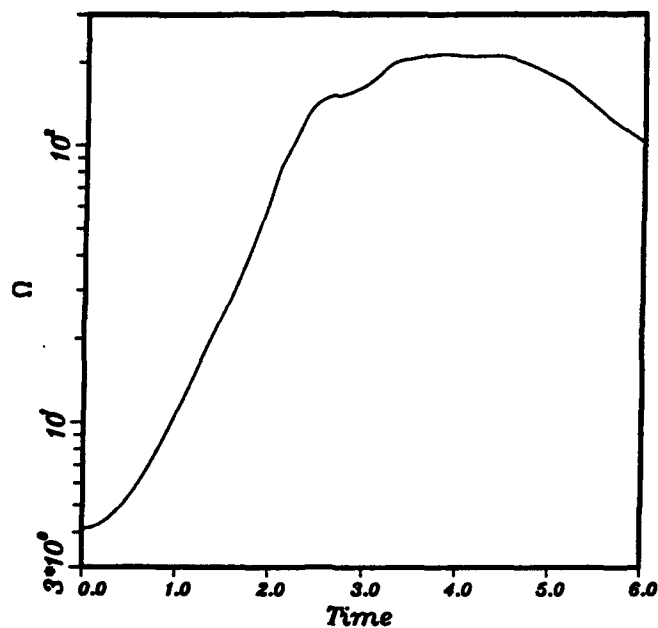
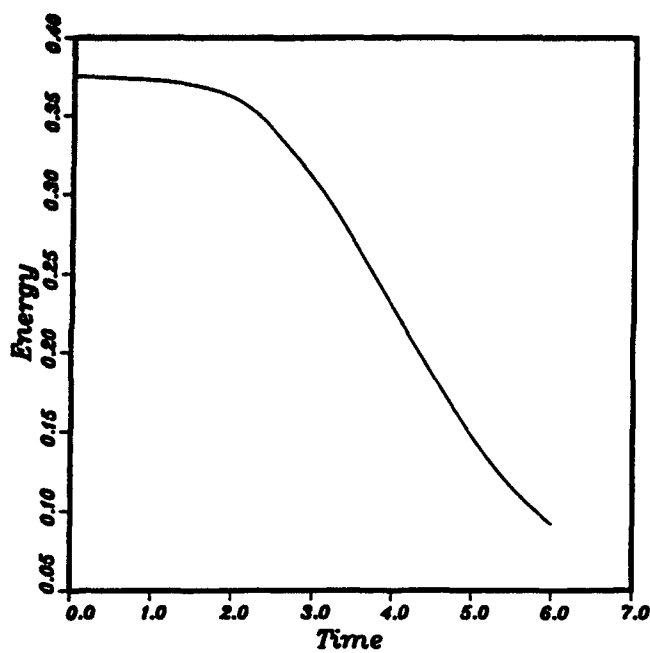


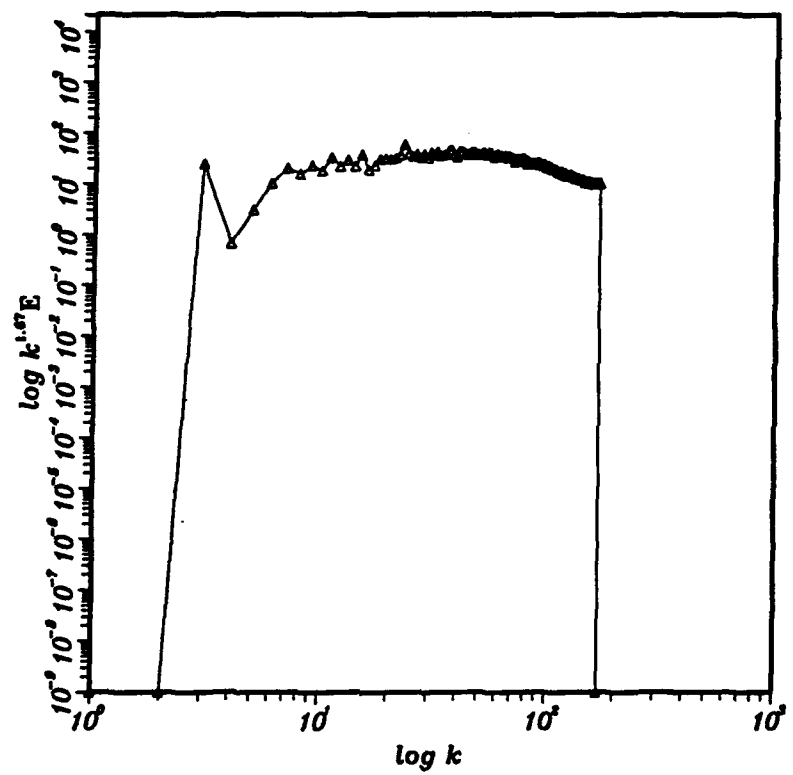
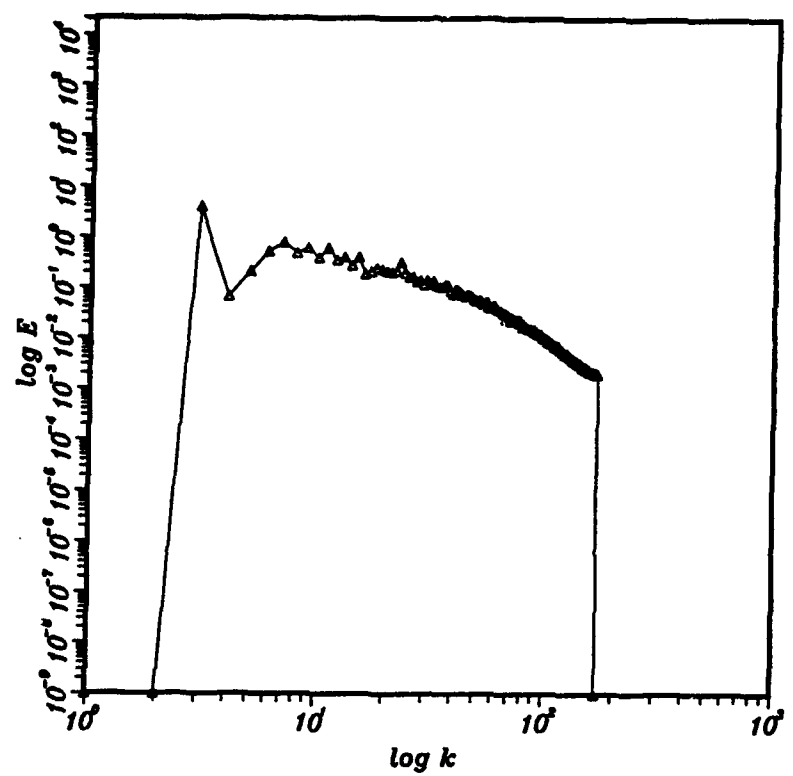
$t=0.5$



$t=0.75$

2

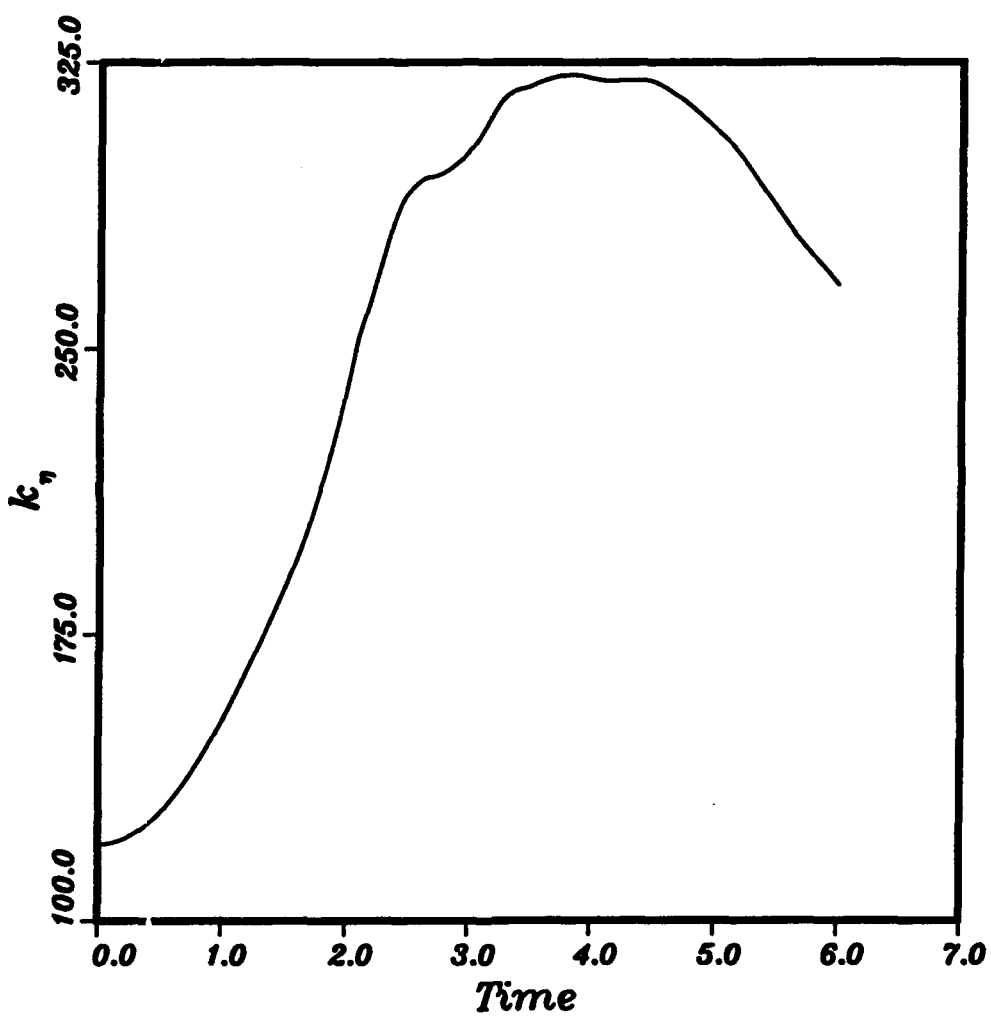


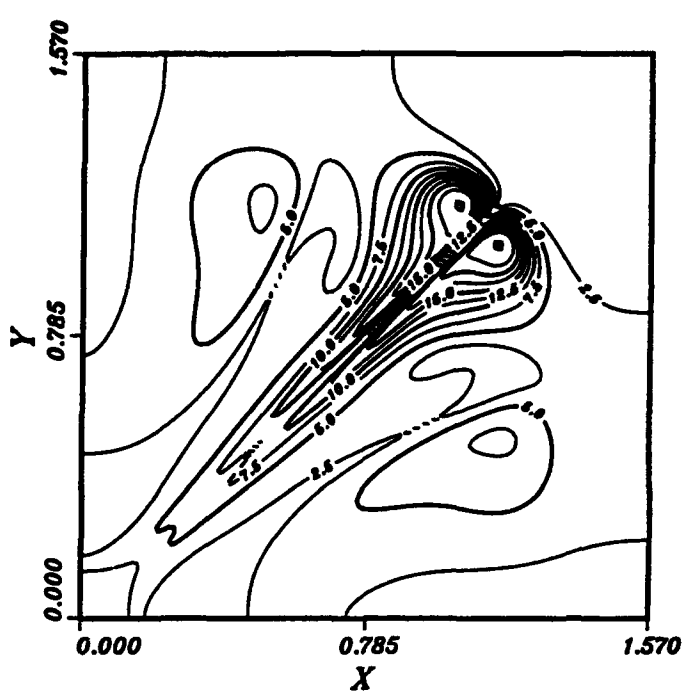
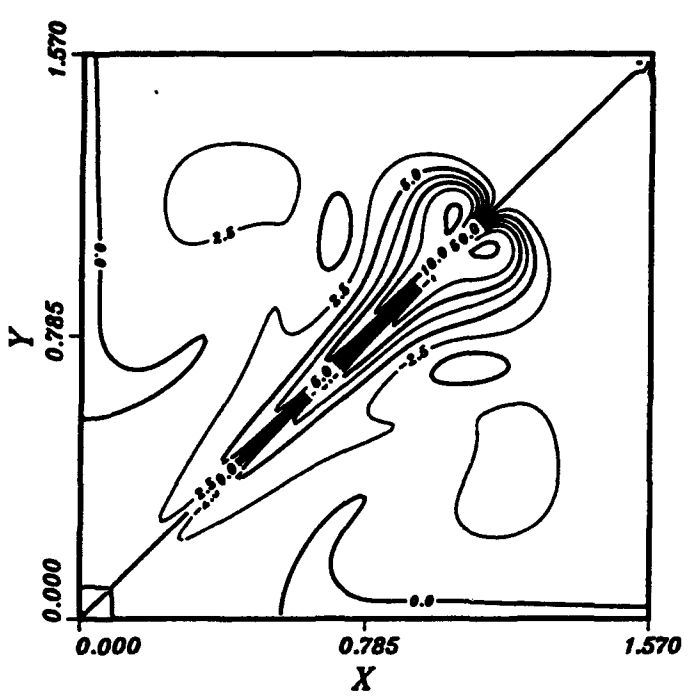
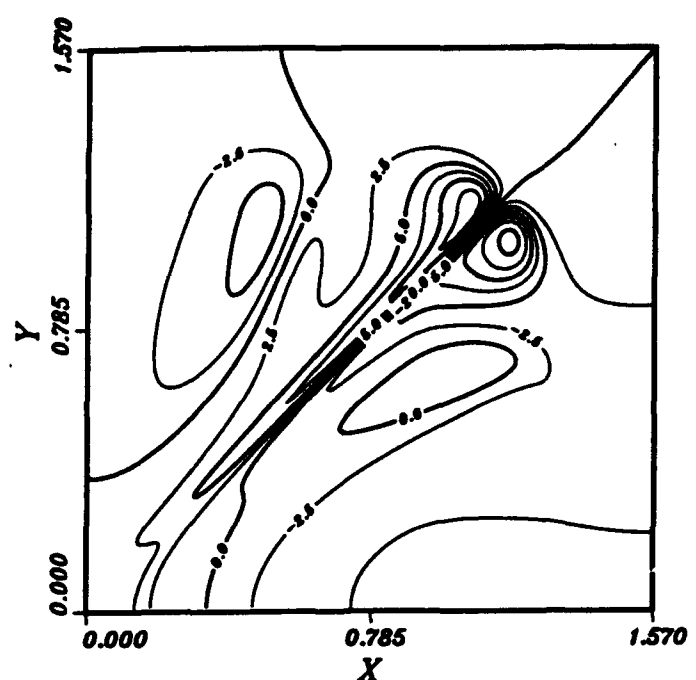
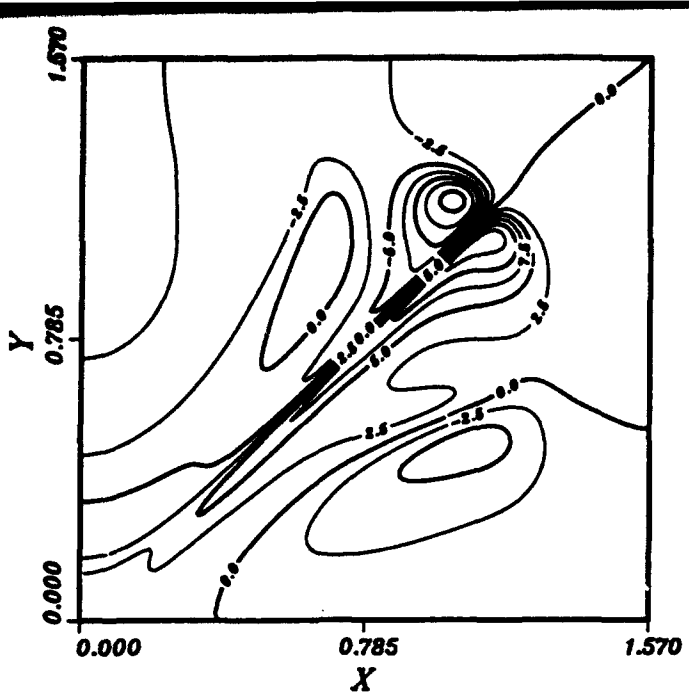


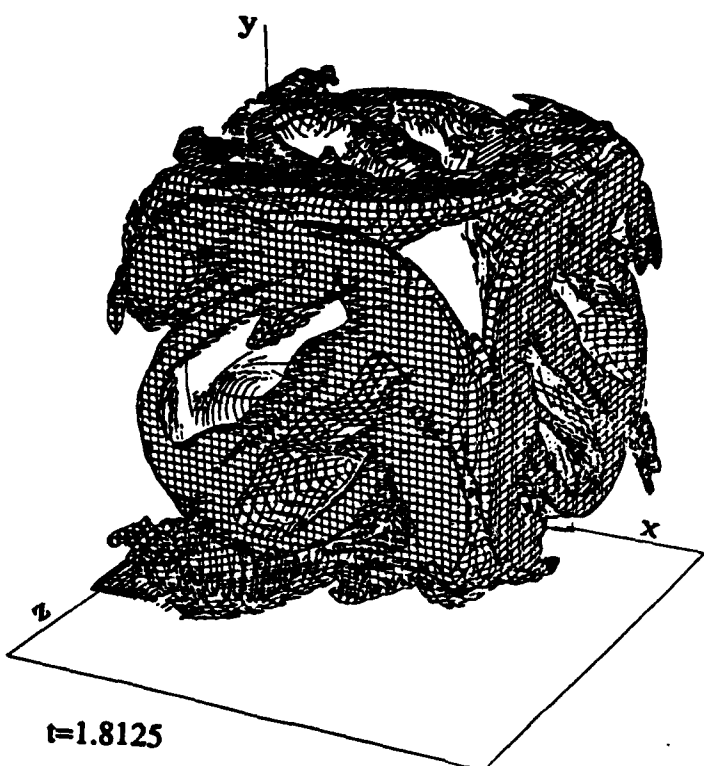
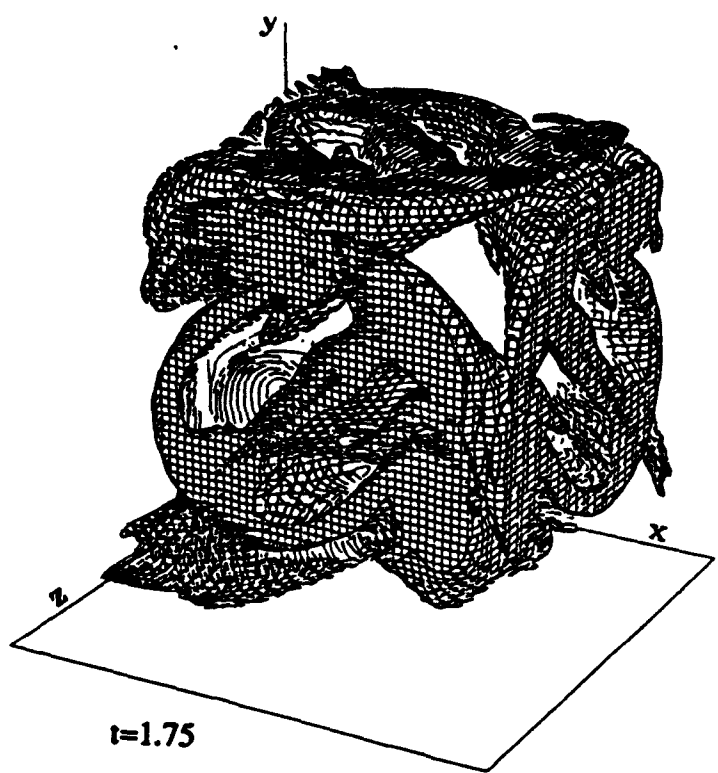
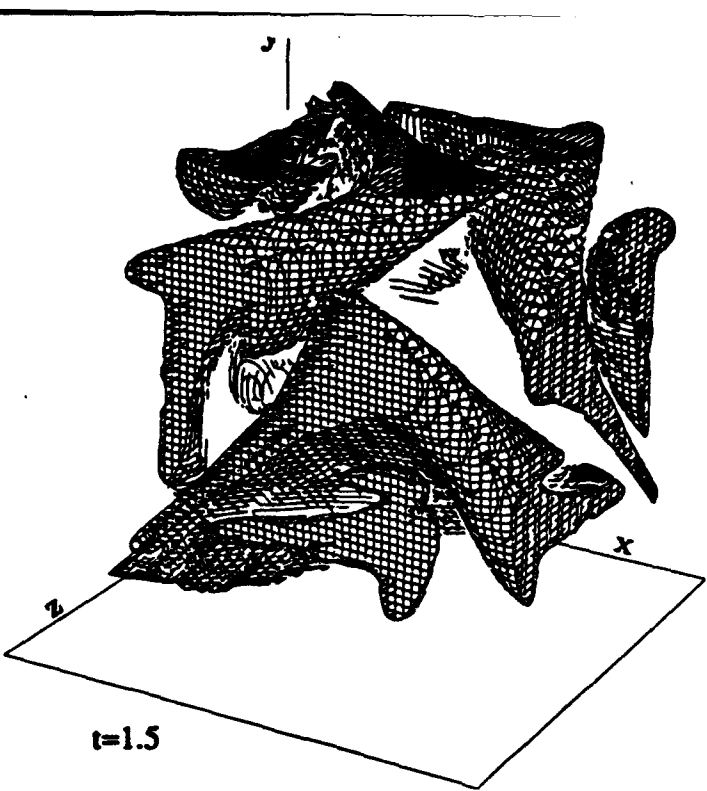
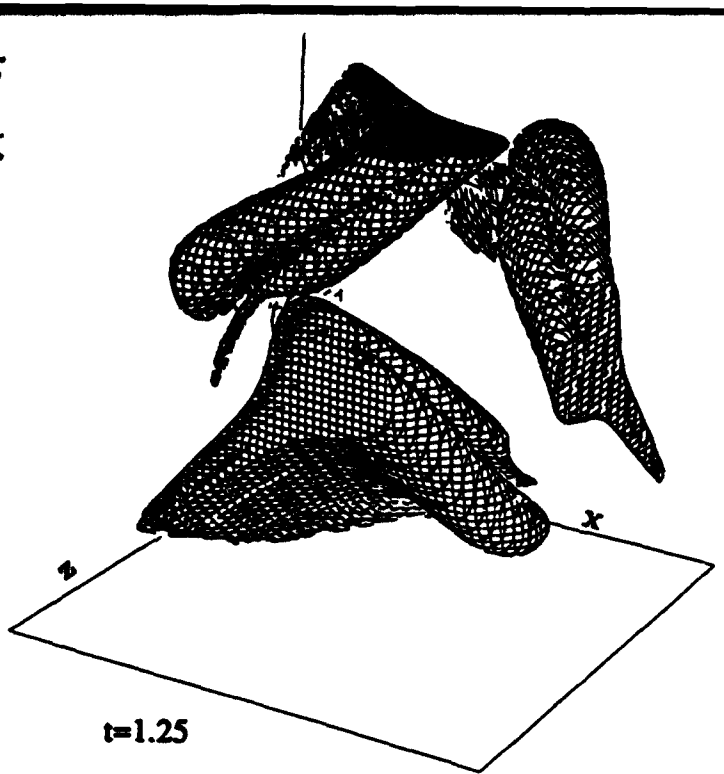
4a,b

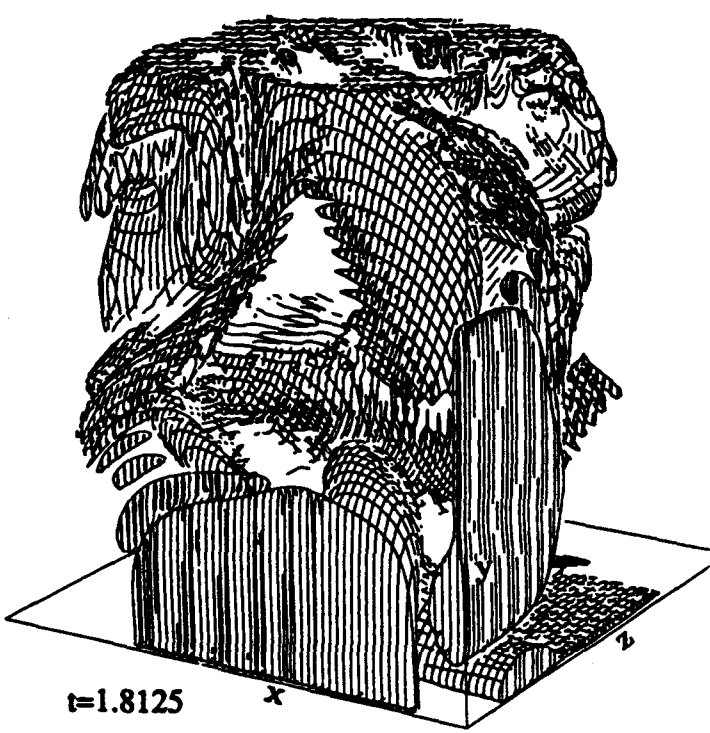
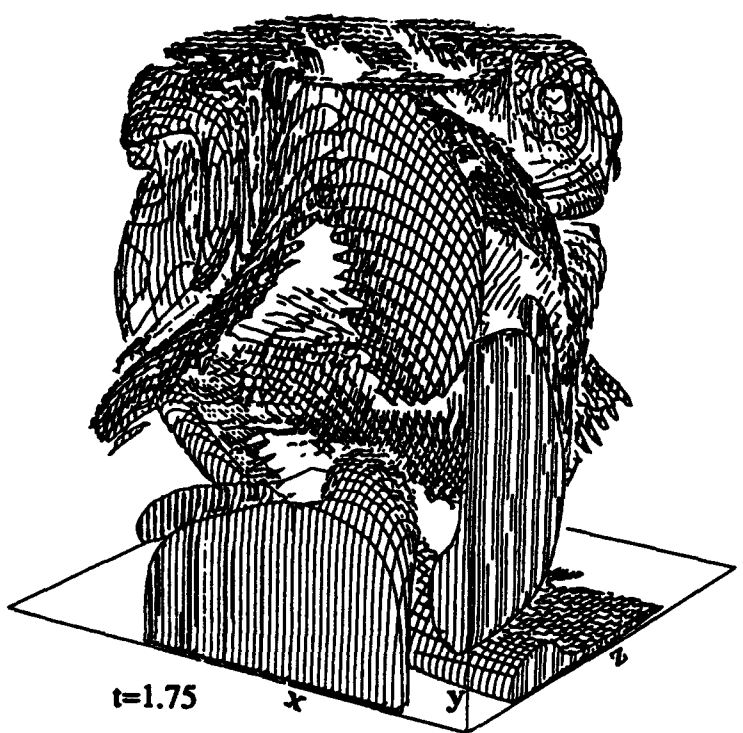
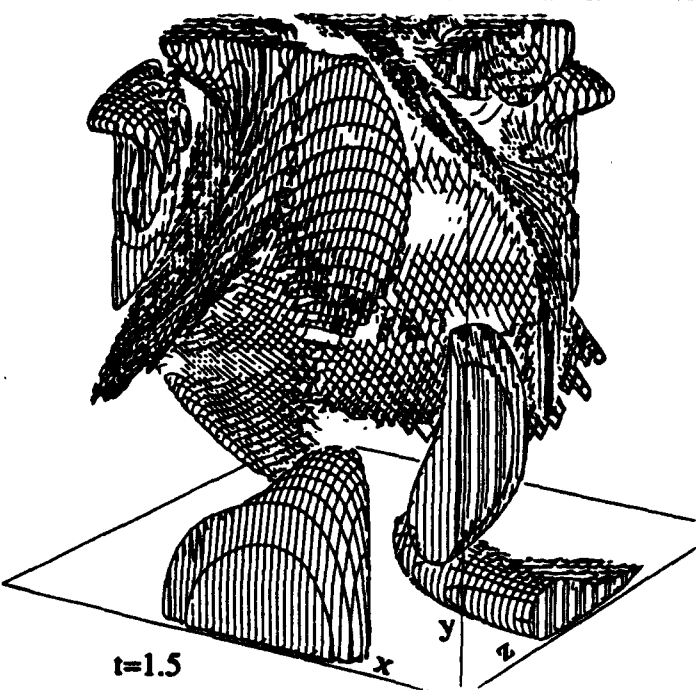
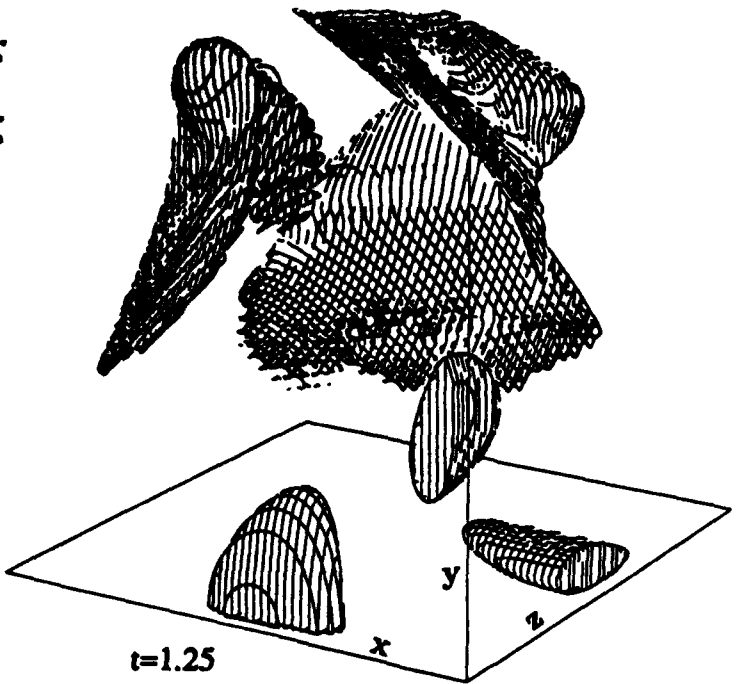
(2D) || Print || speck plt || Specdrak5/3 t=2.6.

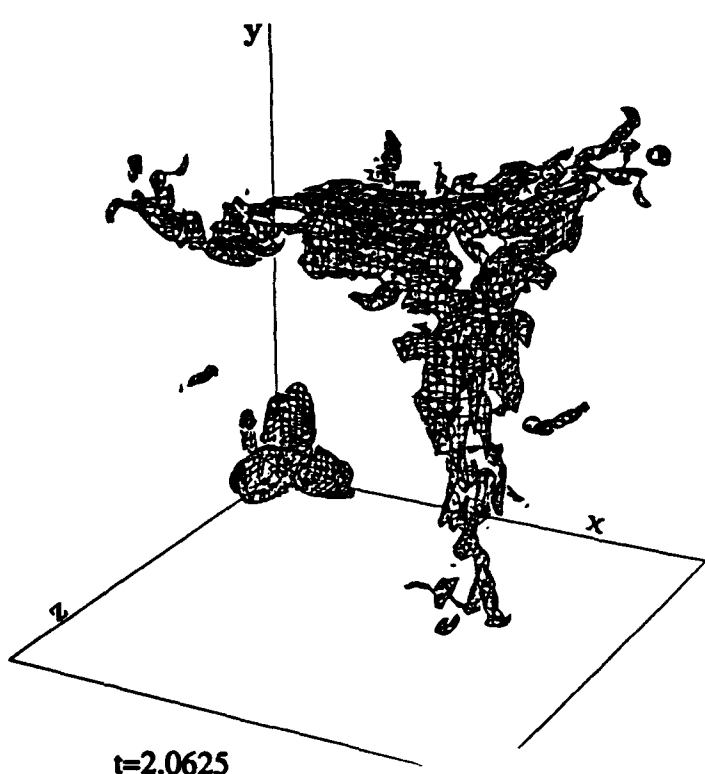
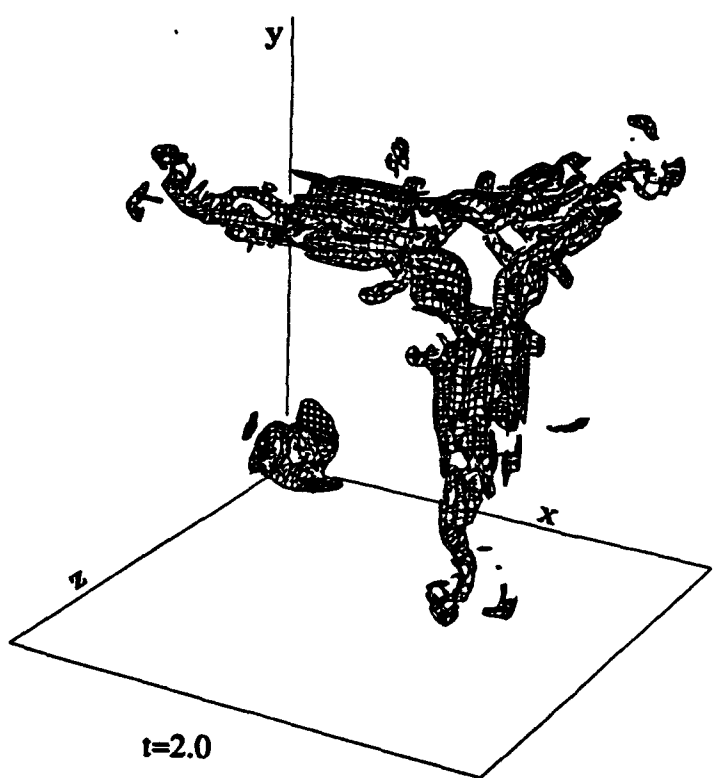
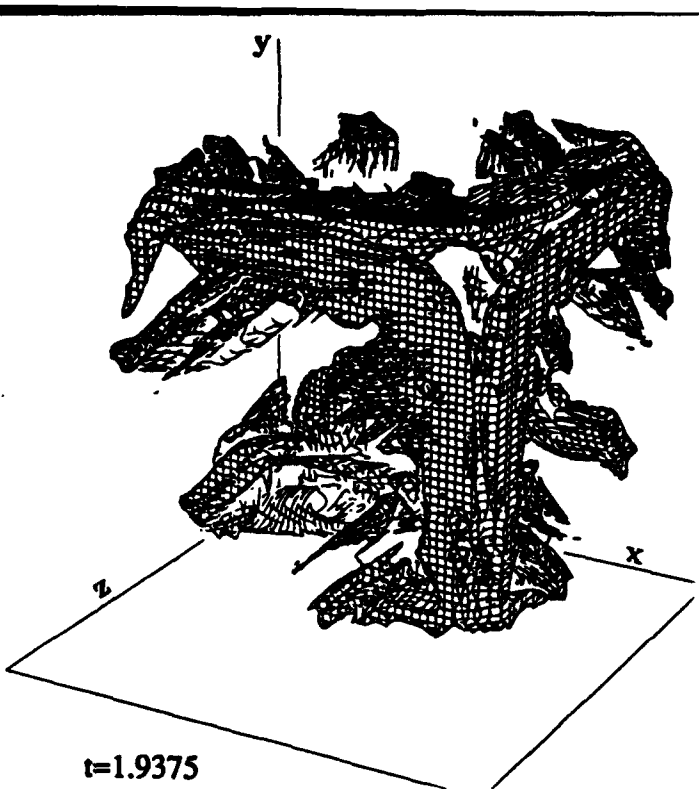
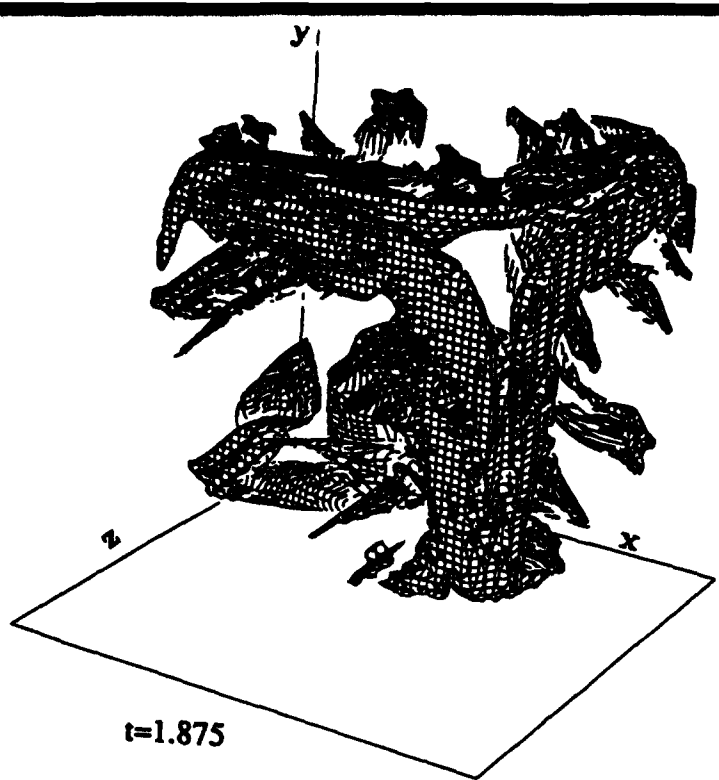


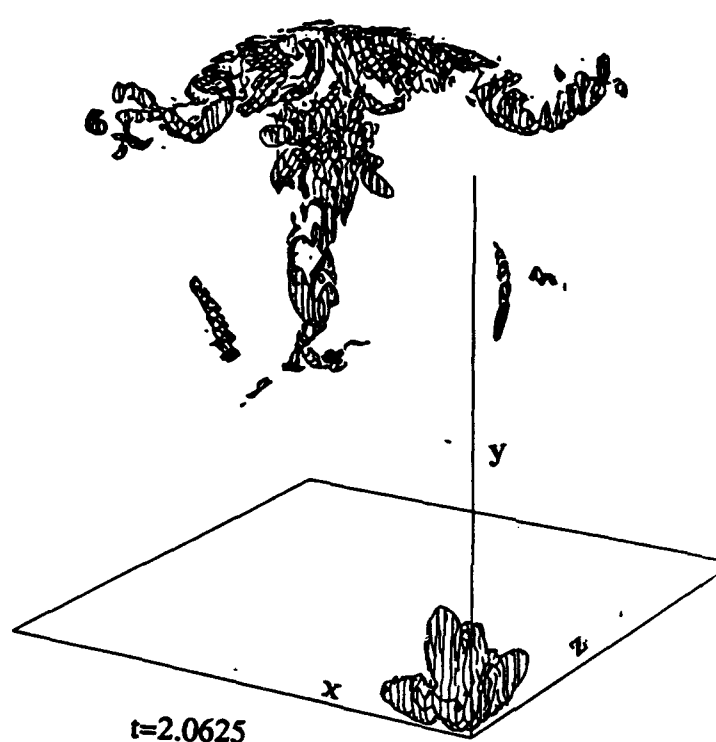
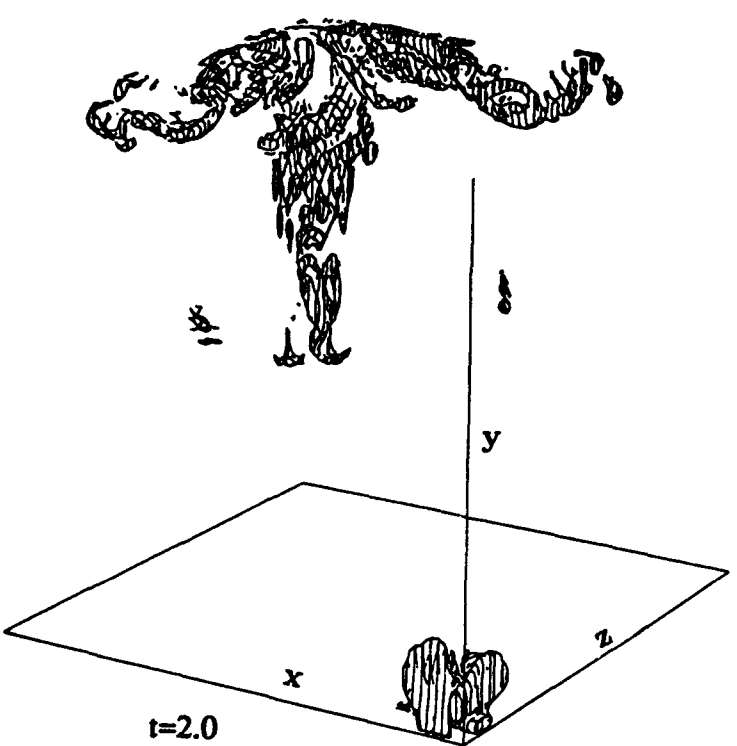
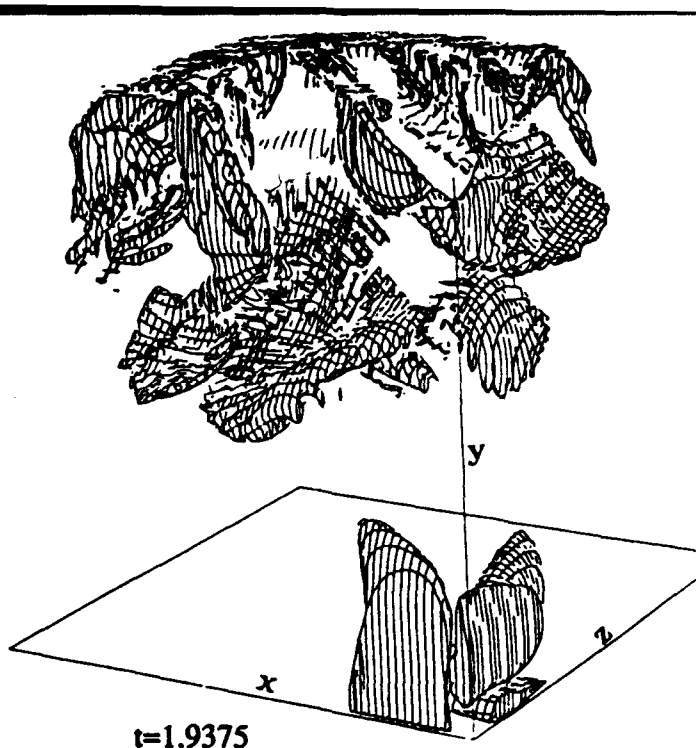
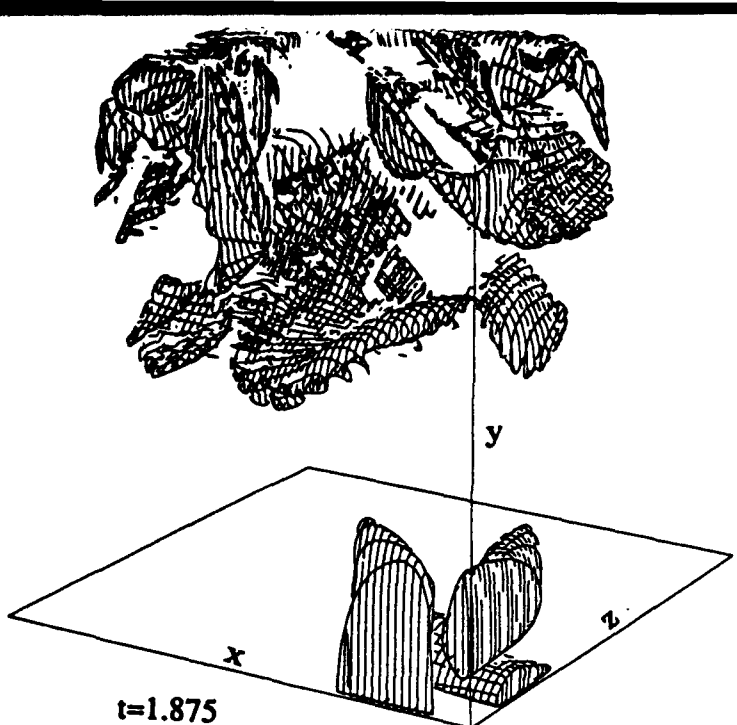


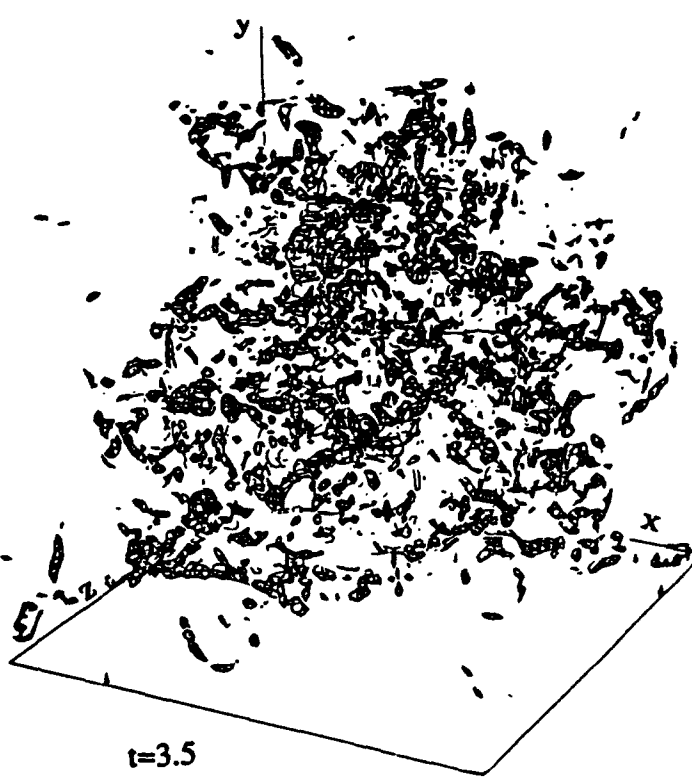
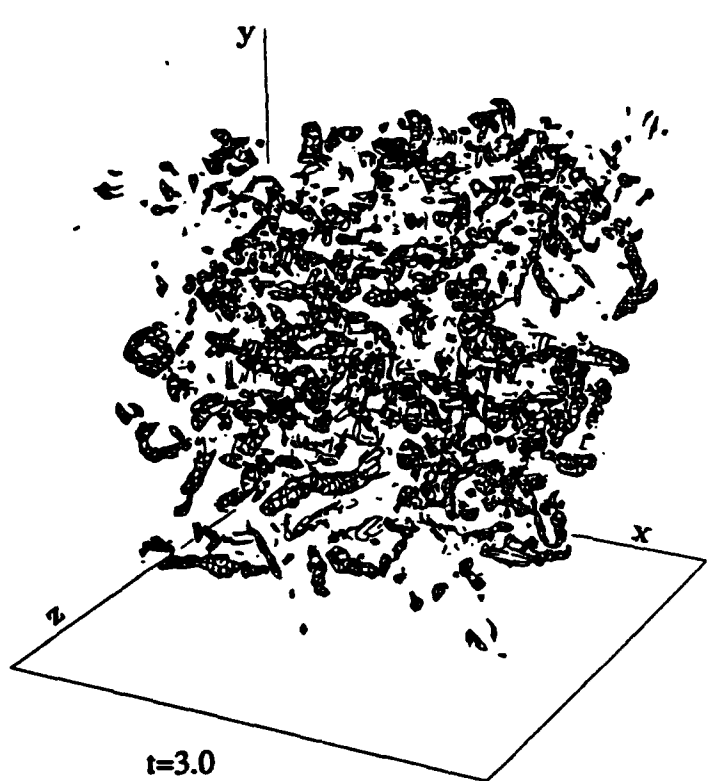
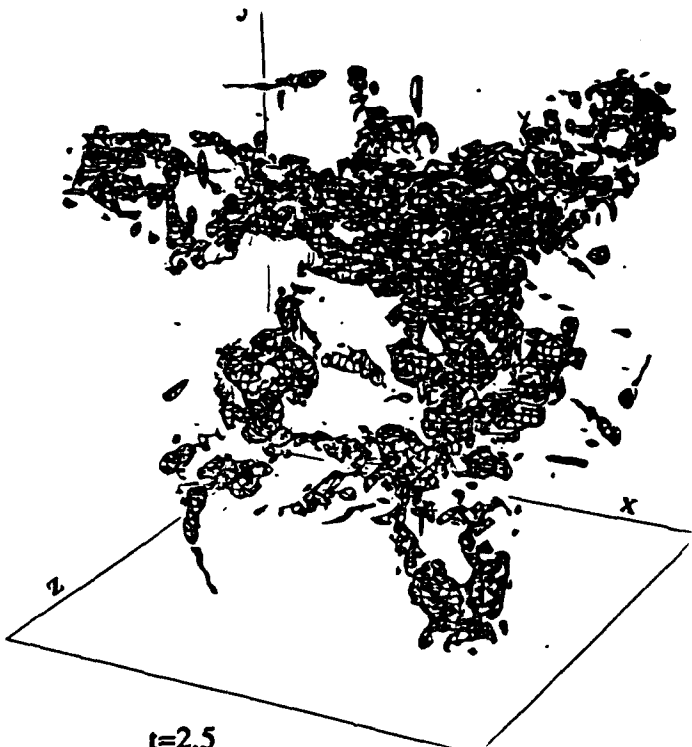
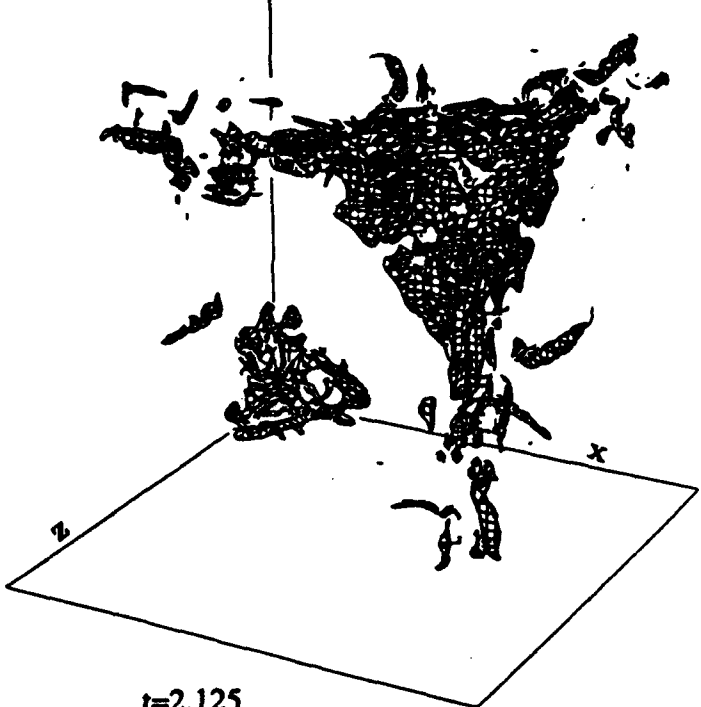


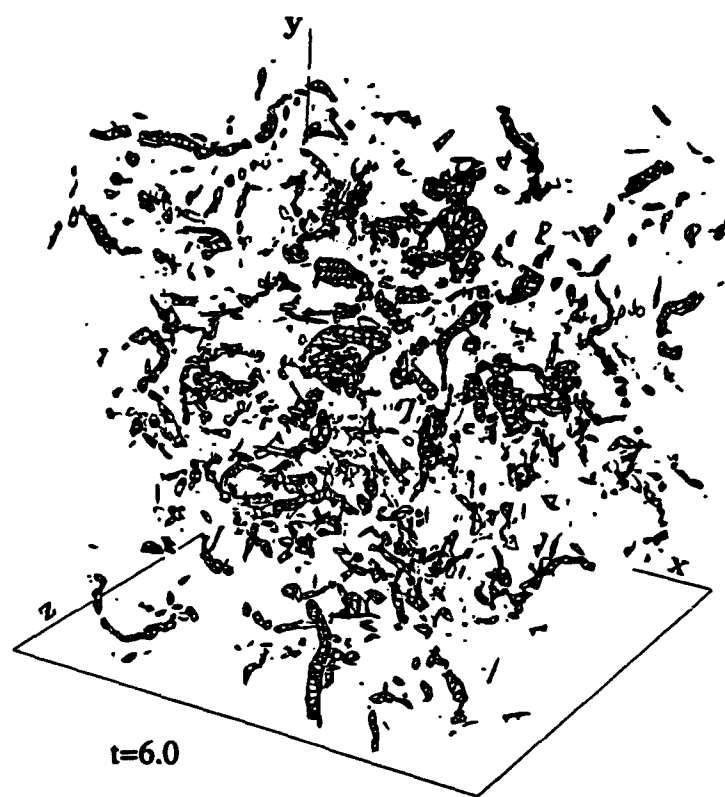
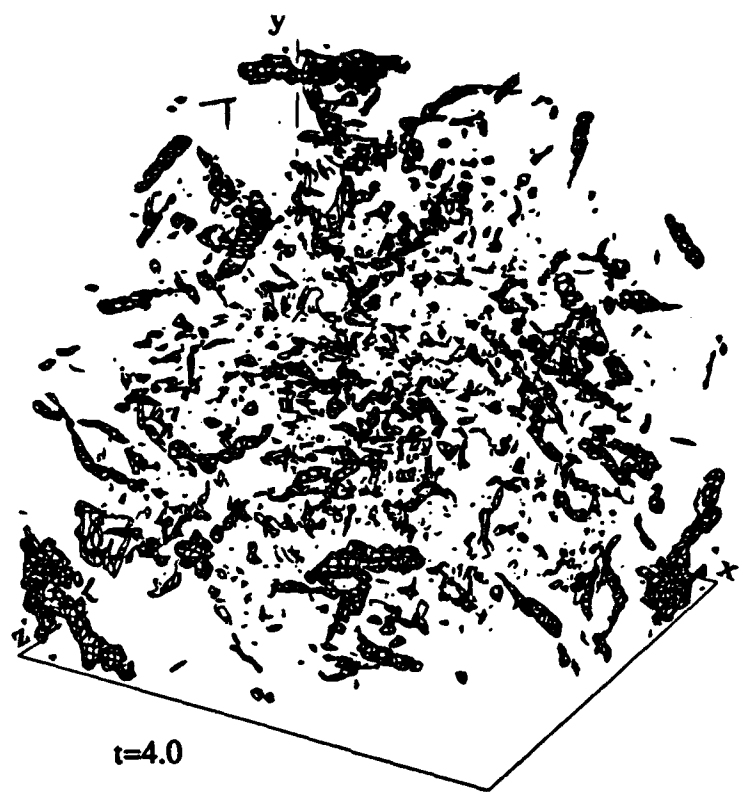


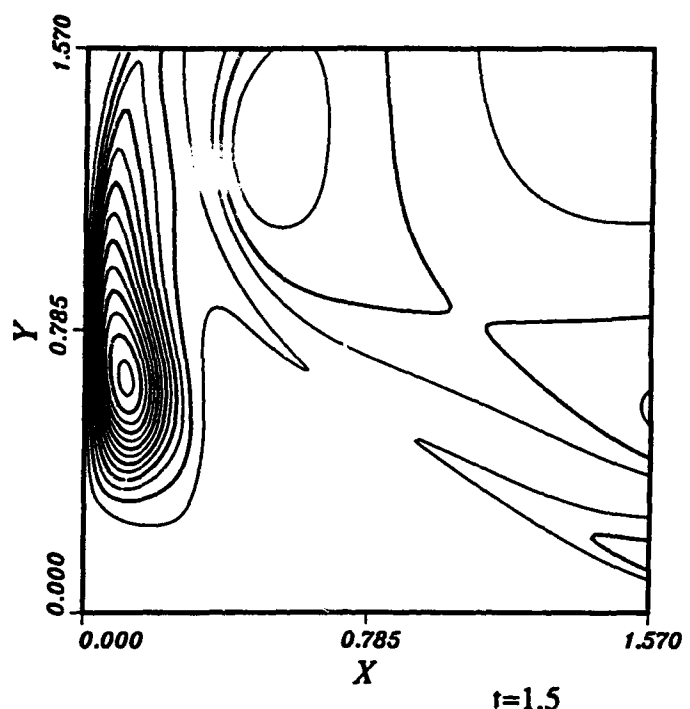
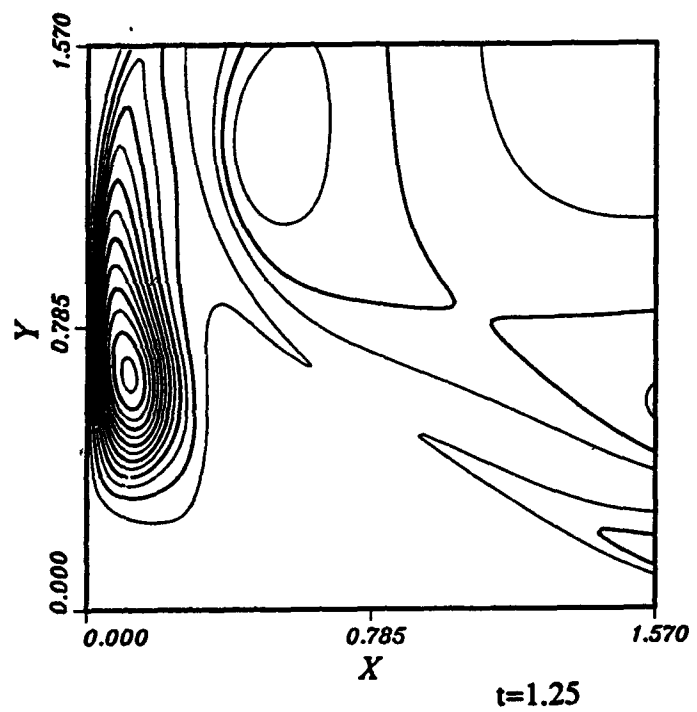
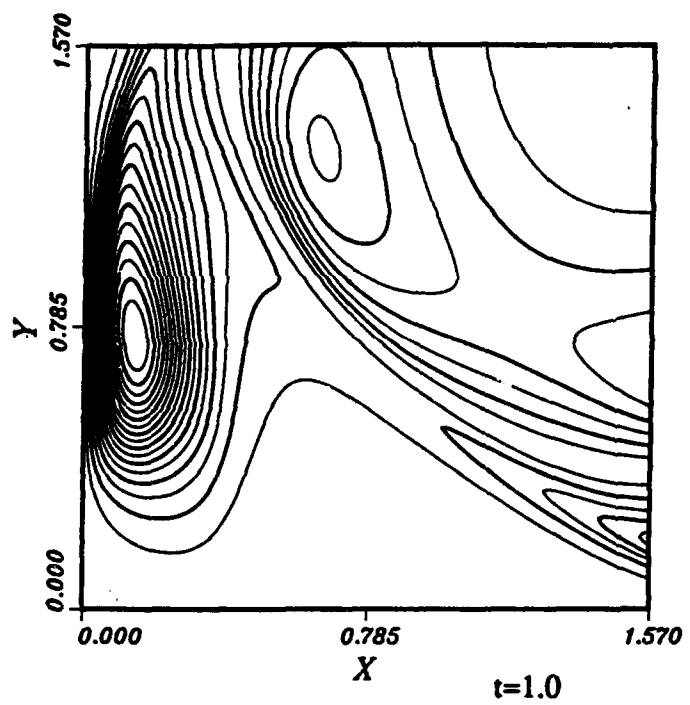
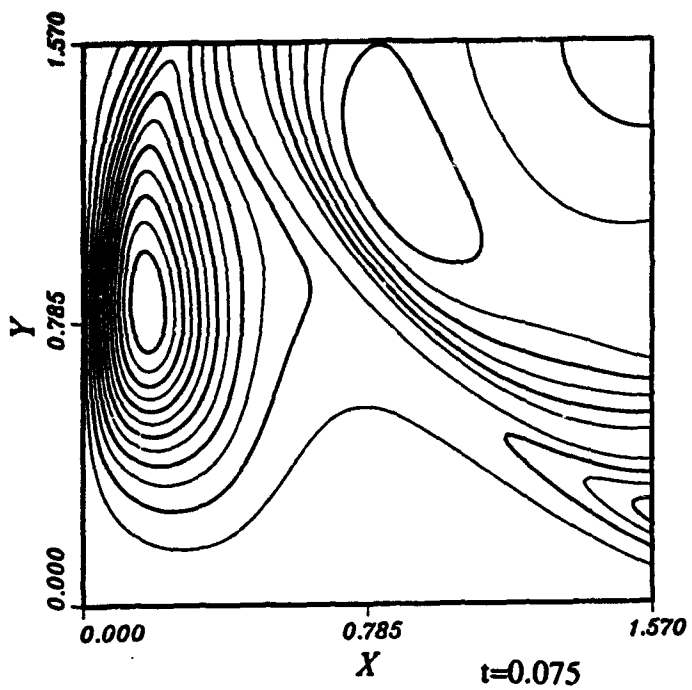


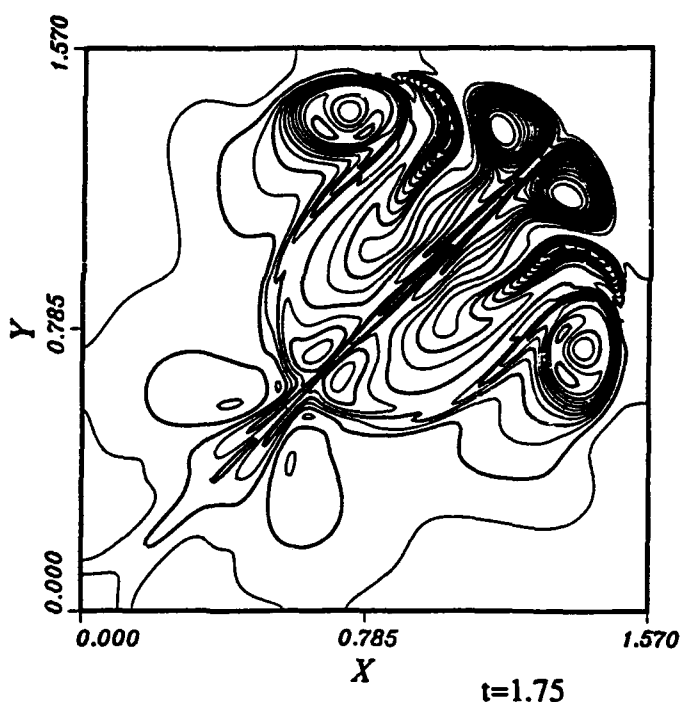
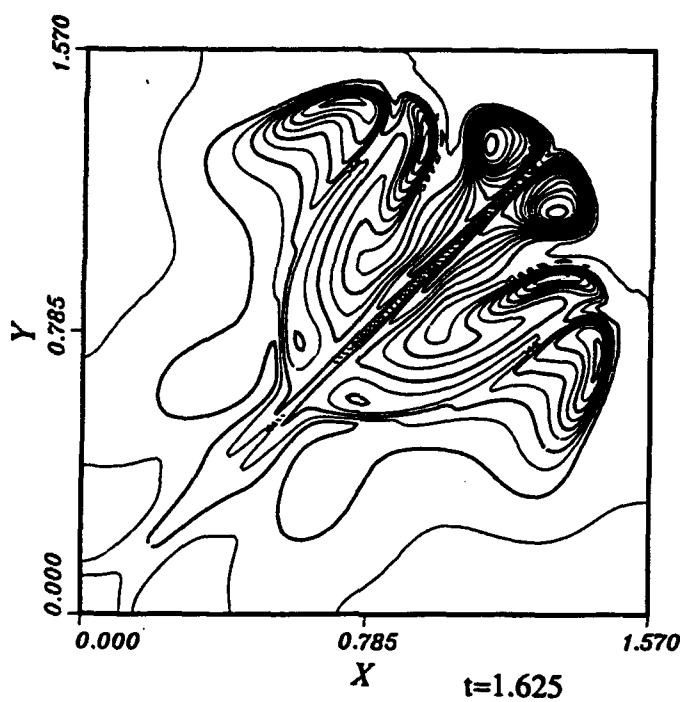
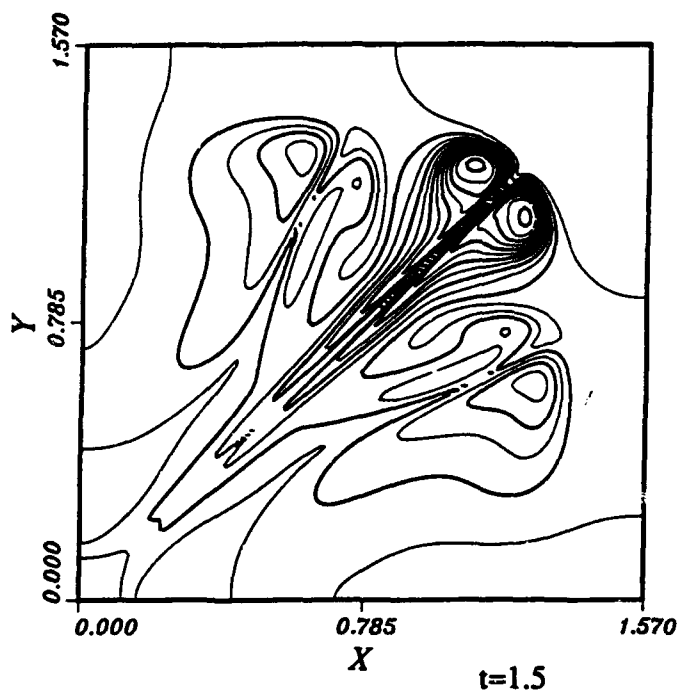
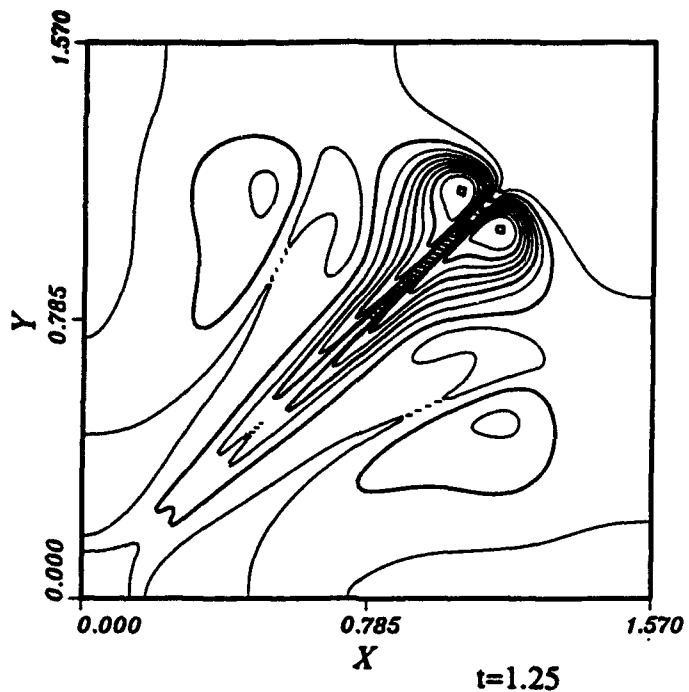


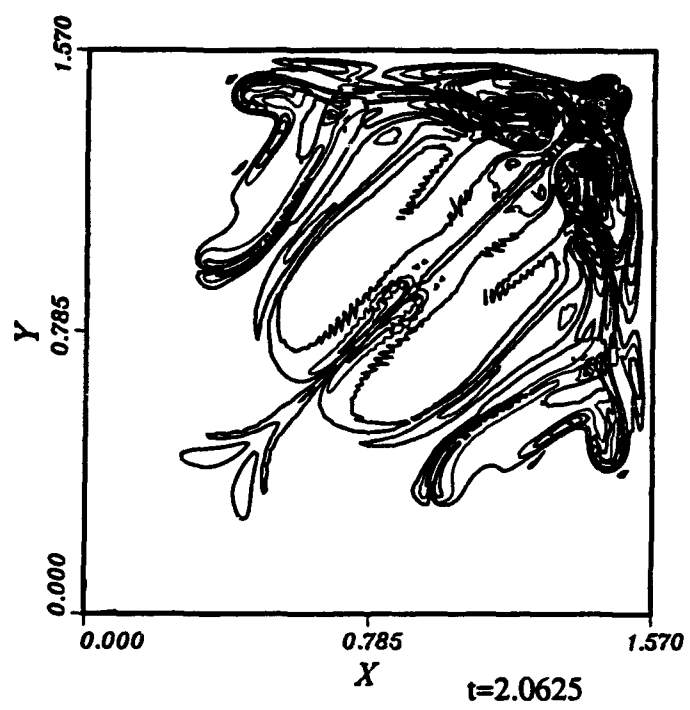
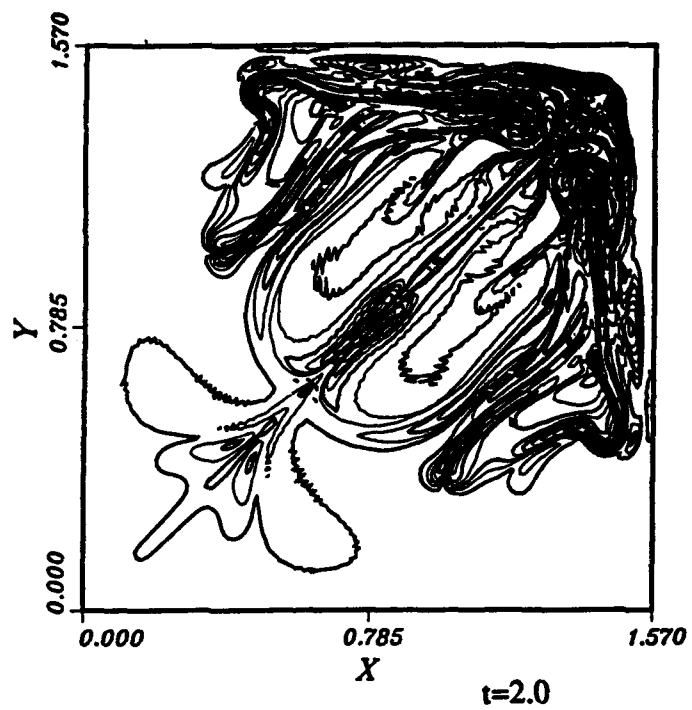
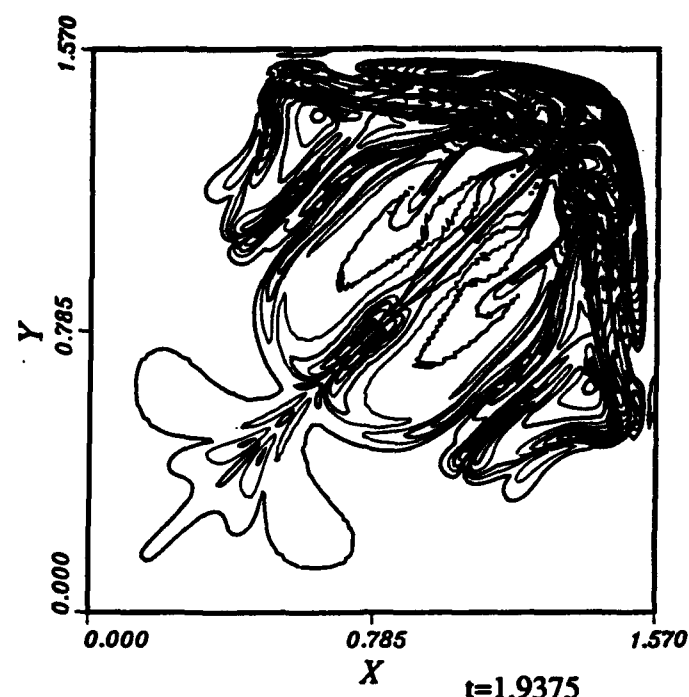
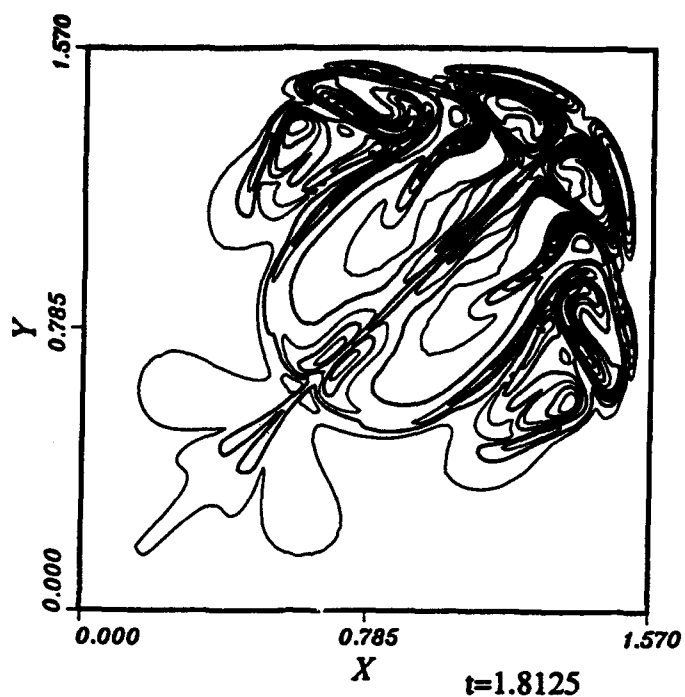


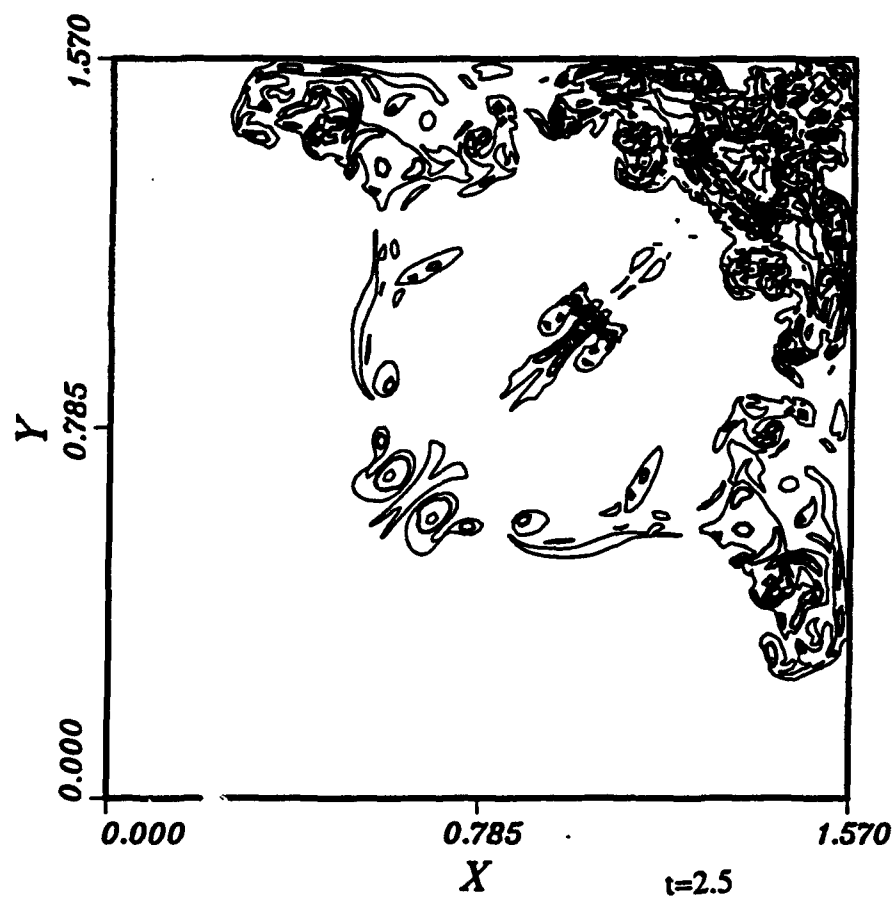
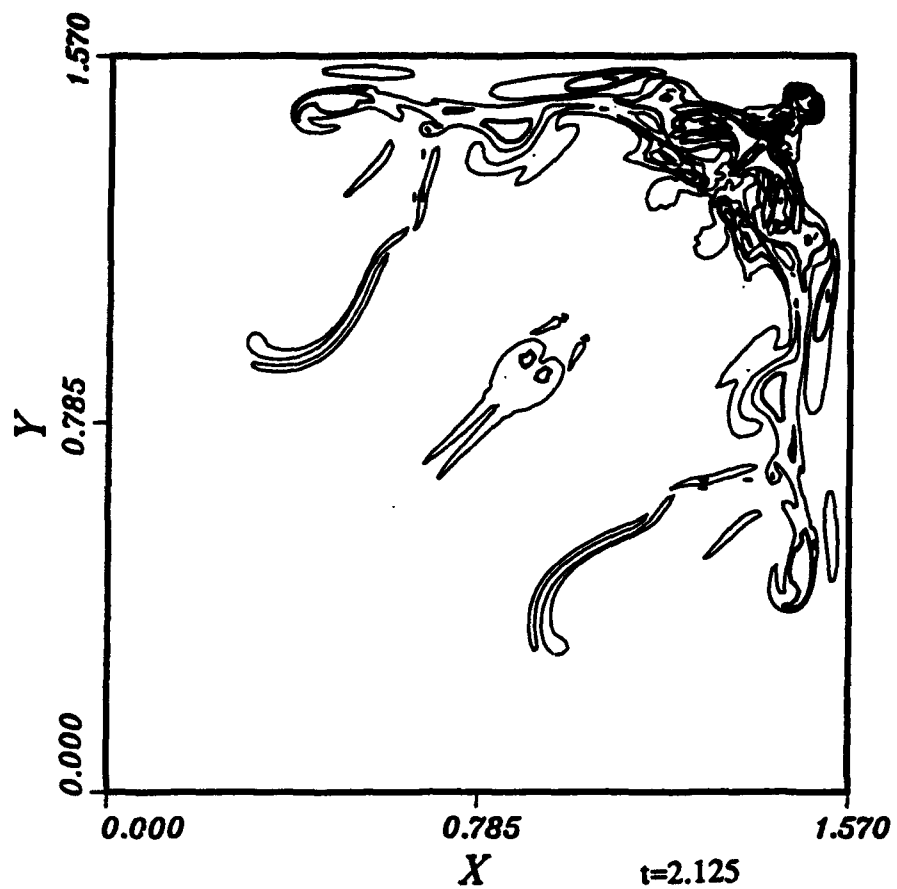


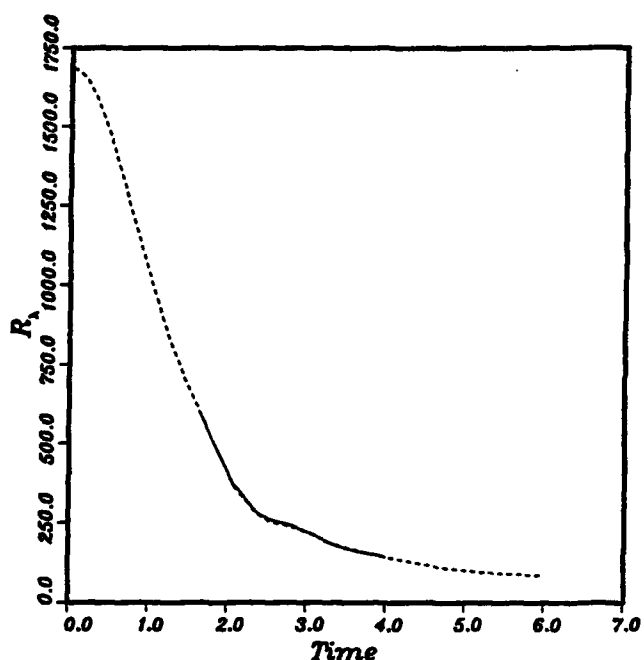
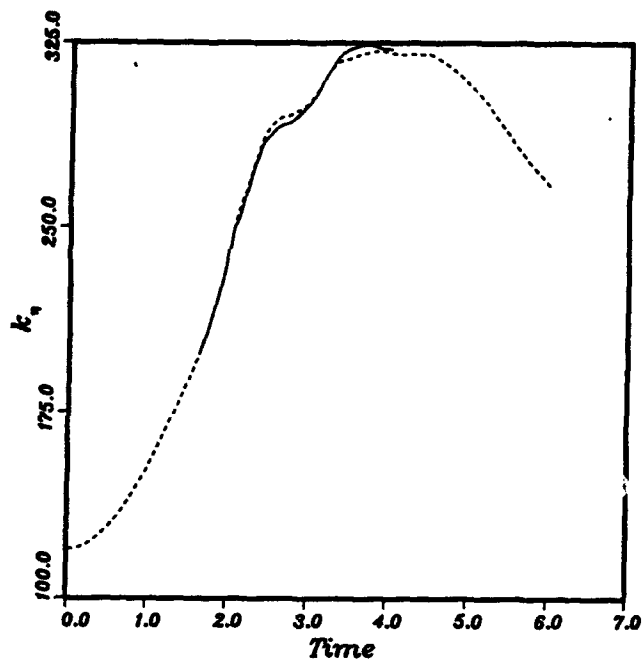
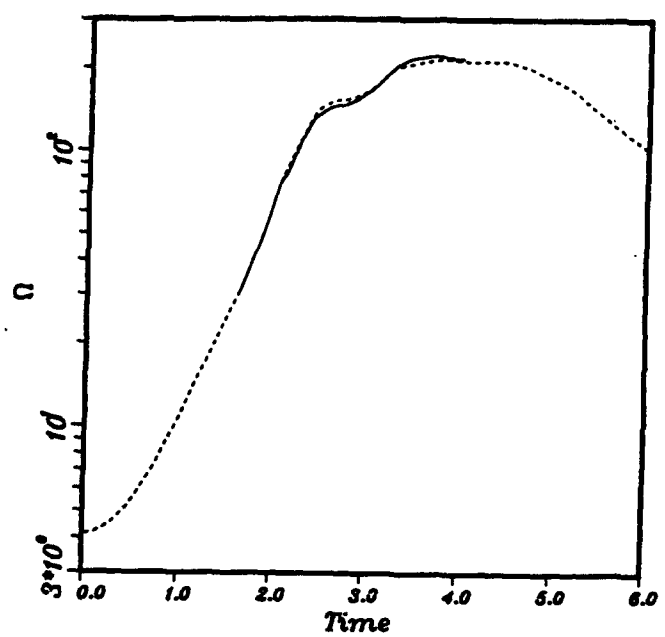
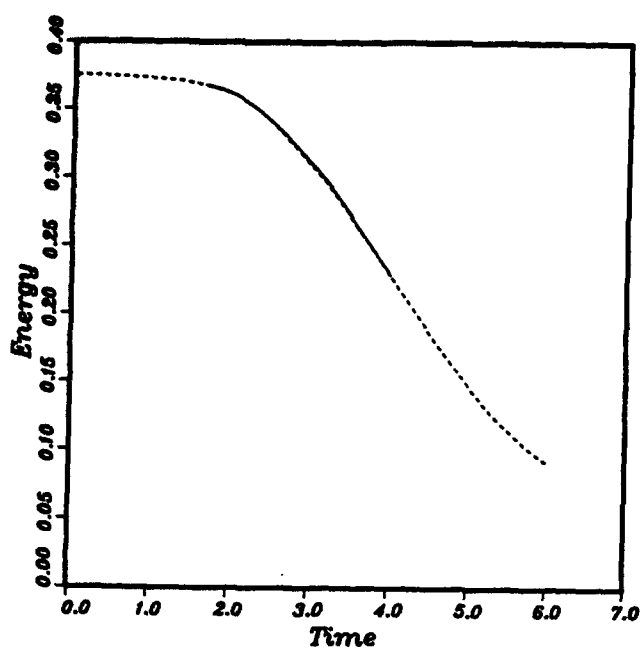


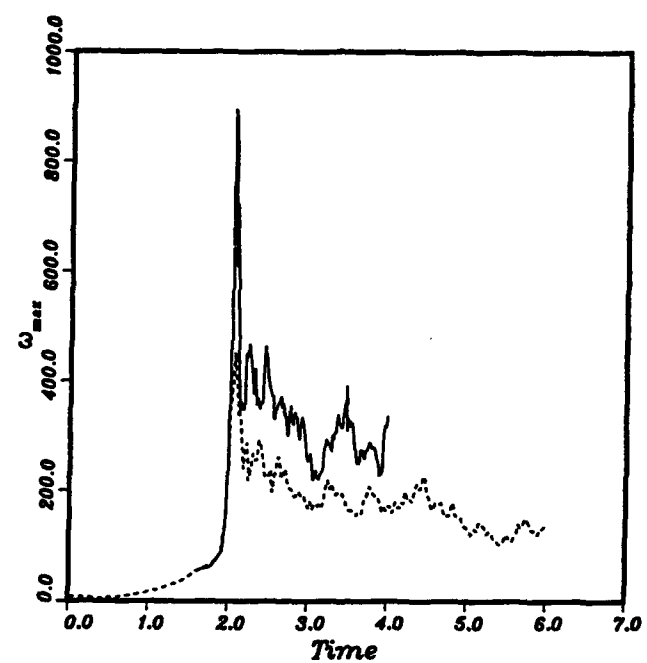
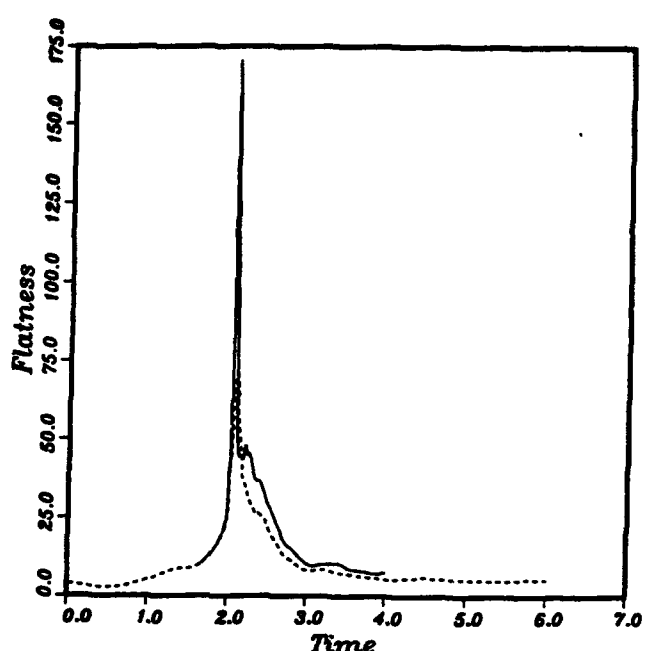
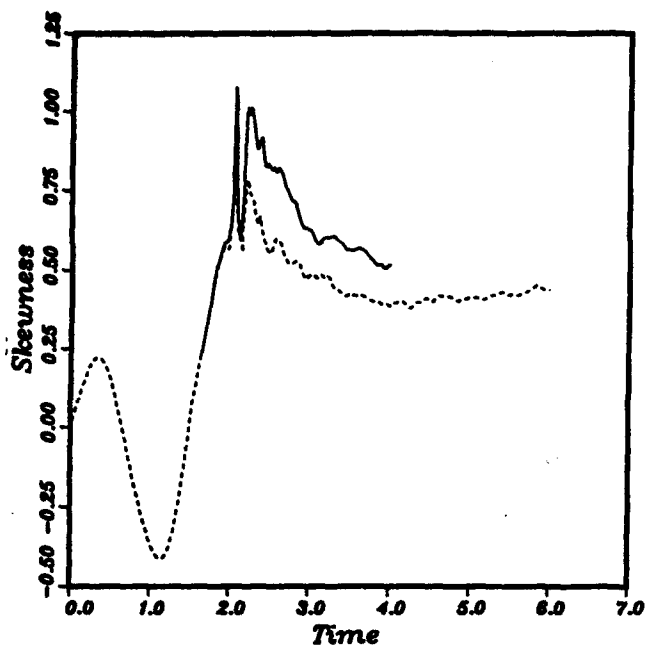


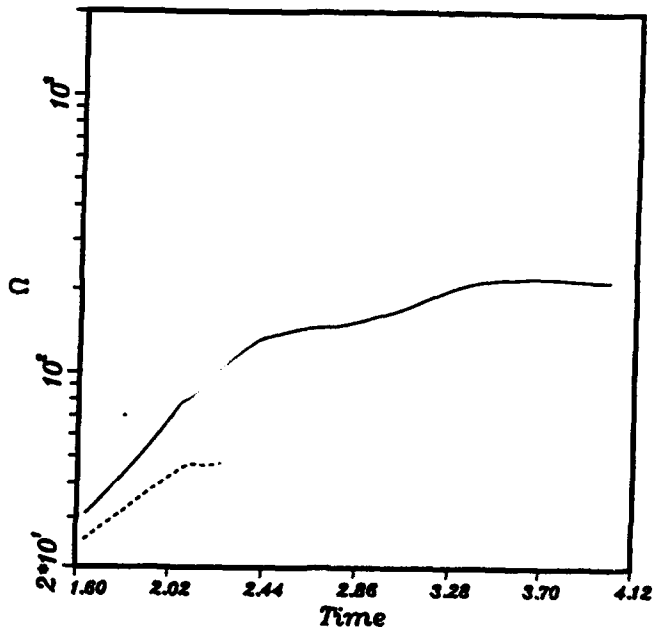
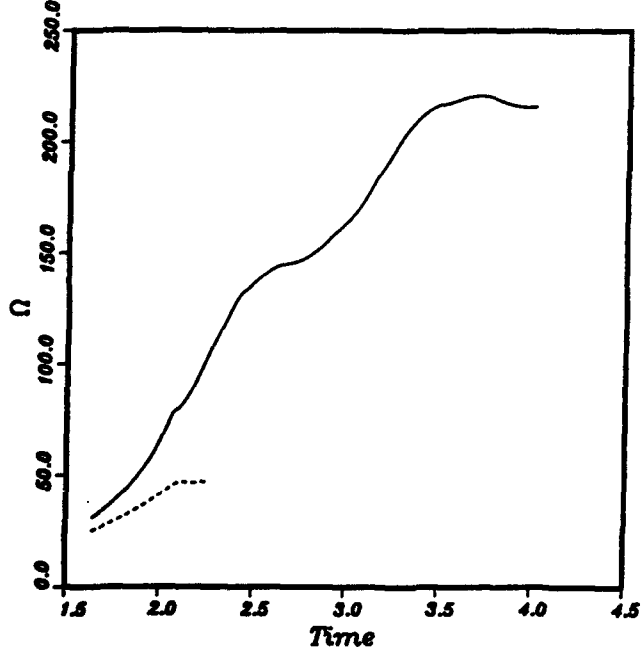
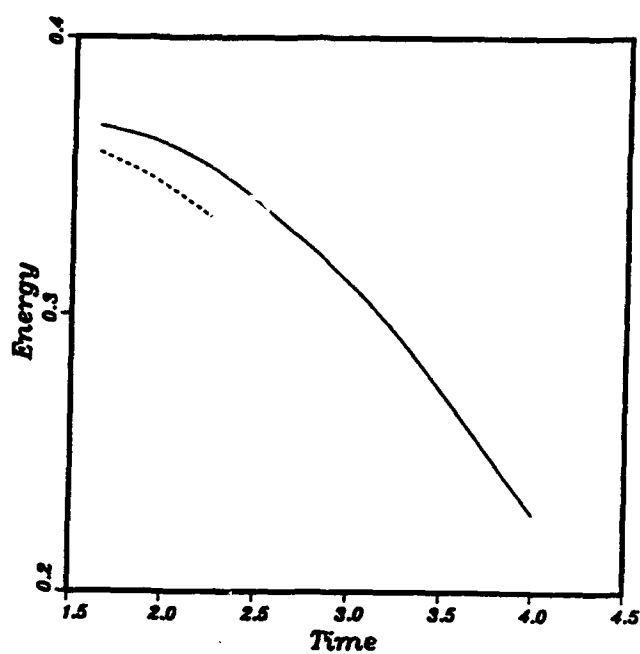
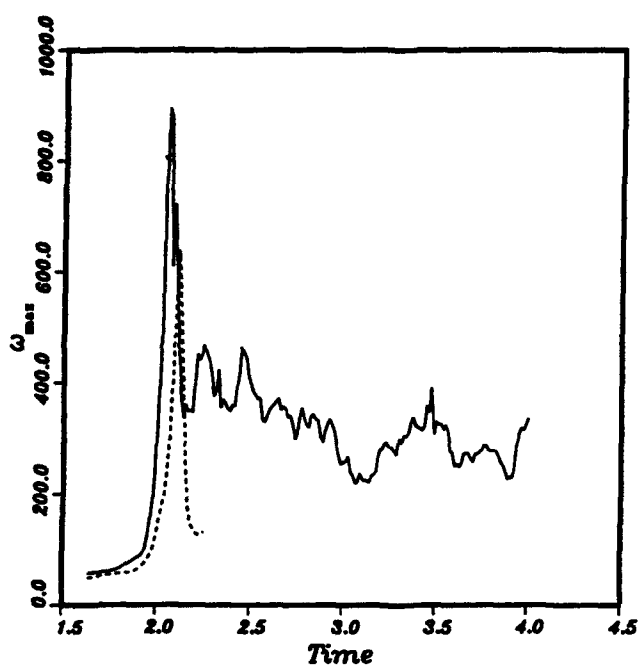
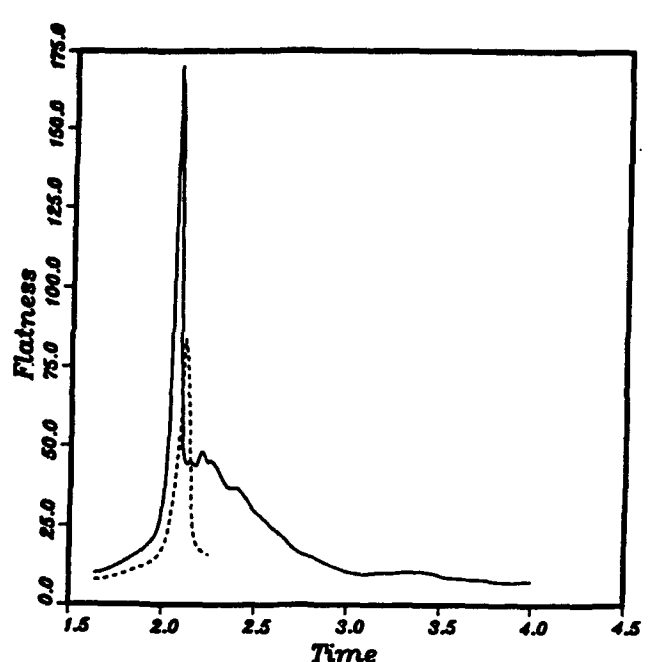
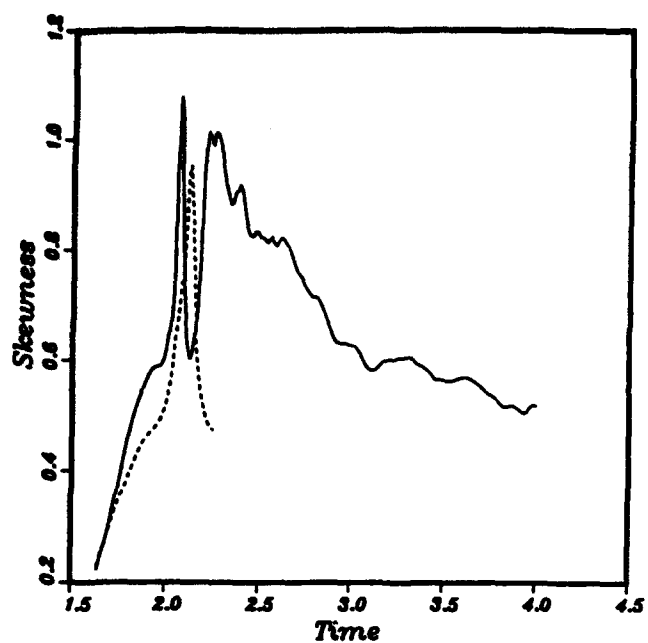


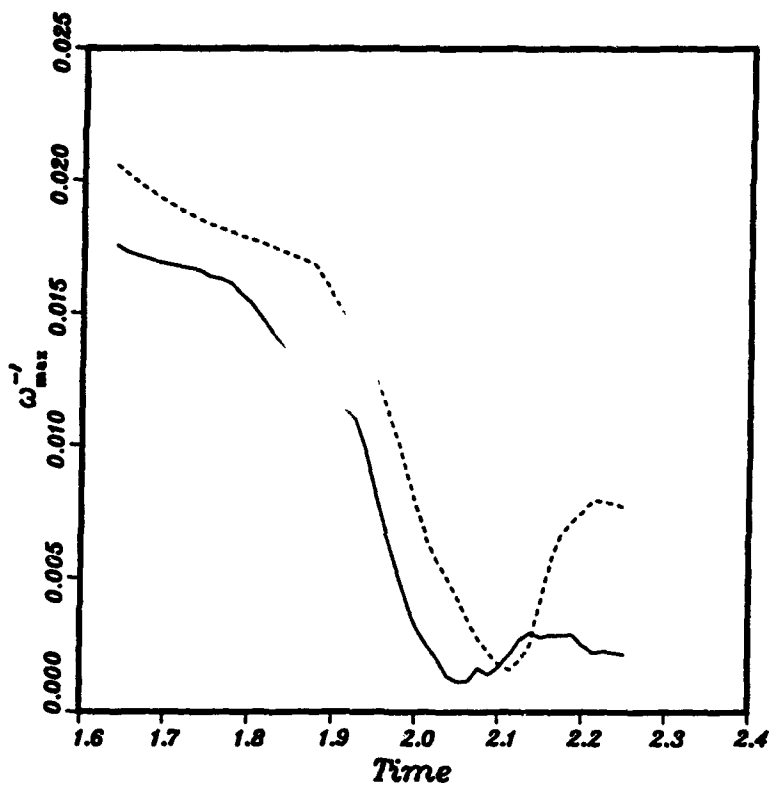
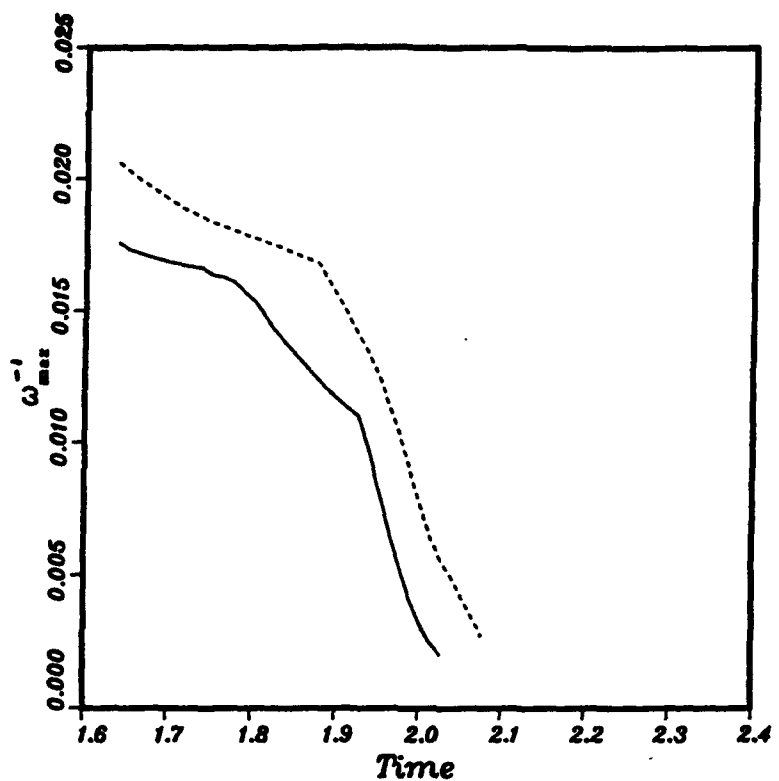




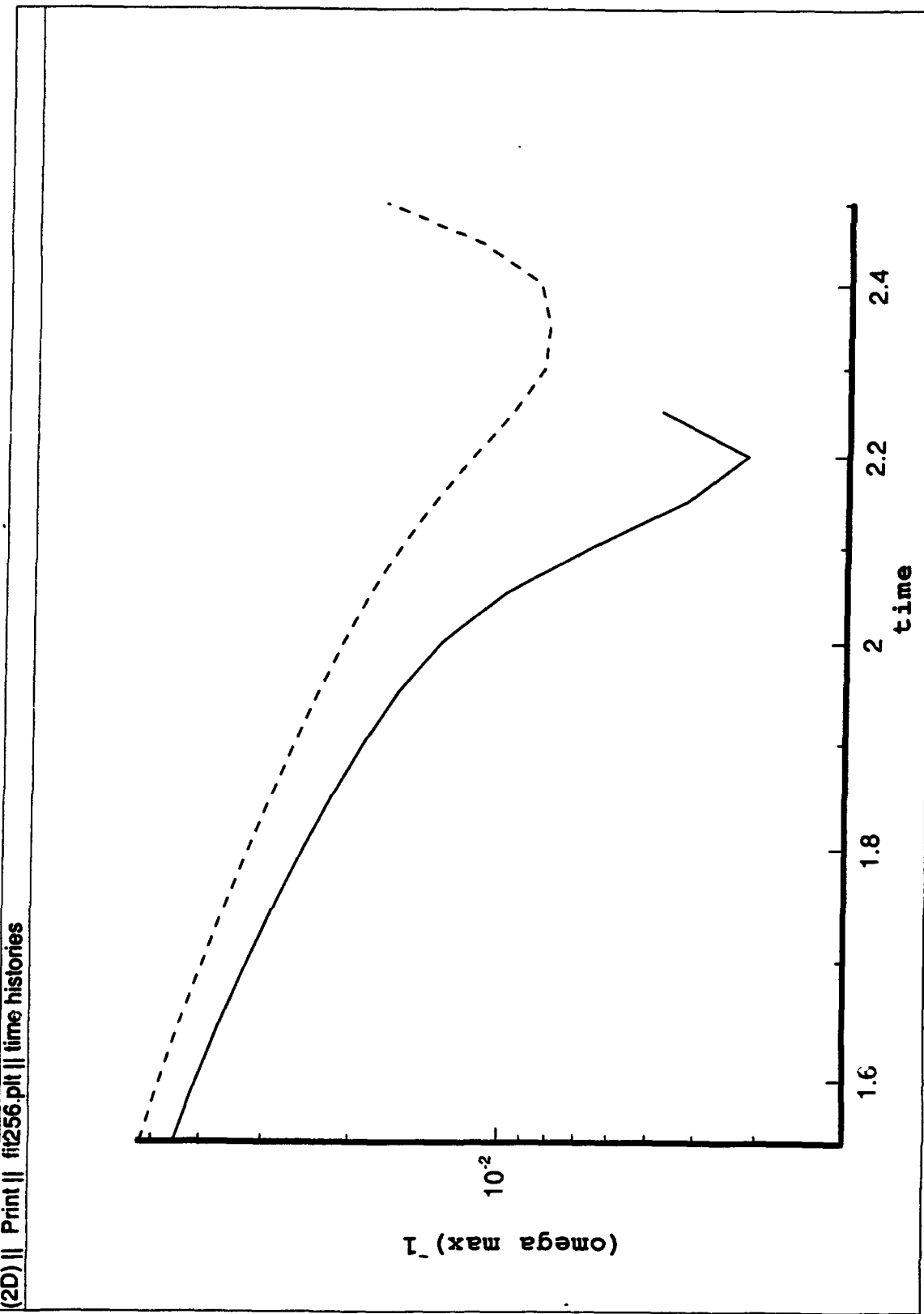


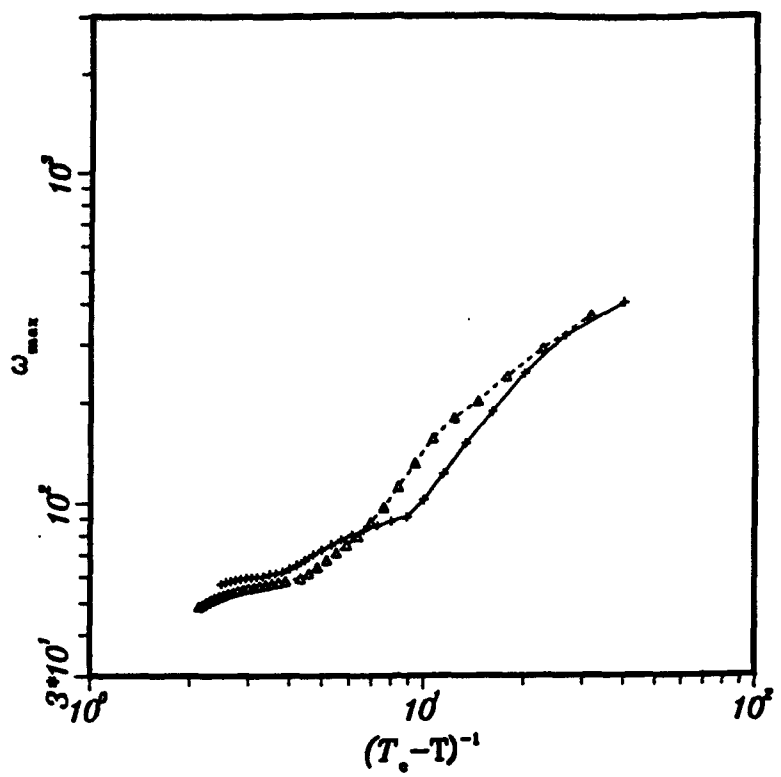




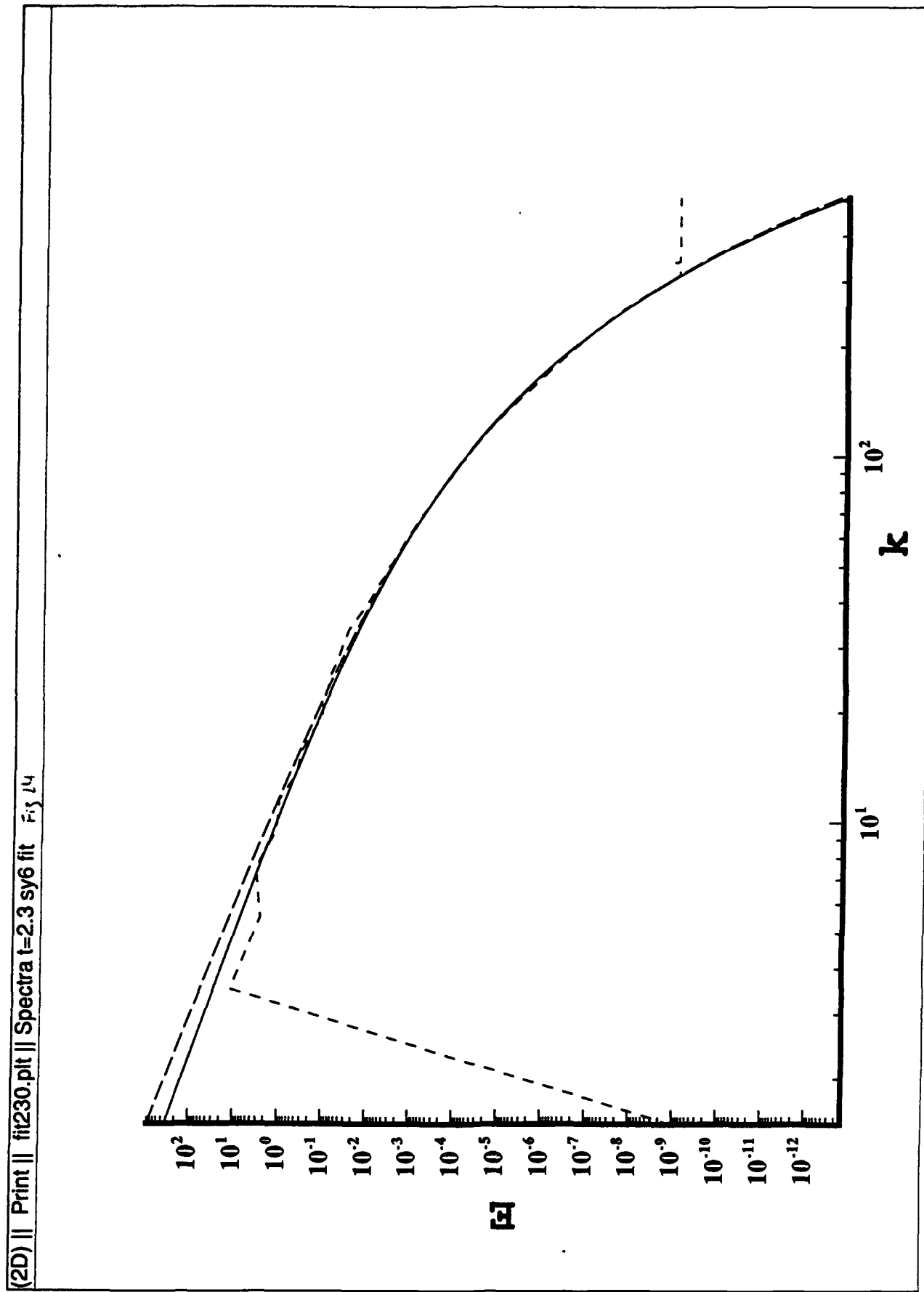


(2D) || Print || fit256.pt || time histories

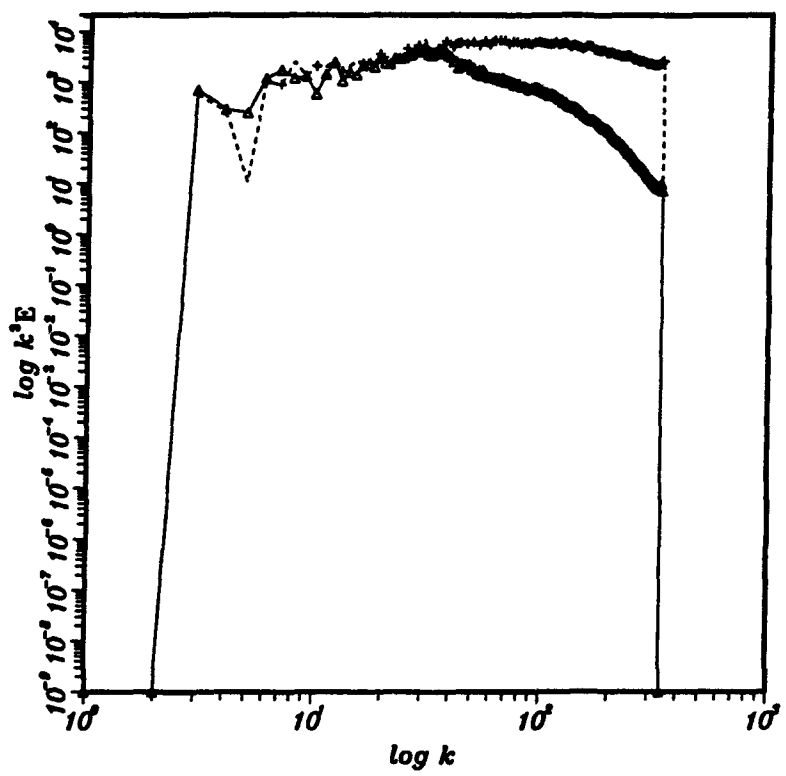
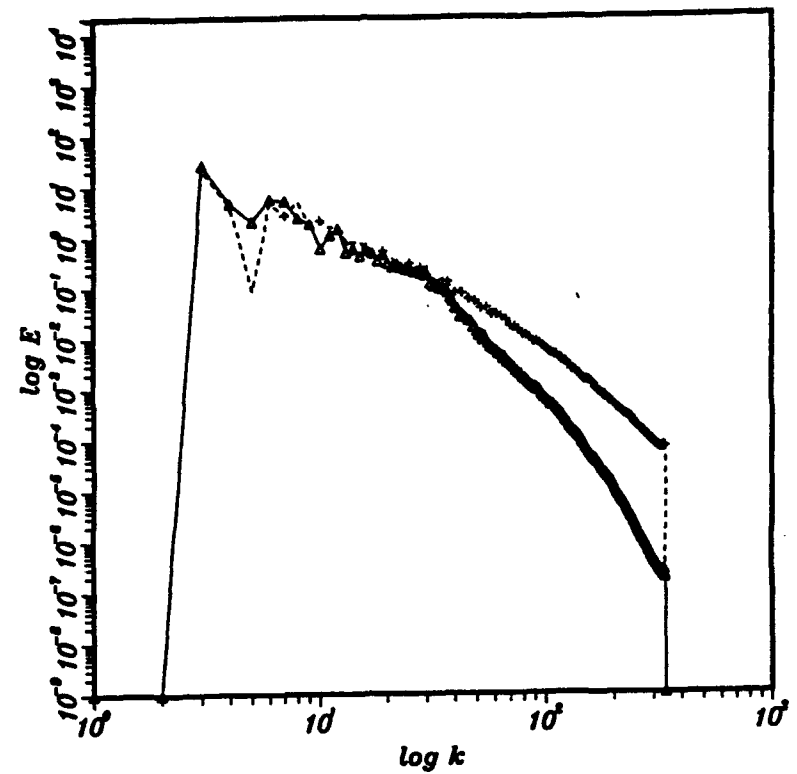


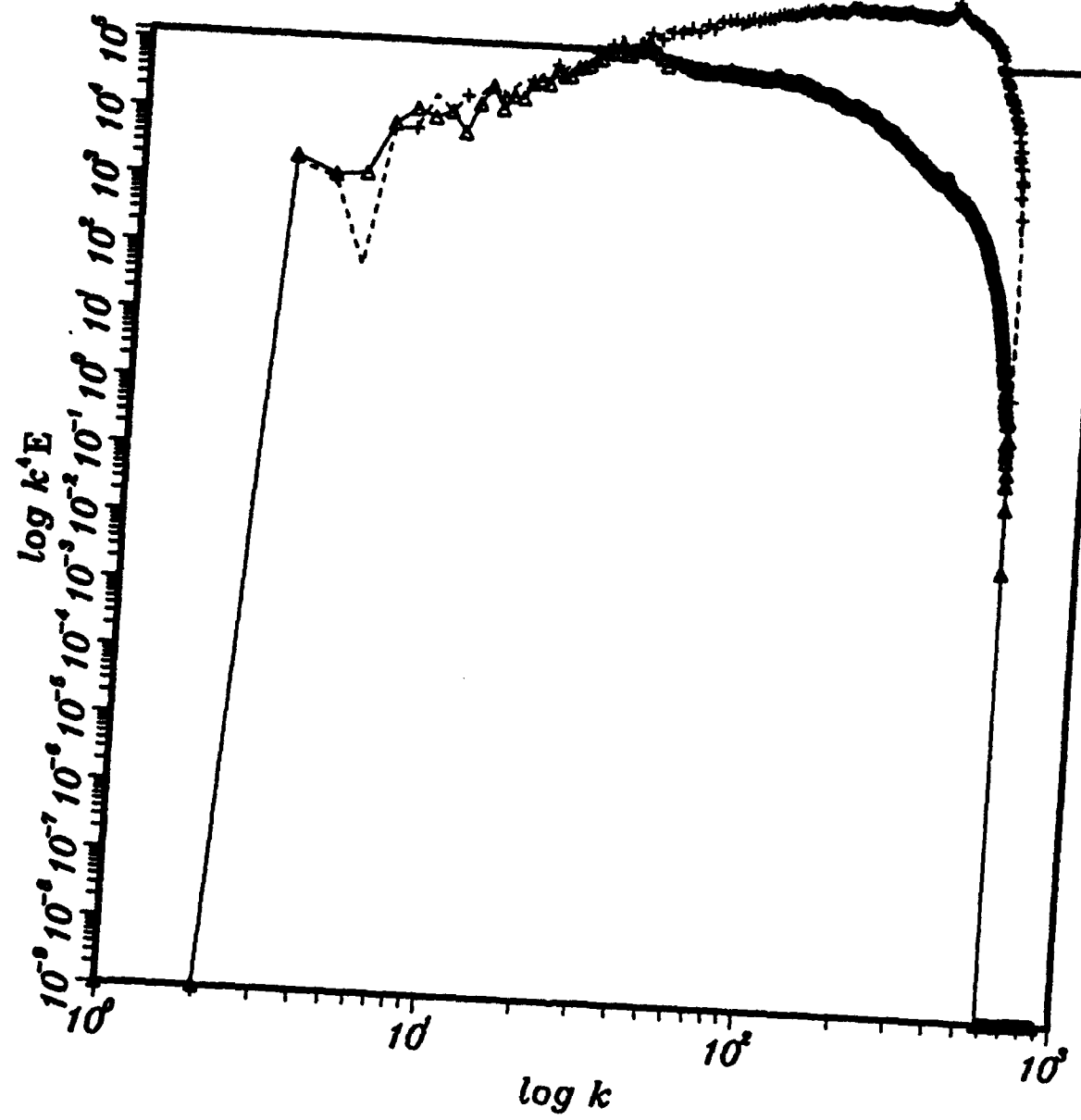


(2D) || Print || fil230.plt || Spectra t=2.3 sy6 fit \tilde{F}_1 l4



23

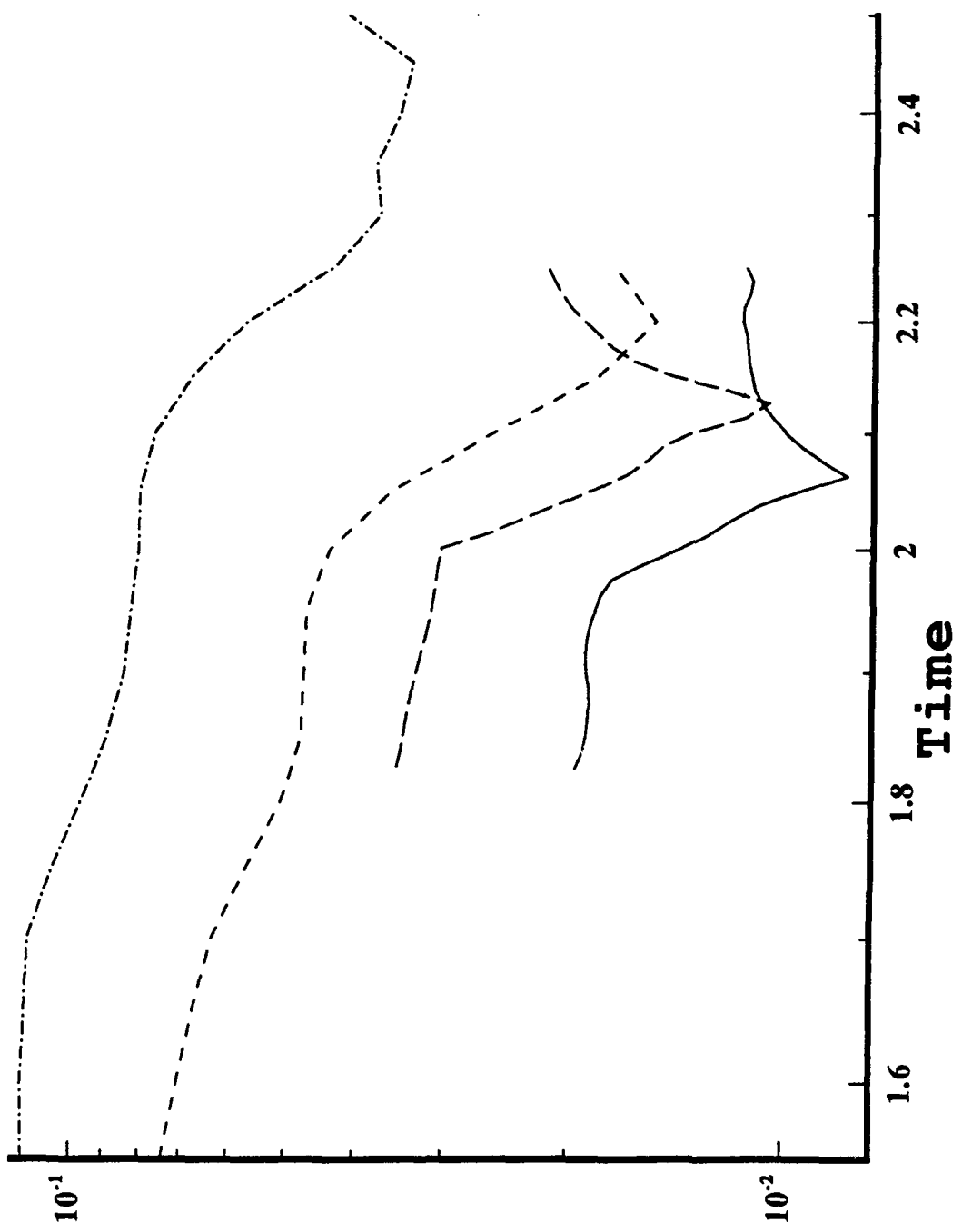


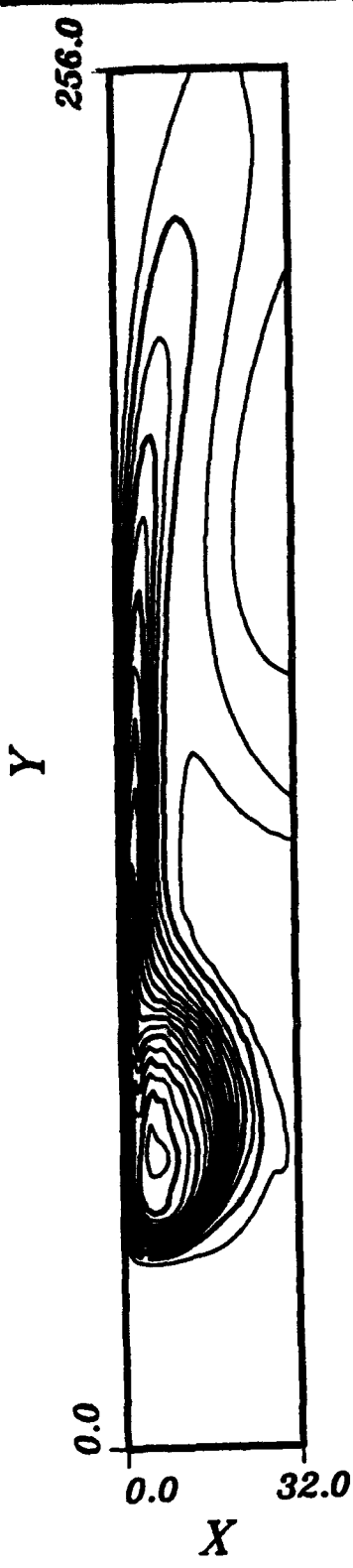


24c

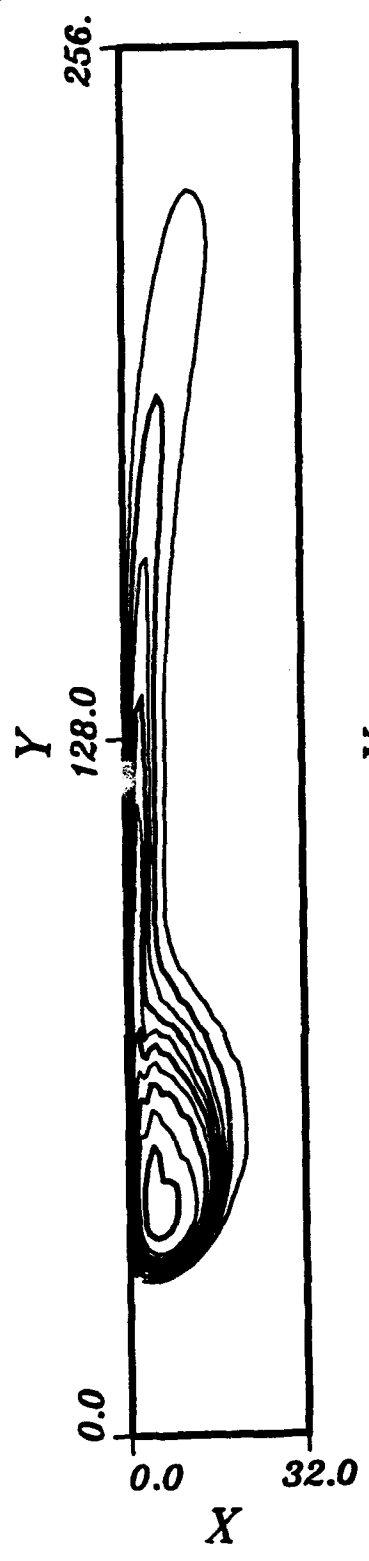
(2D) || Print || sy.print || t and delta

20

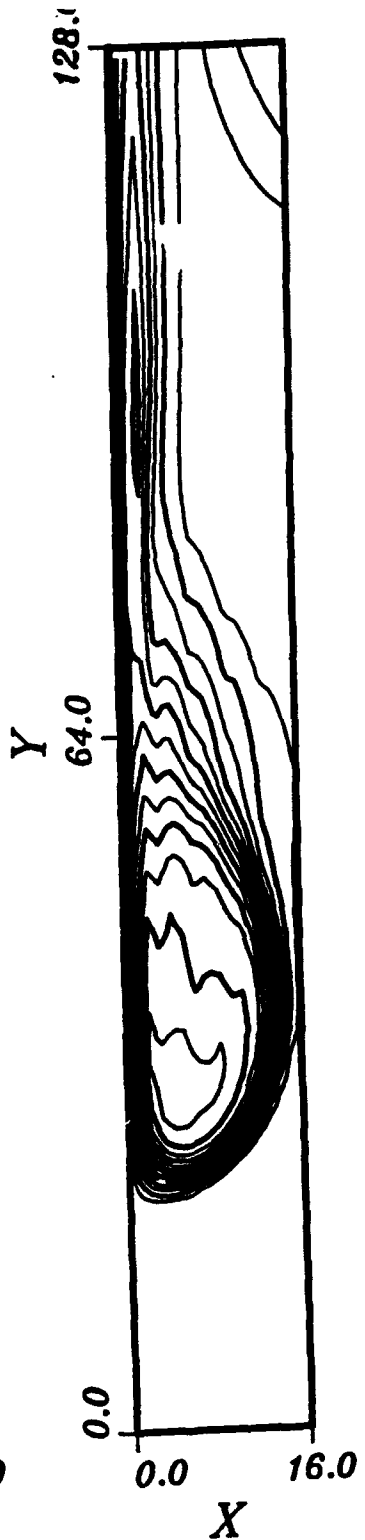




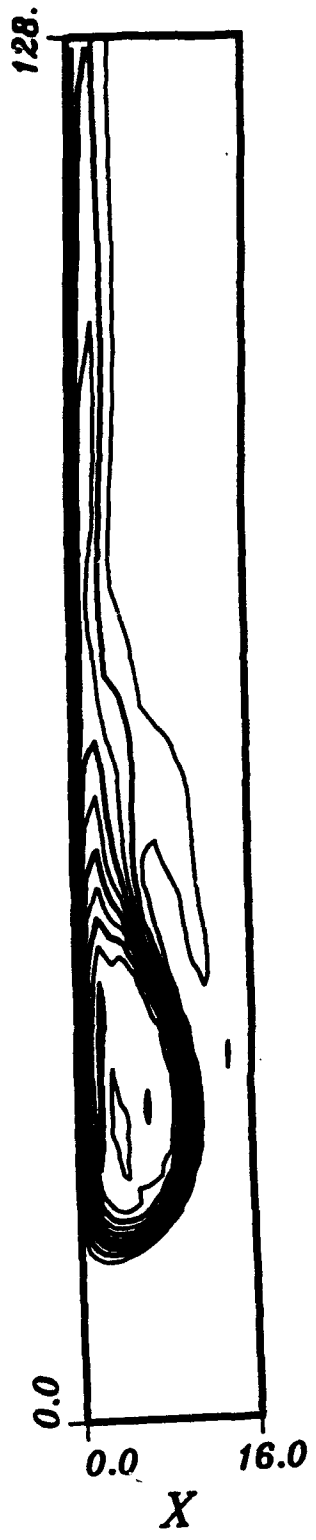
$t=1.75$



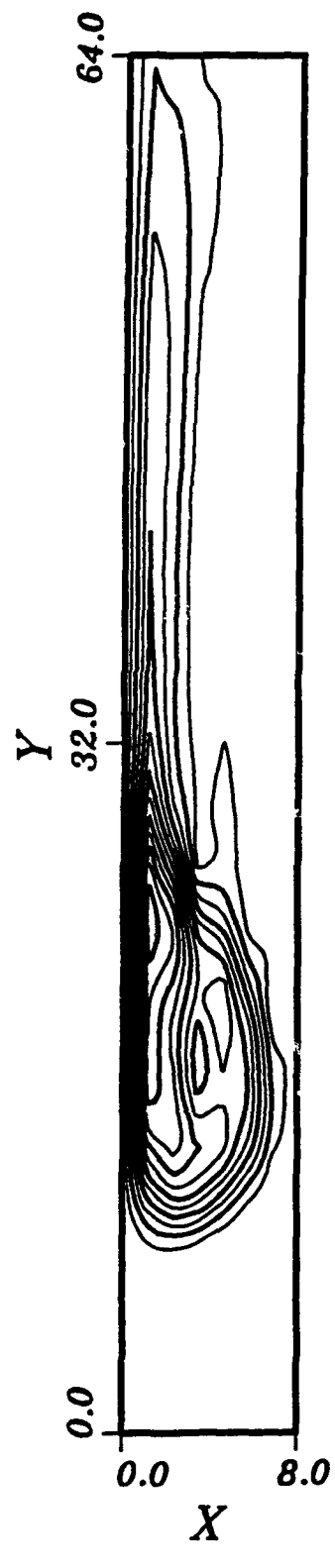
$t=1.8125$



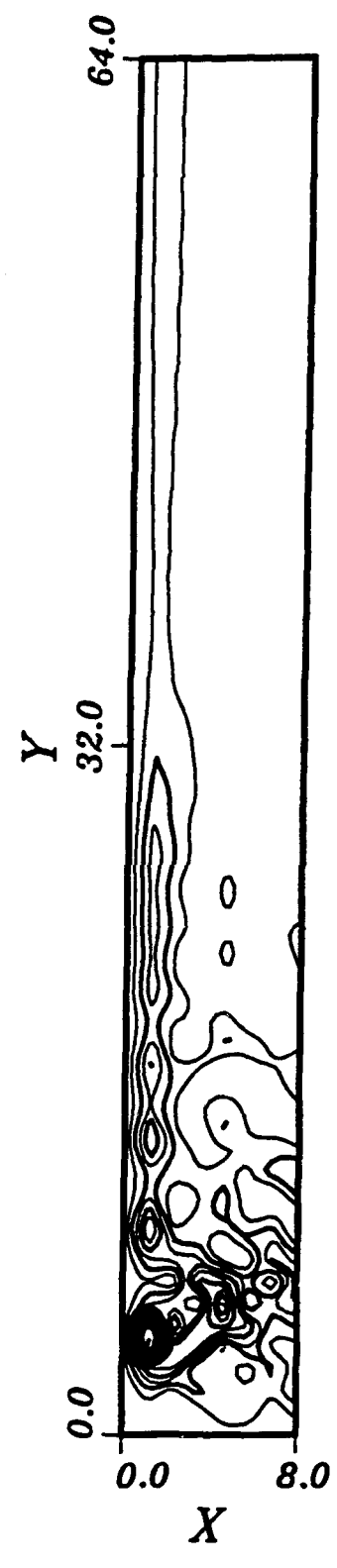
$t=1.875$



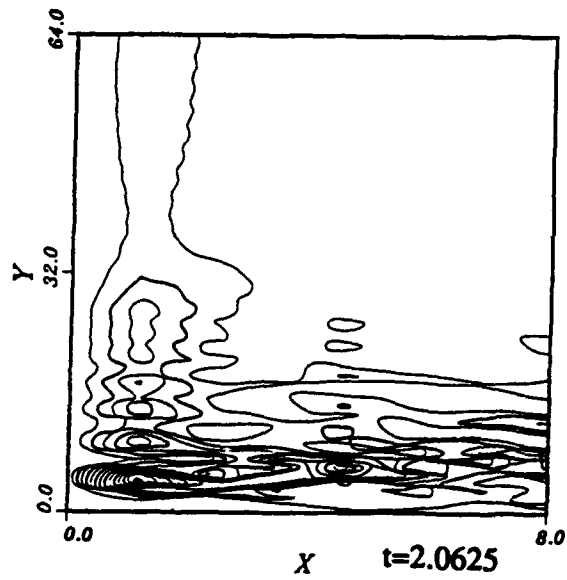
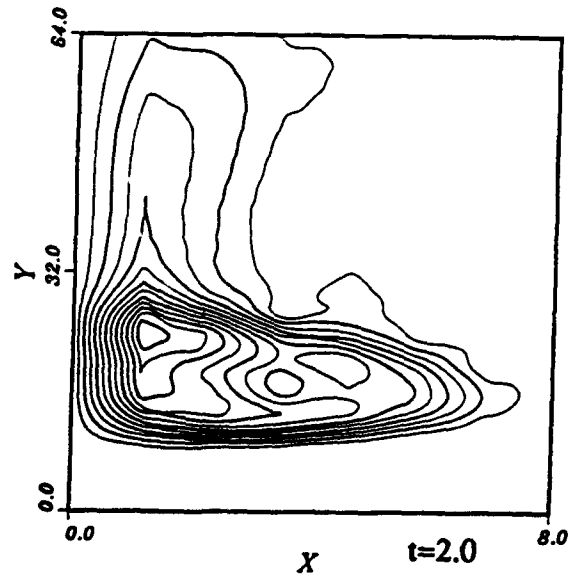
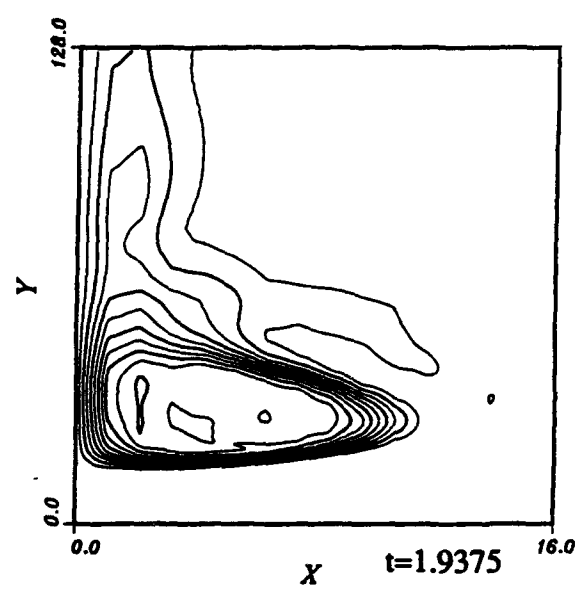
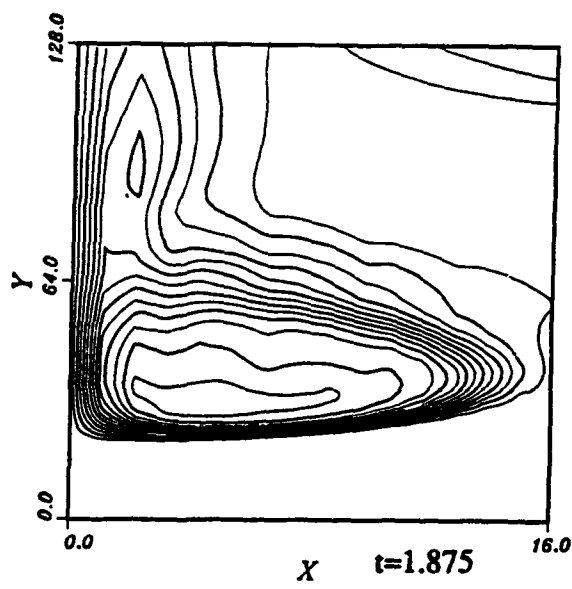
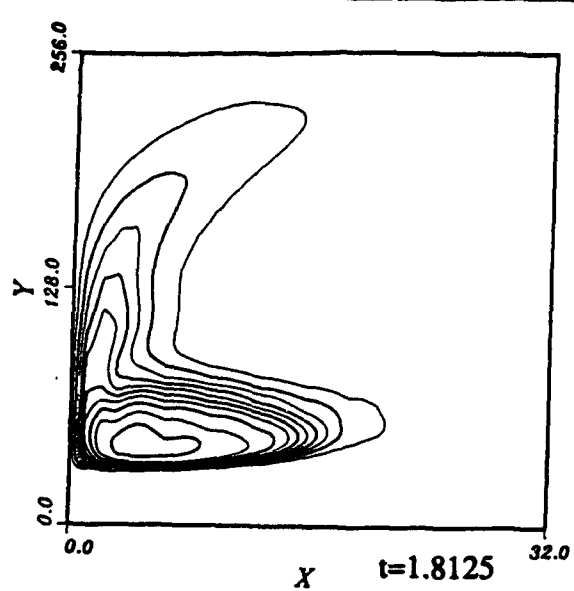
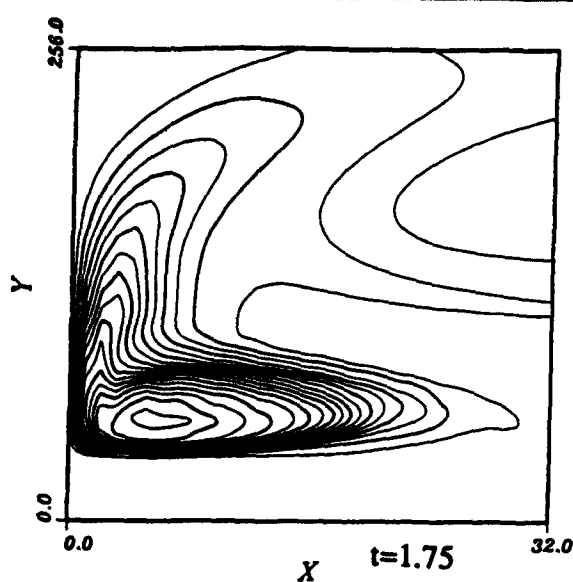
$t=1.9375$

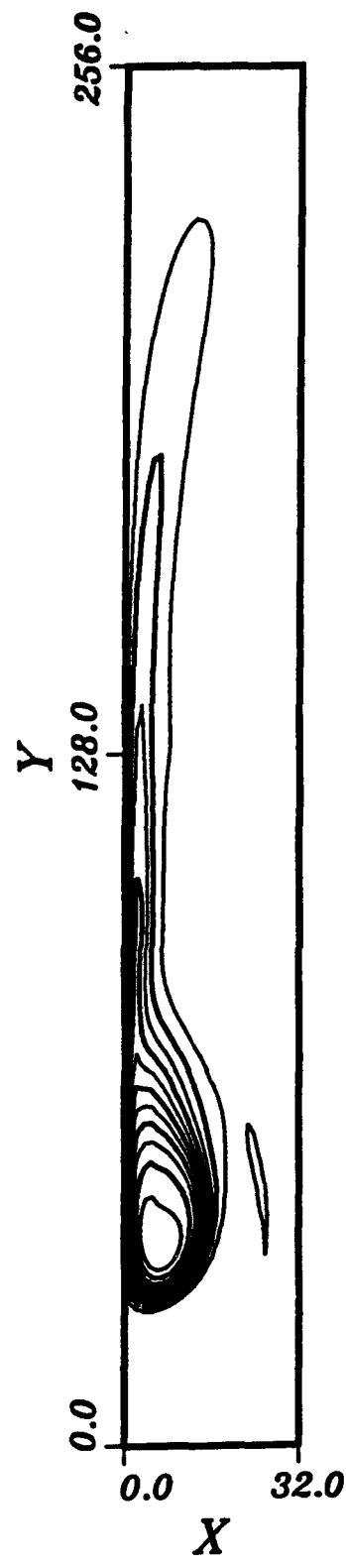


$t=2.0$

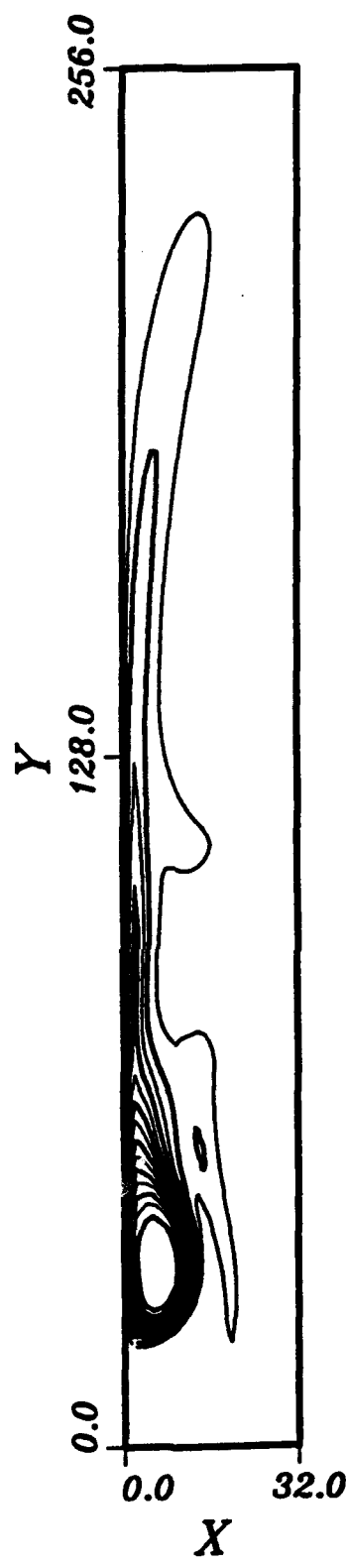


$t=2.0625$

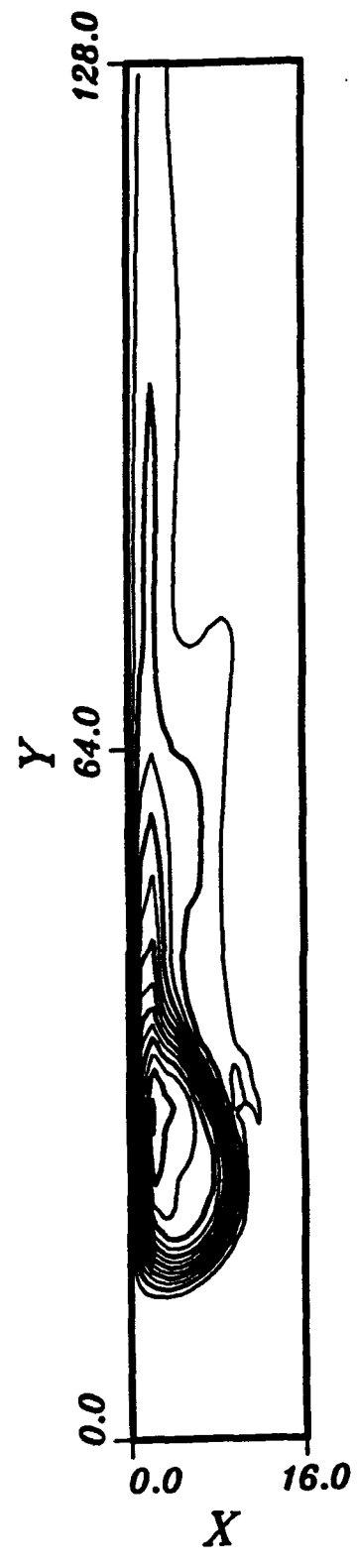




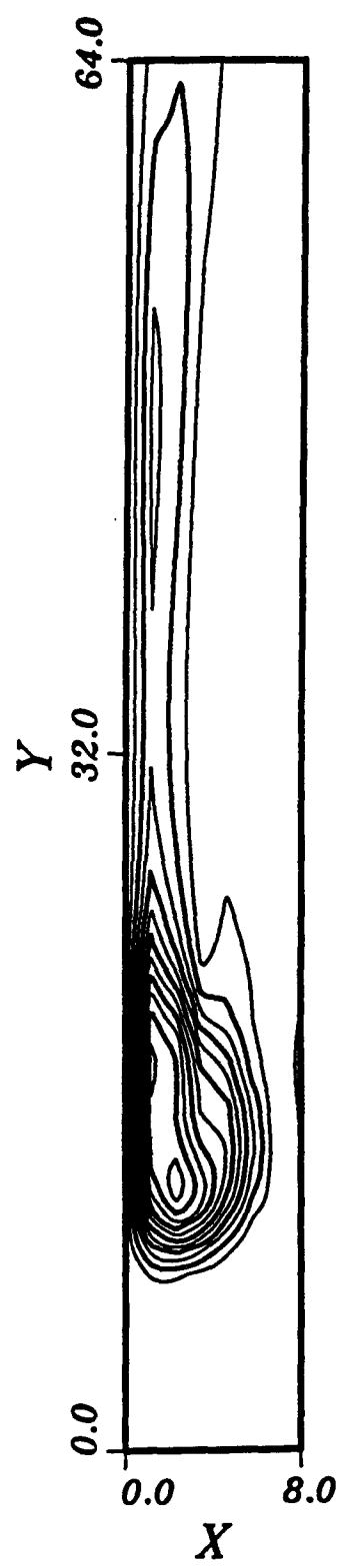
$t=1.875$



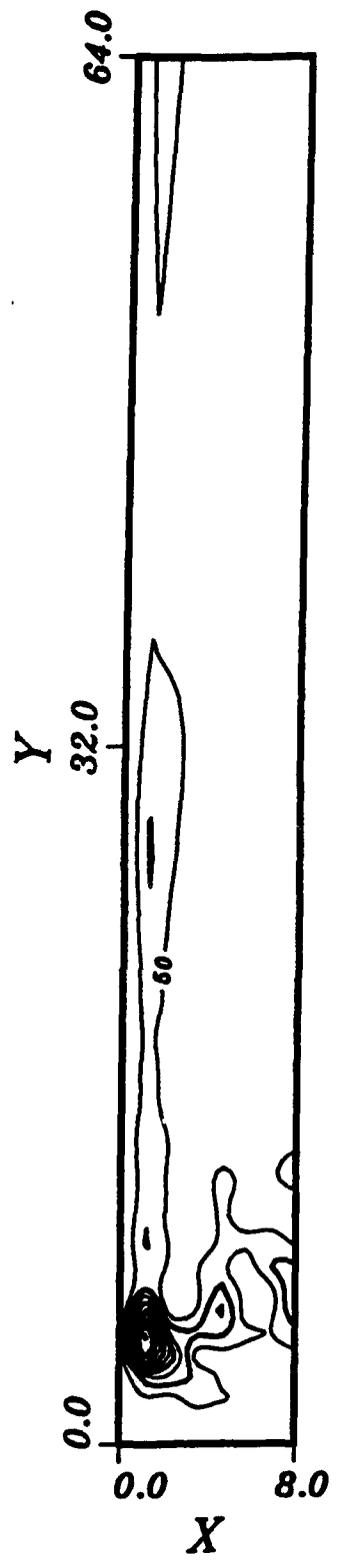
$t=1.9375$



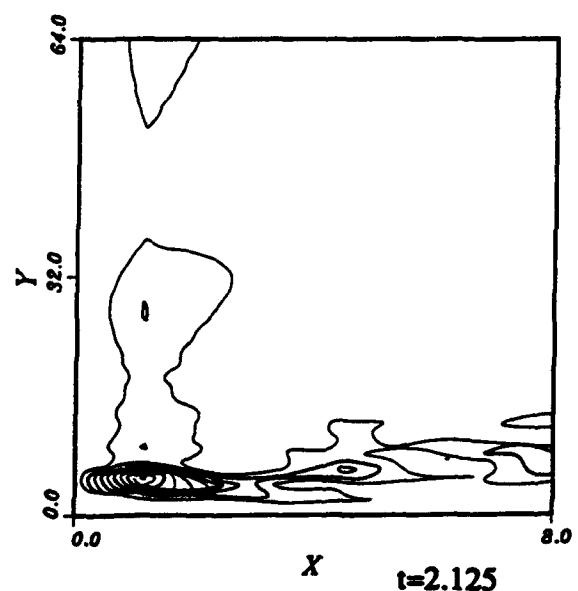
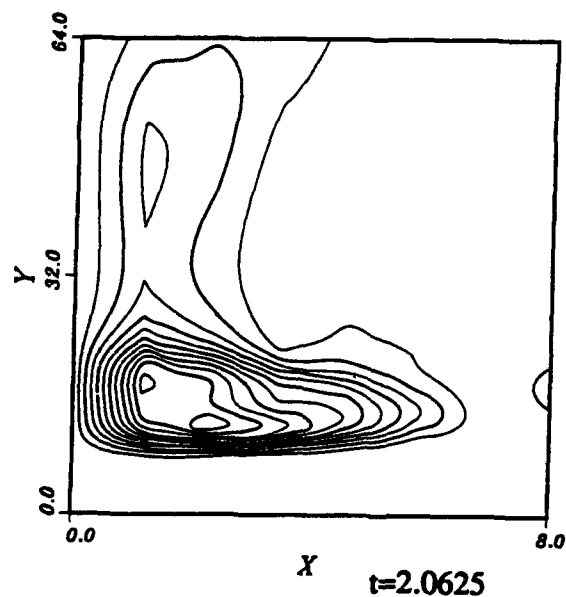
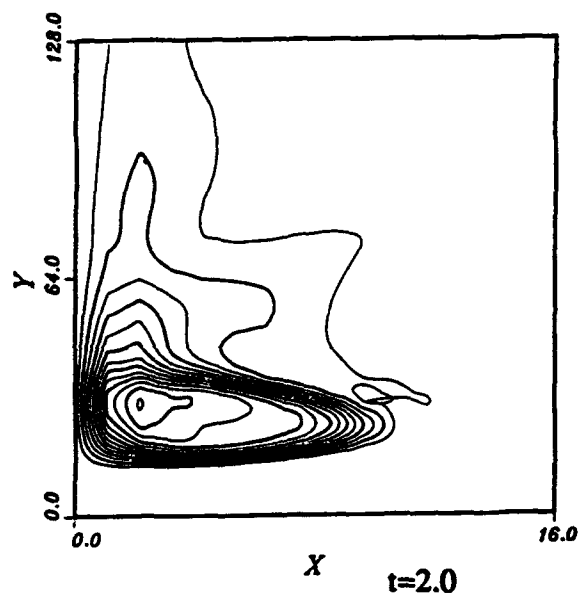
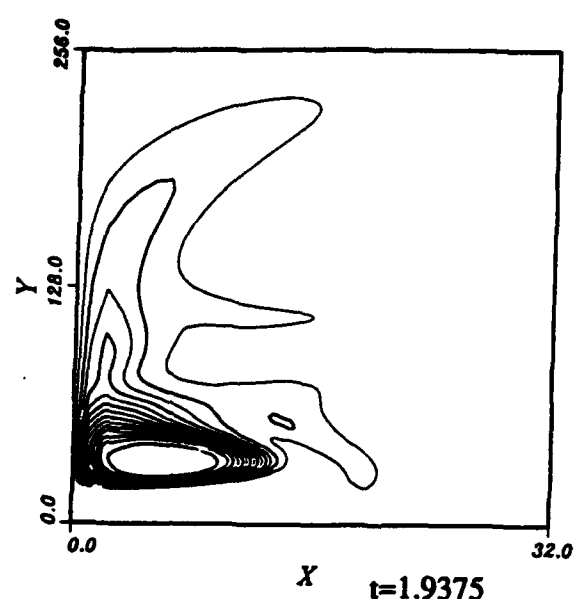
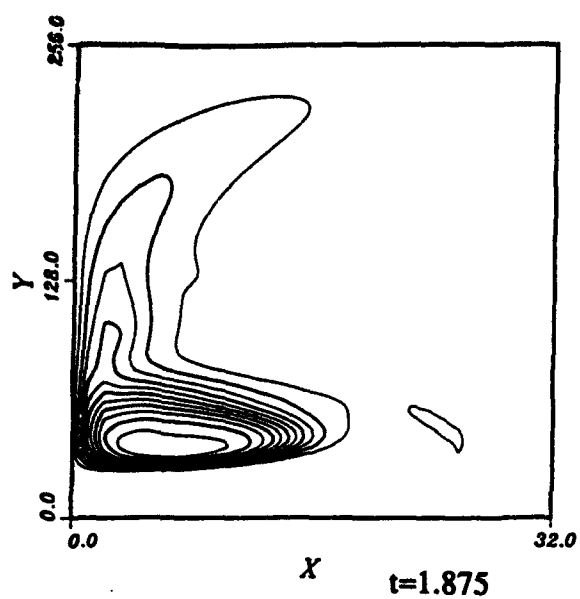
$t=2.0$

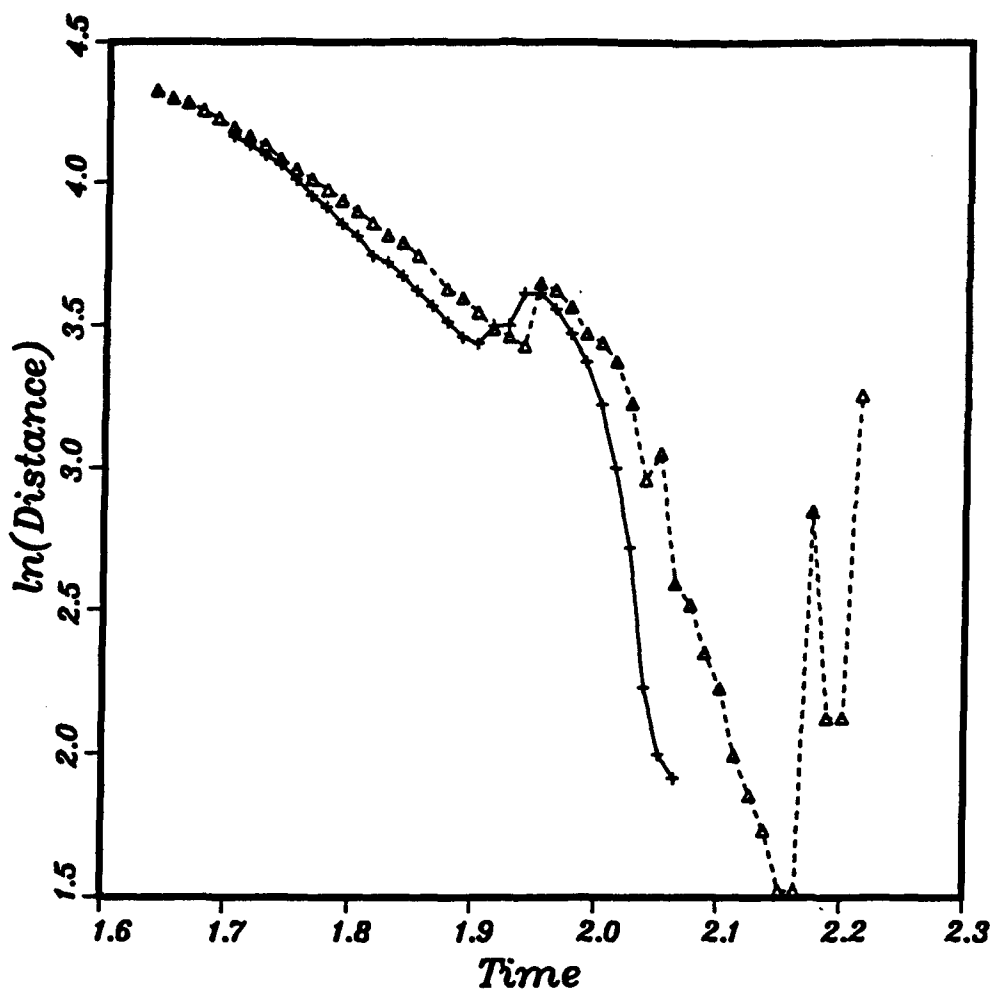


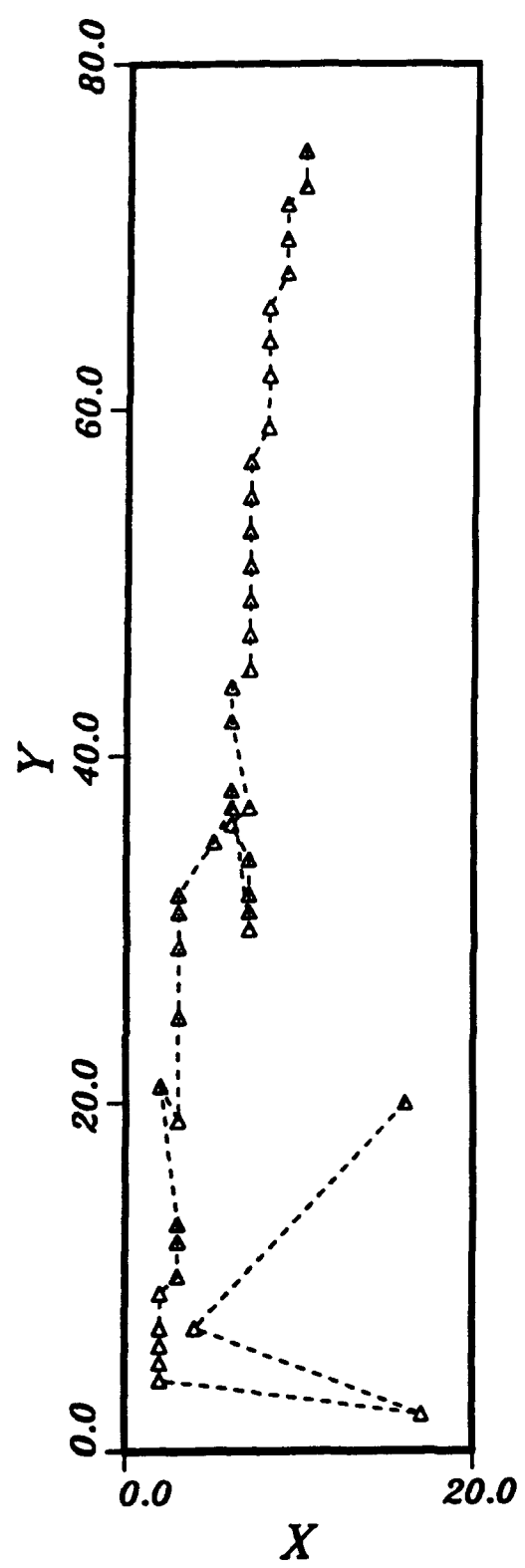
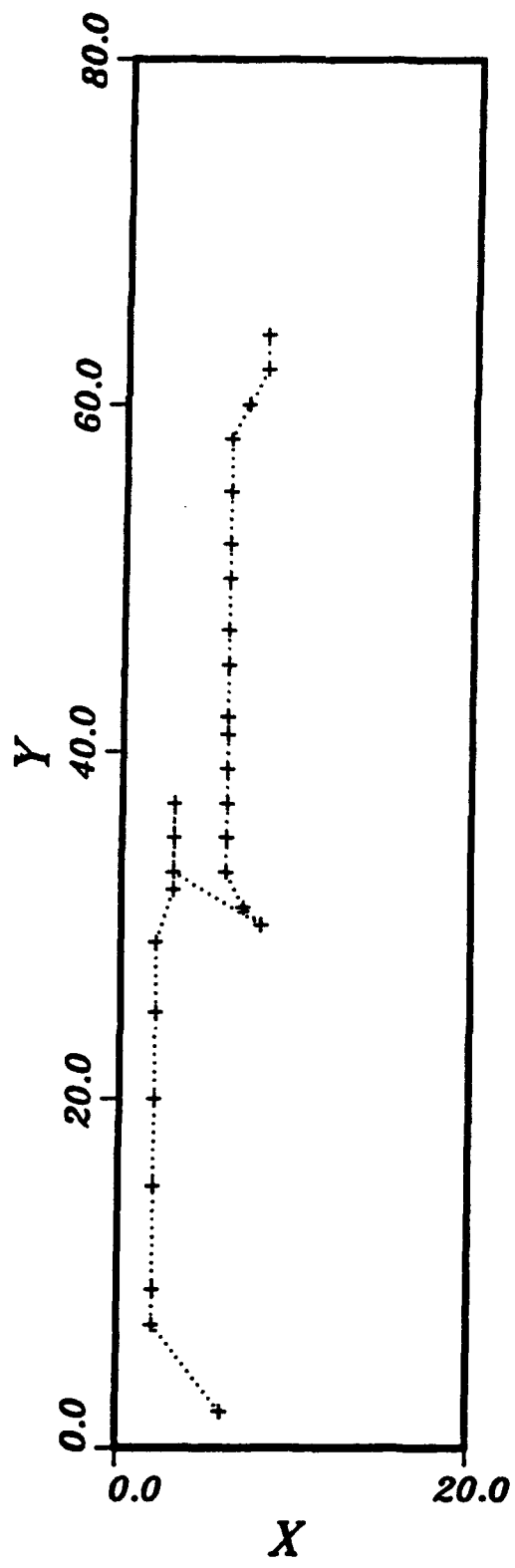
$t=2.0625$



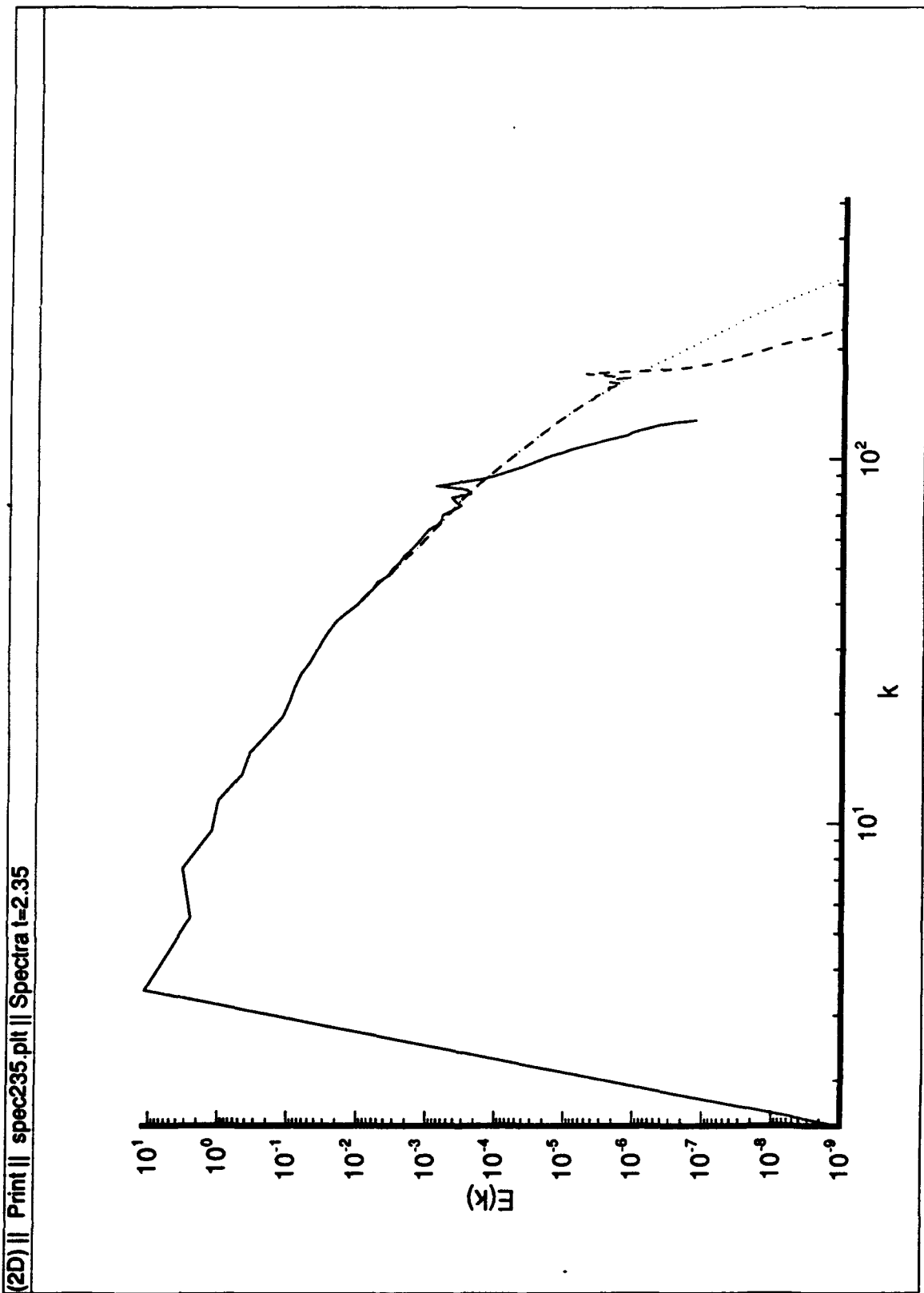
$t=2.125$







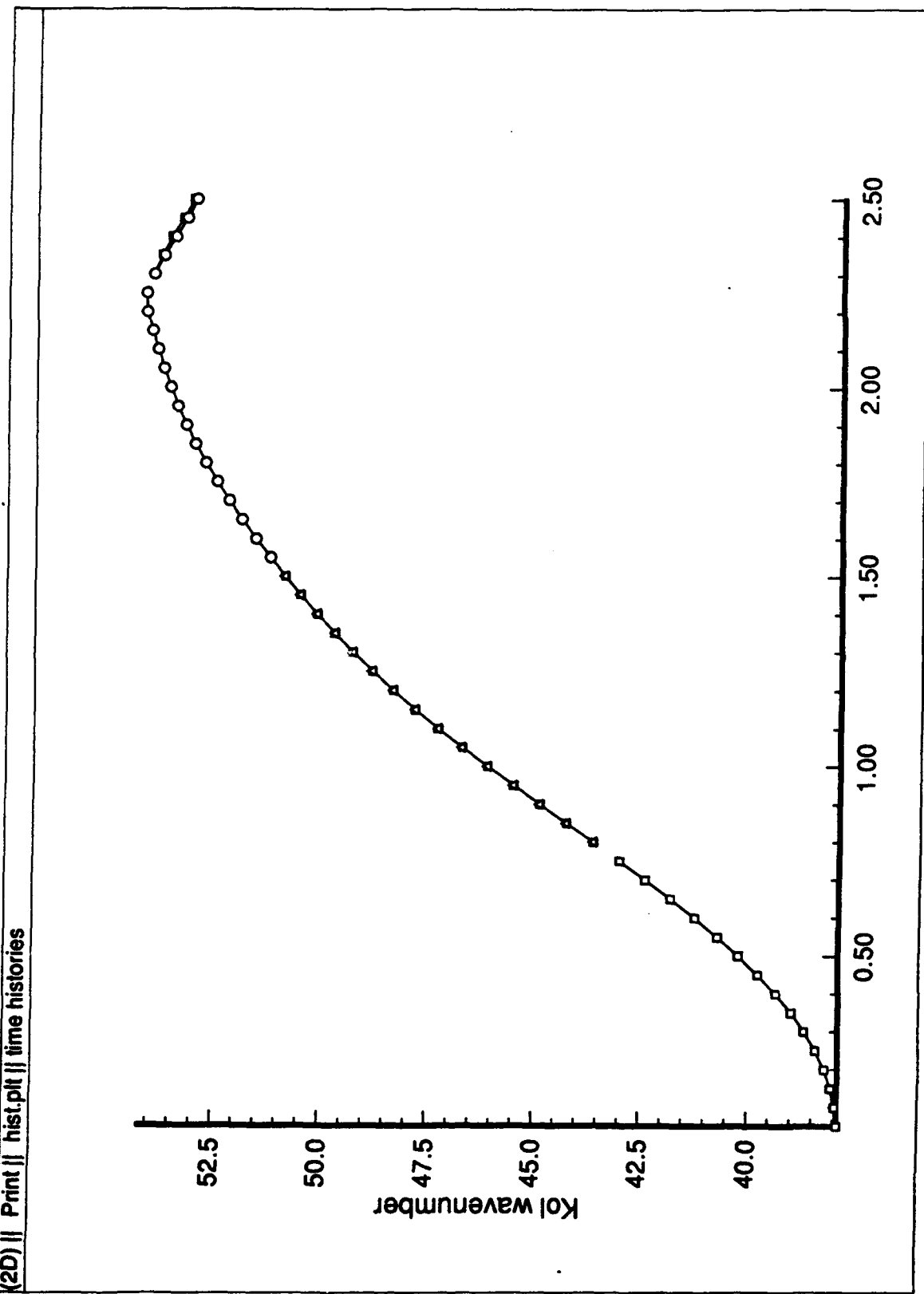
(2D) || Print || spec235.plt || Spectra t=2.35



346

344

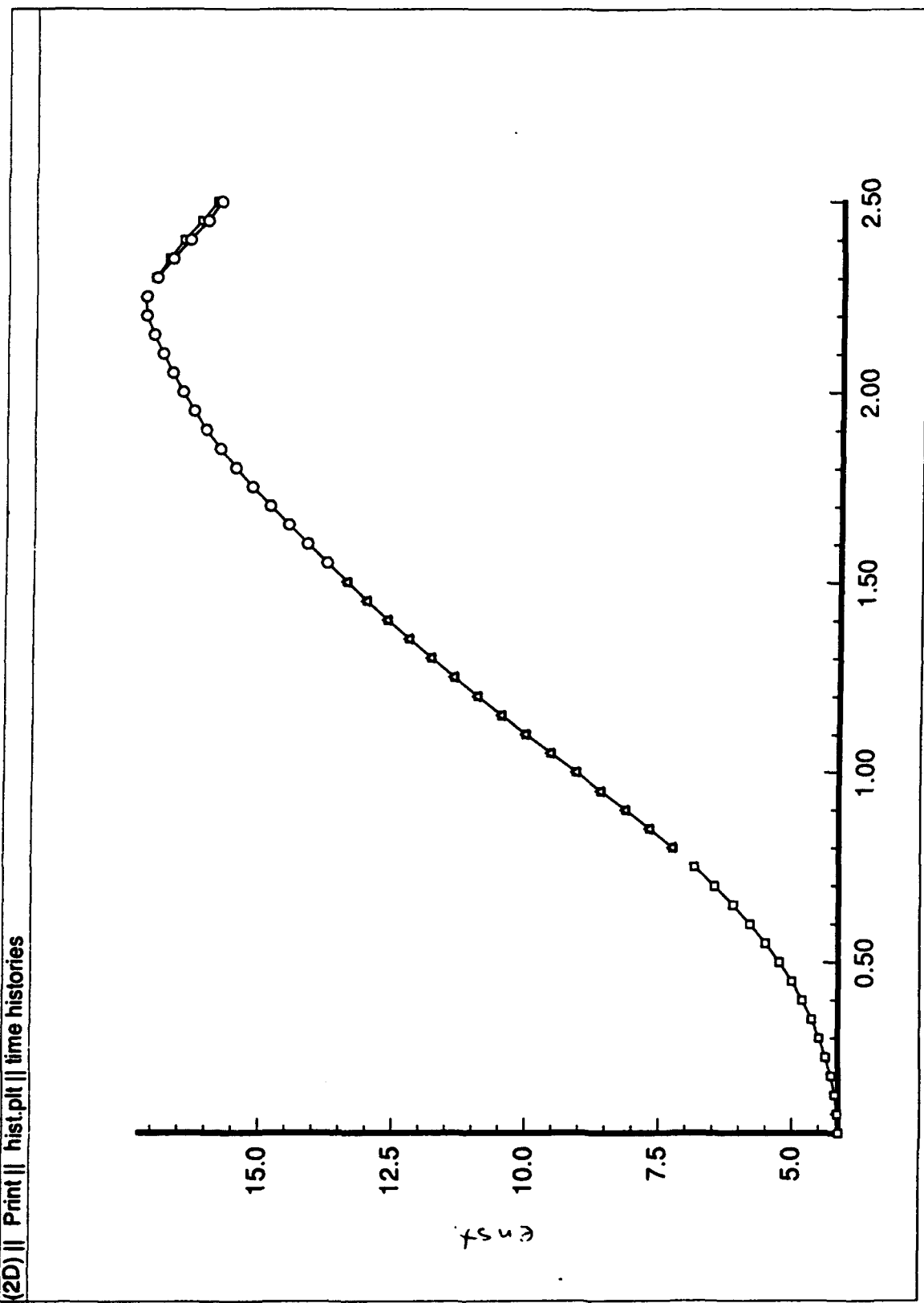
(2D) || Print || hist.pt || time histories



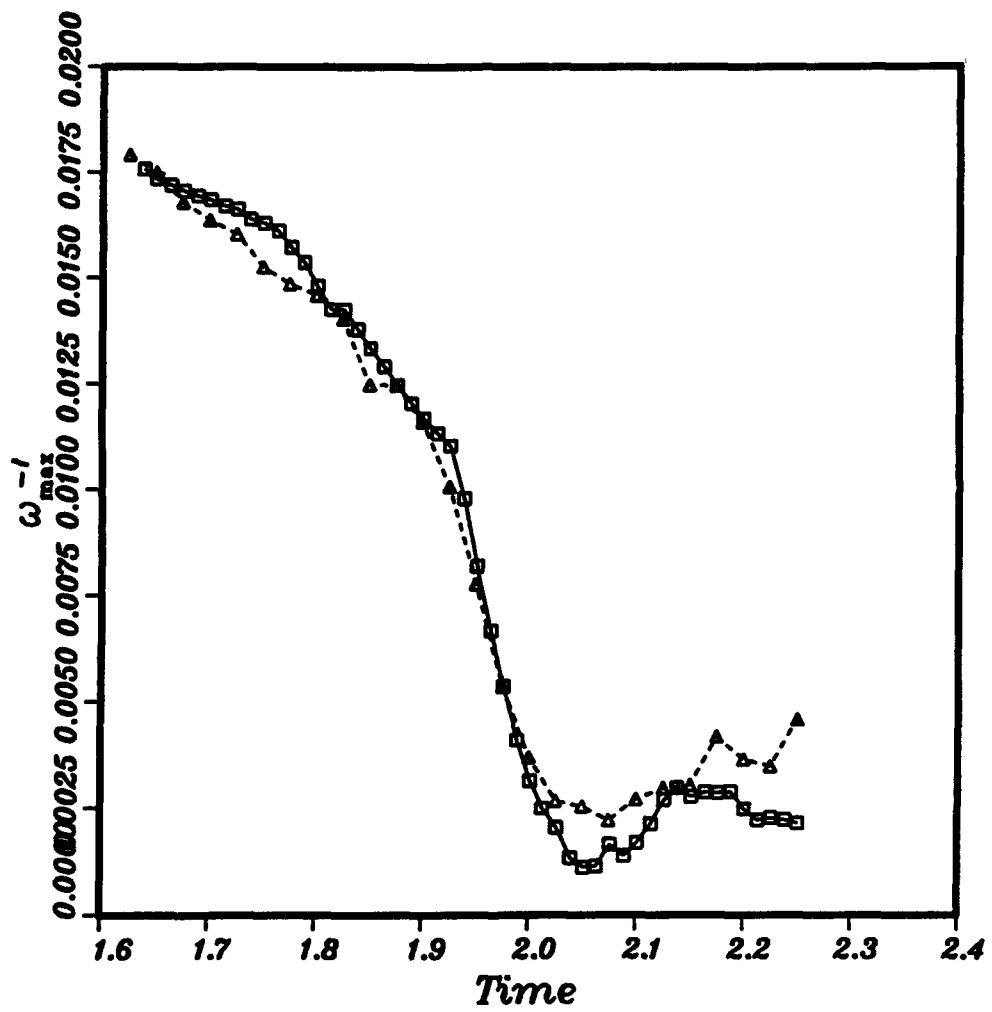
3.5

3.5

(2D) || Print || hist.plt || time histories



36



(2D) || Print || max.pt || time histories

